Alternatives to Pt as the Electrode Catalysts for Polymer Electrolyte Membrane Fuel Cells

A Dissertation

Presented to

the faculty of the School of Engineering and Applied Science

University of Virginia

in partial fulfillment

of the requirements for the degree

Doctor of Philosophy

Chemical Engineering

by

Li, Fei

August

2014

APPROVAL SHEET

The dissertation

is submitted in partial fulfillment of the requirements

for the degree of

Doctor of Philosophy

Li, Fei

AUTHOR

The dissertation has been read and approved by the examining committee:

Matthew Neurock

Advisor

Roseanne Ford

John T. Yates

Robert Davis

David Green

Accepted for the School of Engineering and Applied Science:

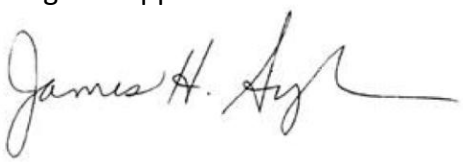

Dean, School of Engineering and Applied Science

August

2014

Abstract

Various non-precious metal materials are examined in this study for their possible use in polymer electrolyte membrane fuel cells (PEMFC) to promote both fuel oxidation at the anode and oxygen reduction reaction (ORR) at the cathode. A Pt-Mo alloy is studied in detail and compared to pure Pt as the anode catalyst for its catalytic activity in activating the C-C bond of ethanol and tolerance to C1 species poisoning. It is found that the introduction of surface Mo atoms to Pt enhances upon pure Pt in both of these two aspects. On the reduction electrode side, a class of organometallic complexes known as transition metal nitrogen-doped carbon (TM-N-C) materials was studied as possible substitutes for Pt. It is found that similar to the natural cytochrome c enzyme that inspires their discovery, the TM-N-C materials can achieve ORR activities rather close to that of Pt. Moreover, the $2e^-$ incomplete reduction and $4e^-$ complete reduction of oxygen can be selectively promoted by employing different metal centers due to different electron backdonating capabilities of transition metals. A further study of TM-N-C structures residing between various graphene edge structures showed even higher activities towards O-O bond activation. However, such enhanced O-O cleavage also results in severe O* poisoning. Three N-doped carbon systems without the presence of metal elements were further examined in this study to account for ORR activities recently observed in experiments on these materials. It is found that the catalytic activity of the active carbon site is closely related to the N-doping configurations, with the graphitic-N doping configurations generally leading to better ORR performances.

Table of contents

List of Figures

List of Tables

Chapter 1. Introduction

Before the era of the polymer electrolyte membrane fuel cells (PEMFC), alkaline fuel cells (AFC) were the most maturely developed and widely used. Although AFCs provide several advantages such as that the alkaline environment is less corrosive thus ensures a longer cell longevity when compared to PEMFCs, the issues regarding alkaline electrolyte carbonation due to CO_2 from the air or the oxidation products form at the anode are hard to eliminate and thus limit the prospect of their application [1]. The use of highly proton-conductive and electron-insulative perfluorosulfonic acid (PFSA) polymer membranes, also known as Nafion developed by Dupont Chemical in late 1960s [2, 3], as the electrolyte in fuel cells has promoted the prosperity of the applications of PEMFCs [4]. From that moment on PEMFCs have quickly become popular substitutes for AFCs due to the advantages from the flexibility of using the polymer electrolyte membrane as a solid electrolyte and thus the avoidance of electrolyte leakage, low operating temperatures and zero emissions [1]. The PEMFCs were first utilized as an auxiliary power source in NASA's Gemini spacecrafts [4] and since then were extensively utilized in the manufacture of space shuttles, automobiles, electronic portable devices and military weapons due to advances in their fundamental designs and emergence of new fabrication methods of the fuel cell components [5-10].

The essential part of the PEMFC is the membrane electrode assembly (MEA), which includes the polymer electrolyte membrane that provides the proton shuttling channels within the fuel cell, sandwiched by two catalyst layers and two gas diffusion layers (GDL) that provide the space for gas fuel (H_2, e.g.) and oxidant (O_2, e.g.) to diffuse to the catalyst-electrolyte interface [9, 11, 12]. The catalyst layer (also called the active layer) and the GDL are both porous structures with the latter typically composed of cloth or carbon paper that is 0.2 to 0.5mm thick [12]. The three components are typically fabricated separately and compressed together between two bipolar plate current collectors with built-in gas distribution channels to form a single cell, and experimental results regarding single fuel cell vs. fuel cell stack performances in the last decade indicate that multiple single cells stacked in series can provide greater power capability and fuel conversion efficiency [13-16]. The polymer membrane lies at the heart of PEMFC and directly provides the electrolyte-electrode interface along with the catalyst layer where fuel oxidation and oxygen reduction occur [8, 9]. The particular characteristic of the PFSA membrane of being proton-conductive determines that most of the chemical processes occurring within the PEMFC are carried out under acidic conditions. The electron-insulative characteristic of the membrane ensures that the electrons released together with the protons at the anode as a result of fuel oxidation will take an electrical detour through the outer circuit instead of short-circuiting the fuel cell [9]. Fuels are fed via an inlet to the anode and will later diffuse through the GDL to the anode-electrolyte interface to be oxidized. When liquid fuels such as ethanol are used instead of H_2, additional gas and liquid outlets for complete and incomplete oxidation products such as CO_2, acetaldehyde and acetic acid are required. At the cathode, O_2 is generally fed into the fuel cell to diffuse through the GDL and subsequently combine with electron and proton to be

reduced at the cathode-electrolyte interface. Additional gas outlet for excess unreacted O_2 and liquid outlets for oxygen reduction products such as water and hydrogen peroxide are installed at the cathode [12]. An illustration of the general fuel cell structure is shown in Fig. 1.1.

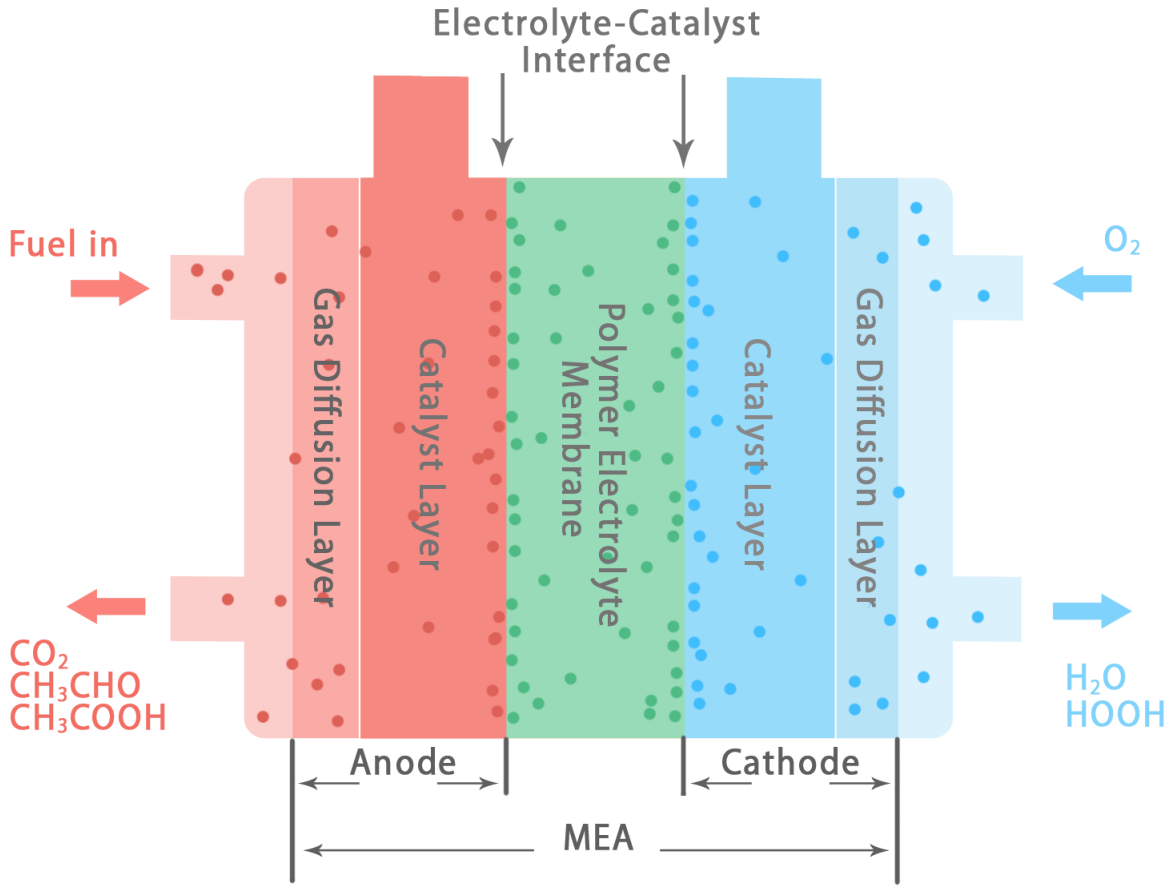

Figure 1.1. The Membrane Electrode Assembly (MEA) comprising the polymer electrolyte membrane, the catalyst layer and the Gas Diffusion Layer (GDL) within a PEMFC.

Certain level of humidity must be maintained for the polymer electrolyte membrane to work optimally. The proton conductivity of Nafion and related PFSA polymer membranes are found

to reach an optimal level when the membrane is fully hydrated, since the proton conduction process across the membrane is actually carried out by water molecules carrying proton in the H_3O^+ form that subsequently permeates through pores of the membrane [11, 17]. There are two main causes that might lead to possible dehydration of the membrane and therefore decrease in the proton conductivity of the membrane: one is the polarity of water molecules that leaves them under the influence from the so-called "electro-osmotic drag" transport phenomena [17-20] within the fuel cell that constantly pulls water away from anode towards cathode, which dries up the anode; the other is the loss of water due to under-saturated gas streams in and out of the PEMFC [17, 21]. On the other hand, the generation of additional water at the cathode due to oxygen reduction reaction, combined with water that migrates from the anode to the cathode due to electro-osmotic drag transport, might instead cause flooding beyond the membrane into the pores of the cathode catalyst layer and the GDL, leading to high mass transport resistance [21]. Therefore proper water management has become an important issue in the study of PEMFCs and numerous studies have been carried out to optimize the circulation of water in PEMFCs in recent years [3, 17, 21-23]. A popular direction is to reduce the thickness of the membrane to magnify the water back-diffusion process from the cathode to anode [24]. However, thinner membranes suffer from the so-called gas crossover [25, 26] which leads to insufficient fuel utilization and accelerated membrane degradation [27]. The coordination of water management and gas crossover prevention has been a long-lasting topic in the field [25, 26]. Besides all these extremely complicated water transport phenomena occurring in PEMFCs, we take a simplified approach to model a catalyst-aqueous interface that mirrors this hydrated membrane electrolyte-electrode

interface with proton conducted via chains of water molecules in the form of H_3O^+. More specifically, we focus on an extremely thin water layer up to several nanometers thick adjacent to the catalyst surface that represents the electrical double layer within which the electric potential gradient is the steepest and therefore the electric field strength is much higher than in the bulk solution [28, 29]. Multiple theoretical models are developed in history to understand the electrical double layer [30-32]. These models generally assume the formation of a capacitor between surface charges and a loosely attached layer of solution counter ions. The layer of counter ions screens out the electric field thereby confines the electric potential drop within the electrical double layer. As can be seen from Fig. 1.2, the potential increases dramatically from the anode to the bulk solution within the anode electrical double layer and increases dramatically again from the bulk solution to the cathode within the cathode electrical double layer. The electrical double layer is hence fundamentally important due to the profound impact of its strong electric field on most electrochemical processes that predominantly occur at the electrolyte-catalyst interface [33]. The simulation of electrical double layers using the double reference method [34] developed previously in our group will be discussed later in the chapter of method.

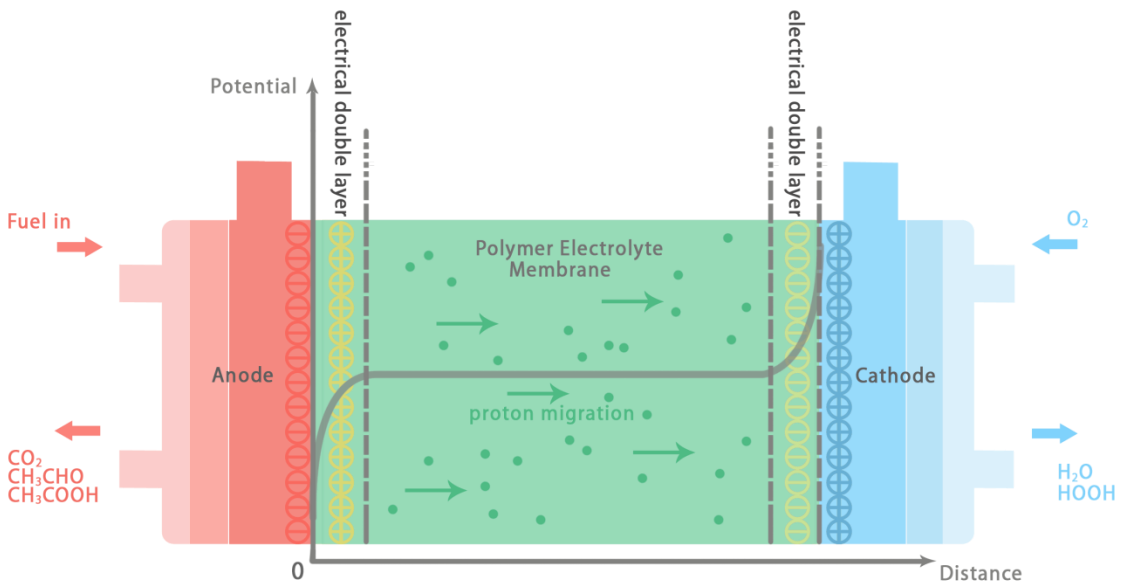

Figure 1. 2. A simplified illustration of the electrical double layer. The green arrow shows the migration of protons in the form of H_3O^+ through the pores of polymer electrolyte membrane. The electric potential changes dramatically only within the thin electrical double layers which are usually several nanometers thick.

Besides the appropriate study of the water environment in PEMFCs, the examinations of catalytic activities of anode and cathode catalysts are probably of even greater importance when it comes to the conversion of chemical energies to electric energies within the PEMFCs. Under working conditions, the potential established at the cathode is always higher than that at the anode due to the fact that the anode is always more electron rich than the cathode, which results in an electric field that always points from the cathode to the anode. This electric field drives the external flow of electrons from the anode to the cathode. Within the fuel cell, the formation of the electrical double layer confines the electric field, and an opposite chemical

force resulting from thermodynamic chemical potential equilibrium (or simply the gradient of the chemical potential within the fuel cell) overcomes the electric force and drives the flow of proton also from anode (high chemical potential but low electric potential) to cathode (low chemical potential but high electric potential) [12, 35]. It is just these two accompanying but separate electric and chemical forces that render the typical “electrochemical” environment within which most of the catalysis phenomena we are interested in are carried out. Under equilibrium or the so-called reversible/open-circuit conditions, the chemical force and the electric force will eventually become balanced, and the difference between the cathode potential and the anode potential is termed the reversible electromotive force or the open circuit voltage [12, 36]. The anode is maintained at an electron-rich state while the cathode is maintained at an electron-deficient state, and two stable electrical double layers are established as a result at both the anode and cathode under open-circuit conditions. Under working conditions, however, the electron accumulated at the anode will begin to flow out to the electron-deficient cathode through the connected external circuit, and overpotentials will be created at both the anode and cathode due to the sluggish kinetics of electrode reactions, which causes deviations of the actual electrode potentials from the equilibrium open-circuit electrode potentials. Such overpotentials are reflected as an increase in the operating potential at the anode and a decrease in the operating potential at the cathode [36, 37]. The overpotentials are essentially consequences of the destruction of the equilibrium electrical double layer structures due to delays in the replenishment of additional electrons that flows out of anode and consumption of additional electrons that flows into cathode under working conditions, which alters the original reversible electron-rich and electron-deficient states of the

anode and cathode. The generations of overpotentials at both the anode and cathode of PEMFCs under working conditions are illustrated in Fig. 1.3.

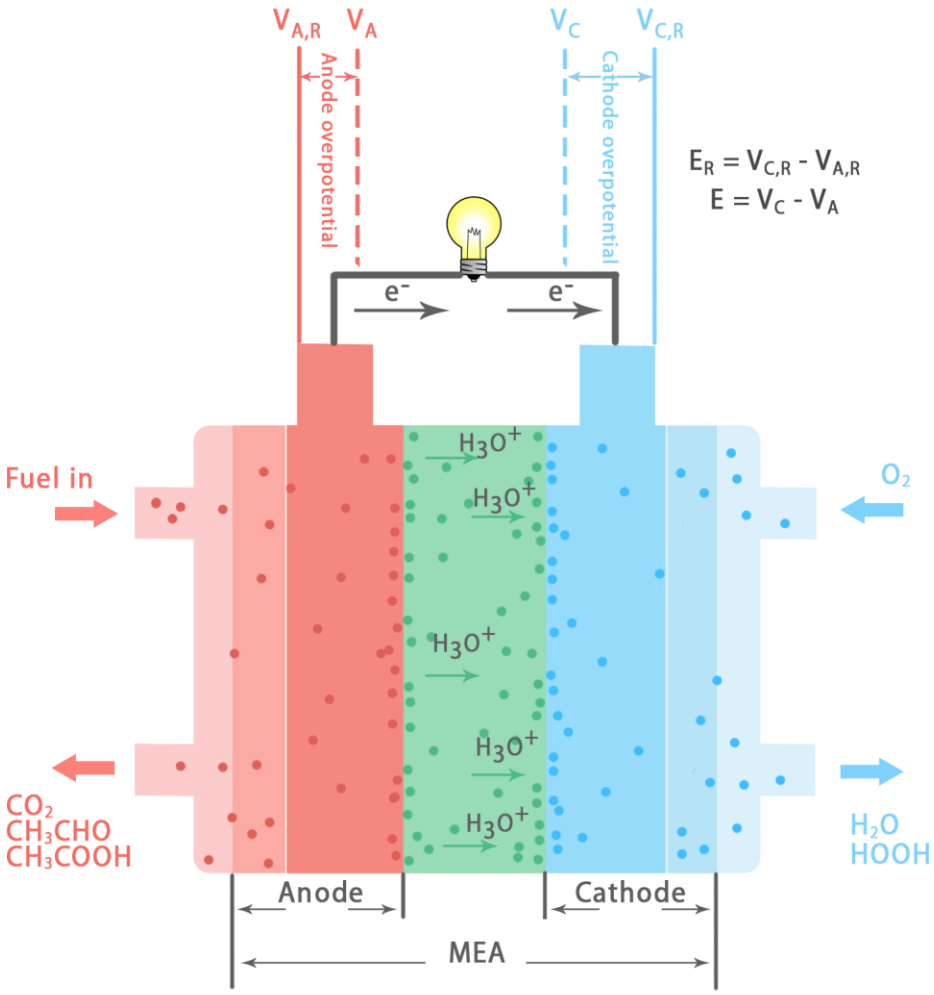

Figure 1. 3. Anode and cathode overpotentials under working conditions. The additional electrons that flow out of the anode under working conditions lead to an increase in the anode potential from $V_{A,R}$ to V_A and the accumulation of additional electrons that flow into the cathode under working conditions leads to a decrease in the cathode potential from $V_{C,R}$ and V_C. The cathode overpotential has historically been higher than the anode overpotential due to the traditional Pt catalyst being more inactive towards oxygen reduction. The existence of overpotentials causes the electromotive force E under working conditions to be less than the reversible electromotive force E_R.

As can be seen from Fig. 1.3, the existence of overpotentials has greatly diminished the electromotive force that PEMFC can output, and elimination of them has therefore been a major goal in the field. The overpotentials can be viewed as an accumulation of electron at the cathode (which decreases the reversible cathode potential) that causes the cathode to deviate from its original reversible electron-deficient state and an inadequacy of electron at the anode (which increases the reversible anode potential) that causes the anode to deviate from its original reversible electron-rich state, due to the inability of cathode catalyst of readily promoting proton-electron recombination (thus electron consumption) at the cathode-electrolyte interface and the inability of anode catalyst of readily facilitating proton-electron separation (thus electron generation) at the anode-electrolyte interface [12, 36]. Therefore, an anode catalyst that possesses higher catalytic activity towards fuel oxidation can generate more electrons at the anode thus better replenish the electrons that flows out from the anode and lower anode overpotential under operating conditions as compared to a less active anode catalyst, as will be discussed later in our study of ethanol oxidation over Pt-Mo alloy vs. pure Pt(111) anode catalysts; and a cathode catalyst that can better promote the combination of electron with O_2 though its interface with the electrolyte will better discharge the cathode of excess electrons that flow in under working conditions and thereby also lower the cathode overpotential more when compared to a less active cathode catalyst. The roles that catalytic activity of cathode catalysts play in affecting the cathode overpotential will be discussed later in our study of oxygen reduction over functional carbon materials.

To simulate the overpotentials and their impacts on the reaction mechanisms, we simulate the chemical force by solving an approximated version of the Schrödinger equation and incorporate the electric force into our system by further adding and extracting electrons from the catalyst surface. Such controlled excess or inadequacy of electrons in the system together with the homogeneous counter background charge added to maintain the overall electron-neutrality of the system will eventually lead to the establishment of electric fields that polarizes water molecules adjacent to the catalyst layer, which closely resembles the effects of the strong electronic field within the narrow electrical double layer. Instead of simulating the anode and cathode reactions all together, we take a different approach to separately simulate anode reaction and cathode reaction. By varying the number of electrons in the system, we are effectively simulating the flow of electrons in and out of the electrode. The separate studies of electrochemical reactions at anode and cathode are also consistent with the prevailing experimental approach in the field where experimentalists focus on exerting a controlled potential separately on an anode or a cathode to closely monitor the oxidation or reduction process. Further theoretical details about how we simulate the electrolyte-catalyst interface using the double reference method [34, 38, 39] are given in the method chapter.

The catalytic activities of oxidation and reduction reactions at given catalyst-electrolyte interfaces to a great extent determines the PEMFC efficiency. Besides all the advantages of modern PEMFC technologies, the commercialization and deployment of low temperature

PEMFC in recent years however has been limited by the challenges from the storage and transport of hydrogen and the costs required in the use of Pt as the active catalyst for both the anode and the cathode [5-7, 40-42]. Efforts to improve stability, portability and fuel efficiency of PEMFCs have focused on changes in fuels and operating conditions. One direction is to replace hydrogen with ethanol, which possesses a high mass-energy density and is easier to produce, store and transport [5, 41, 43, 44]. One of the leading challenges of using ethanol, however, is its low reactivity at low temperatures as the C-C bond is much more difficult to activate than H-H bond. The complete oxidation of ethanol also requires a transfer of 12 electrons ($CH_3CH_2OH+3H_2O \rightarrow 2CO_2+12H^++12e^-$) [41, 45, 46]. The catalytic activity for the oxidation of ethanol has been examined over a large number of metal catalysts, Pt, Pd, Au, Rh, Ir, Ni and Ti, and their alloys [47-60]. Pt and its alloys are the most active and widely used [42, 44, 61, 62]. The oxidation of ethanol over Pt predominantly proceeds through $2e^-$ and $4e^-$ partial oxidations to form acetaldehyde and formic acid ($CH_3CH_2OH \rightarrow CH_3CHO+2H^++2e^-$ and $CH_3CH_2OH+H_2O \rightarrow CH_3COO^-+5H^++4e^-$) under acidic conditions [44, 45], which do not undergo C-C bond cleavage. Although it is reported that Pt can indeed activate the C-C bond, the kinetics are intrinsically very slow and results in overpotentials on the magnitude of 0.5 V at a current density of 40 $mA\cdot cm^{-2}$ and ethanol concentrations of ~1.0M. The reaction is thought to proceed via step sites which are more coordinatively unsaturated [45, 61, 63, 64]. The C1 intermediates that form bind strongly to the surface Pt sites and make them unavailable for further oxidation processes [46]. All of these observations lead to the consideration of alloying Pt with other metals to tailor its catalytic activity [5, 43, 62].

Various non-precious metal-Pt bimetallic alloys have been examined [46, 65-79] and the results suggest that pairing Pt with an oxophilic transition metal such as Ru can increase its catalytic activity. Pt-Mo forms a promising pair in promoting ethanol oxidation as indicated by recent experimental studies where enhancements in both overall oxidation current and CO tolerance are observed [69, 80-85]. Several mechanisms were proposed to account for Mo's co-catalytic effect in lowering the onset potential of CO oxidation. The increased activity has been described by the formation of bi-functional sites [43, 84-88] where water is activated at the oxophilic Mo (or Ru) sites and directly interacts with the CO bound to the Pt sites on the surface, as well as by a possible electronic ligand effect [43, 84, 85, 87-89], where the neighboring Mo centers bind strongly to the Pt sites and weaken their interactions with CO thus resulting in an increased desorption of CO. Despite the significant progress, a systematic study of the effects of Mo on the different elementary steps in the oxidation of ethanol has not been carried out. In the present work, we analyze in detail the ethanol dehydrogenation, C-C cleavage and C1 oxidation steps involved in the oxidation of ethanol over Pt (111) and Pt-Mo surface alloy to understand the detailed role of Mo.

A second and perhaps more critical issue in the development of PEMFCs is the sluggish catalytic kinetics for the reduction of oxygen which occurs at the cathode. The slow kinetics requires operating the cell at much lower potentials and hence high overpotentials in order to catalytically carry out the reaction. The pathways involved in oxygen reduction carried out in acidic media are thought to proceed via the pathways presented in Fig. 1.4 [90-92].

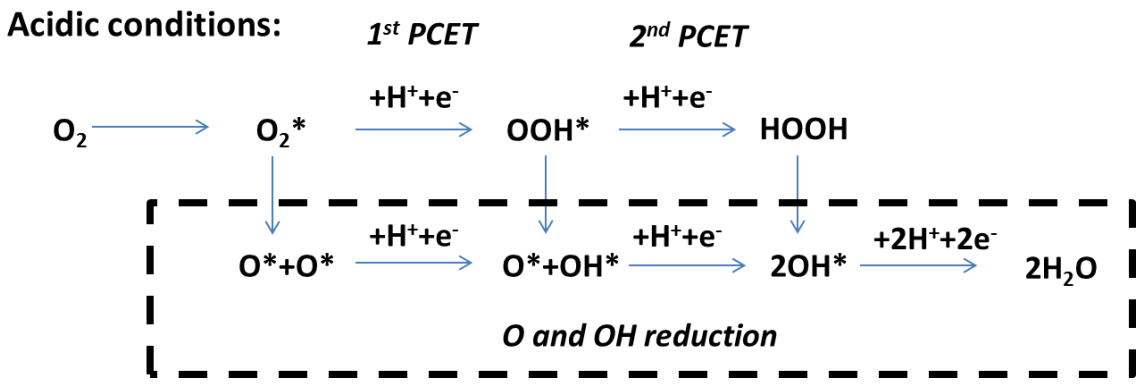

Figure 1.4. General pathways proposed for the oxygen reduction reaction over metal surfaces and metal complexes under acidic conditions. The dashed box indicates the reaction steps leading to complete oxygen reduction to water. The total number of electrons transferred during the reduction process can be determined by summing up all electrons transferred along a specific path from left to right.

The complete $4e^-$ reduction process is thought to proceed via the adsorption and activation of the O-O bond to form the hydroperoxo surface intermediate (OOH*) which is subsequently activated to OH* and O* and reduced to water as was shown in the dashed box in Fig. 1.4. The formation of the hydroperoxy species (OOH) is thought to be critical in controlling ORR kinetics [39, 93]. While Pt demonstrates the lowest overpotentials for ORR, its high cost and sluggish kinetics significantly limit its performance for PEMFC [94]. A wide range of different alternative materials composed of earth-abundant elements was studied to replace Pt to catalyze ORR [90, 95]. The most extensively studied candidates include metal free carbon substrates [96, 97] and supported nitrogen-containing organometallic complexes [98-100]. The organometallic complexes are a class of non-precious catalysts inspired by how nature carries out oxygen reduction. Cytochrome C which readily carries out ORR has been both experimentally and

theoretically examined in some detail in the literature in order to unravel the key structural and composition features that dictate its reactivity. The heme group is thought to be the active site that carries out the ATP formation process in human body where it promotes the $4e^-$ complete reduction of oxygen to water [95, 101-103]. The structure of a bovine cytochrome c [104] is shown in Fig. 1.5. Metal and nitrogen containing macrocyles and organometallic complexes such as Co and phthalocyanine have also shown reliable activities towards ORR [98, 105, 106].

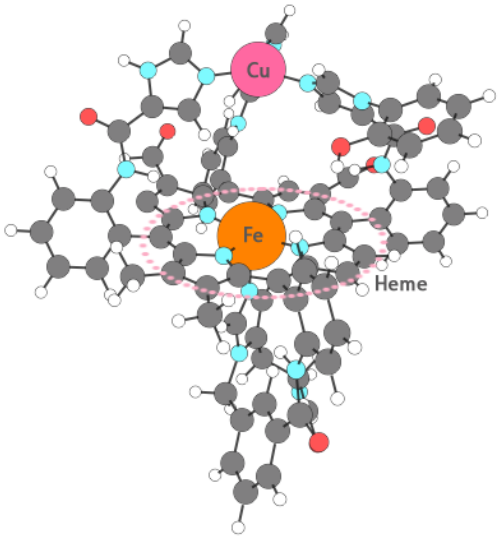

Figure 1.5. Bovine cytochrome c.

While a number of detailed efforts have been put forth to synthesize supported organometallic electrocatalysts that mimic the active site of the heme to promote the oxygen reduction process, their success has been limited. Despite the wealth of experimental studies on the synthesis and catalytic performance over homogeneous and heterogeneous metal and nitrogen containing catalysts for ORR, there are very few theoretical studies on the catalytic behaviors of these systems. We have therefore used first principle density functional theory calculations to systematically examine a series of different transition metal and N-doped carbon materials

comprised of the structural features proposed in the literature as the active site as well as other sites that mimic those found in the active cytochrome c. We examine in detail the ORR mechanism over these metal and nitrogen doped carbon substrates. More specifically we examine Fe as well as Co doped N-containing graphene substrates as well as metal-free N-doped materials [107-109]. The overall ORR pathways shown in Fig. 1.4 are examined for each of these systems in the subsequent chapters of this thesis.

In this thesis we discuss current catalytic issues that limit fuel cell development and what we will examine in the present Introduction chapter and then discuss the theoretical methods used in our work in Chapter 2. The remainder of the thesis is split into two parts, the first examines the oxygen reduction reaction at the cathode and our theoretical efforts that explore the transition metal and nitrogen doped graphene surfaces that can promote both $2e^-$ and $4e^-$ ORR under electrochemical conditions. The proton coupled electron transfer (PCET) process is examined in detail by carrying out first principle density functional theory calculations on the reaction energies and activation barriers together with detailed analyses of the effects of potential by using the double reference potential analysis method developed by Filhol and Neurock [34]. We examined in detail the elementary steps that make up the ORR mechanism over different TM-N_4-C structures that exist in basal plane of graphene (Chapter 3) and along the graphene edges (Chapter 4) and metal-free N doped carbon structures (Chapter 5). An extended study of ORR over metal-free N doped carbon structures under basic conditions was

also included due to recently observed ORR activities on these materials in basic environments [110].

In the second part of the thesis, we examine the reactions that occur at the anode for $12e^-$ ethanol oxidation mechanism over Pt and Pt-Mo surface alloys (Chapter 6). The three major paths that control ethanol oxidation chemistry at the anode which include ethanol dehydrogenation, C-C bond activation and the oxidation of the C1 intermediates that form are examined in detail over the Pt (111) surface and the Pt-Mo alloy surface. The results are used to help elucidate the mechanisms and elementary steps that control ethanol oxidation and the influence of Mo and specific alloy sites on the catalytic performance.

Chapter 2. Methods

First-principle periodic density functional theory (DFT) [111, 112] calculations were carried out to determine the energetics involved in the reduction of O_2 to H_2O_2 and water at various transition metal and N-doped carbon materials and the oxidation of ethanol over Pt and Pt-Mo alloy surfaces. All of the calculations reported herein were carried out by solving the Kohn-Sham equations [112, 113] using periodic plane wave density functional theory calculations as implemented in the Vienna ab initio simulation package (VASP) [114-116]. The exchange and correlation energy was calculated using the Perdew-Wang 91 (PW91) [117] form of the generalized gradient approximation. The core electrons were described using projector augmented wave (PAW) potentials [118] along with a cutoff energy of 396 eV to define the plane-wave basis sets. Electronic self-consistent field (SCF) iterations were converged to 1.0×10^{-5} eV. A 3x3x1 Monkhorst-pack k-point mesh was used to sample the Brillouin zone and ensure adequate computational accuracy. In the calculations for ORR over metal and nitrogen doped graphene surfaces presented in Chapters 3, 4 and 5, the distance between the graphene layers which defines the cell and the aqueous interface was chosen to be 15 Å to provide an adequate number of water molecules to appropriately solvate the protons used to carry out the reduction reactions and negatively charged surface intermediates while allowing for some degree of computational efficiency. The water molecules at the top of the unit cell were kept ~4Å away from the top graphene to avoid interactions between the different layers. More

accurate simulations of the aqueous/graphene interface would require simulating the hundreds of thousands of configurations along the reaction coordinate for each elementary step at constant potential which is computationally intractable. To provide a more assessable approach, we examine the reactions using an optimized aqueous/graphene interface. The optimized water/graphene interface used is determined by carrying out ab initio molecular dynamics simulations by starting with a well-defined ice/graphene interface and carrying out simulated annealing simulations which increase the temperature from 0 K to 350 K (the average working temperature for PEMFC) for 500 fs and then cool the system back to 0 K. The optimized water/graphene interface was used in all subsequent calculation to determine the energies for all of the reactant, intermediate and product structures.

The calculations reported for the oxidation of ethanol presented in Chapter 6, were carried out over the Pt (111) and Pt-Mo (111) surfaces. The surfaces were simulated using a 3X3 unit cell containing four metal layers, with the bottom two layers of the metal slab fixed to simulate bulk metal while the top two layers relaxed for interaction with adsorbates. A distance of 20 Å between consecutive z-direction slabs was used to avoid adjacent metal slabs from interacting across the vacuum region. All the calculations were carried out by allowing for full structural optimization of all of the atoms in the system to within a convergence criterion of 0.05 eV/Å. We found that increasing the convergence criterion for ionic relaxation from 0.05 eV/Å to 0.01 eV/Å resulted in changes in the reaction energies of less than 0.02 eV for all the key structures in the ORR process.

Electrochemical systems are defined as constant potential (grand canonical) systems. Most quantum chemical methods, however, are defined as constant electron (canonical) systems. Herein we used the double reference method developed by Filhol and Neurock, to simulate constant potential systems and determine the potential dependent energies for the elementary steps involved in the reduction of O_2 to hydrogen peroxide and water [34]. The double reference method carries out a series of calculations where the number of electrons within the system are increased (or decreased) in order to systematically increase (or decrease) the system potential. The fractional charge that is added (or removed) is localized on the electrode surface. An equal but opposite charge is then distributed across the unit cell in order to maintain charge neutrality. The charges act to polarize the water molecules at the interface and to create an electrochemical double layer which closely mirrors the double layer defined by using actual ions from an aqueous electrolyte [1]. The potential in the system can be calculated by referencing the calculated potential to that required to remove an electron from the Fermi level of the electrode into the gas phase and subsequently referencing the charged system to the neutral system.

The potential of the aqueous/graphene system with charge q, φ_q, is calculated according to the following formula:

$$\varphi_q = \varphi_q(f) - \varphi_q(w) + \varphi_0(w) - \varphi_0(f) + \varphi'_0(f) - \varphi'_0(v) \quad (2.1)$$

where the subscripts q and 0 refer to the charged and uncharged states of the system, and f, w and v refer to the potential with reference to the Fermi level of the graphene electrode, the

potential with reference to the water molecules in solution and the potential with reference to the vacuum. The last two terms are electrode Fermi level and vacuum references in the vacuum reference cell respectively. The absolute potential φ_q can then be referenced to the normal hydrogen electrode (NHE) U_q by subtracting the work function for the H_2/H^+ couple on Pt under standard conditions [39]:

$$U_q/V = -4.8 - \varphi_q/eV \quad (2.2)$$

The self-consistent energies for the charged systems are subsequently corrected to eliminate the influence of the homogeneous counter charge imposed by the ab-initio calculation.

By varying the charge we can examine the free energy of the system in a given state as a function of potential. In order to follow the reaction behavior we analyze the potential dependent changes in the energies for the reactant and product states for a particular reaction. A more detailed discussion associated with calculating the potentials and the grand canonical energies using the double reference method is given in the following references [34, 38, 39].

Chapter 3. Potential Dependent Analyses of Oxygen Reduction over Fe/Co and Nitrogen-Doped Graphene Basal Plane Substrates

Many of the current issues that prevent the commercialization of polymer electrolyte membrane (PEM) fuel cells which include cell efficiencies, materials cost and catalyst durability arise from Pt electrocatalysts that are used to reduce oxygen on the cathode side of the cell [119, 120]. Significant efforts over the past decade have been focused on the development of Pt-based alloys that show increased activities [121], and in addition to establishing alternative materials comprised of earth-abundant materials that can replace Pt [90, 95]. The latter includes metal free carbon substrates [96, 97], nitrogen-doped graphene, carbon nanotubes and nanoribbons [93, 122-124] and supported nitrogen-containing organometallic complexes [98-100]. Our efforts herein presented in this chapter are focused on the transition metal nitrogen-doped carbon (TM-N-C) materials.

Many of the transition metal and nitrogen doped carbons were initially derived by pyrolyzing Fe-N_4 and Fe-N_6 porphyrin structures and other organometallic complexes that mimic the active sites found in heme responsible for catalyzing oxygen reduction during ATP formation process in biological systems [94, 95, 101-103, 125-127]. Other transition metals and nitrogen-containing macromolecules such as cobalt and phthalocyanine were recently shown to also demonstrate catalytic activity towards ORR [98].

Due to the challenges in synthesizing N-containing porphyrin macromolecules, many of the recent efforts have focused on using other nitrogen precursors. Yeager and coworkers, for example, successfully replaced porphyrin with polyacrylonitrile (PAN) by pyrolyzing PAN and Fe(II)/Co(II) salts together with high surface area carbon [128]. Yang and Liu used chemical vapor deposition to synthesize carbons which contain transition metal ions that are thought to be coordinated to four pyridinic nitrogen in square planar-like structures embedded into basal plane of ACNT [129, 130]. Subsequent cyclic voltammetry (CV) studies showed rapid increases in ORR current when the potential was decreased to 0.7 V vs. NHE. Dodelet recently synthesized active TM-N-C materials in which the Fe/Co-N_x active centers reside at the interstices between graphitic sheets by pyrolyzing a ball-milled mixture of phenanthroline, carbon and ferrous acetate twice, first in argon and then in ammonia [131, 132]. The resulting catalyst demonstrates significant ORR activity at IR-free cell voltages of ~0.9 V which begins to rival to that of the traditional Pt/C catalyst [131-134]. Wu and Zelenay also achieved high ORR activity on a class of polyaniline (PANI) derived non-precious metal cathode catalysts. They found a radical enhancement in ORR activity and $4e^-$ selectivity upon the introduction of Fe or Co into the heat-treated PANI-C substrate, with an ORR onset-potential of 0.93 V vs. the reversible hydrogen electrode (RHE) and a yield of H_2O_2 less than 0.5% observed for the best PANI-Fe-C and PANI-FeCo-C samples [135-137].

While the detailed structure of the active sites and the mechanisms that control ORR are still debated, detailed characterization analyses over a wealth of different metal and N-doped

carbon substrates under working conditions have helped to establish the different sites present and provide insight into their potential reactivity. X-ray photoelectron spectroscopy, time of flight secondary ion mass spectroscopy (ToF SIMS) analyses indicate that the active sites involve Fe^{2+} and Co^{2+} centers coordinated to 4 pyridinic nitrogens in the general form of M-N_4 [138, 139]. ToF SIMS results indicate that the two most abundant fragments are $FeN_4C_8^+$ and $FeN_2C_4^+$ structures [139]. The latter is not stable alone and coordinates with two nitrogens at another carbon edge to form the MN_{2+2} site. Recent studies using Mossbauer and Extended X-ray Absorption Fine Structure (EXAFS) spectroscopy by Dodelet [140] carried out to elucidate the structure and magnetic properties of the Fe centers under working conditions suggest that the most active M-N_4 sites are high spin FeN_{2+2} sites that exist at the edges of the basal planes of graphene and within microporous carbon environments.

ORR is thought to proceed at the M-N_4 or M-N_{2+2} sites by the adsorption and activation of O_2 followed by a series of proton-coupled electron transfer (PCET) steps that reduce the bound O_2 to water [99, 141]. The specific elementary steps and mechanisms, however, are unclear. Experimental observations indicate that ORR occurs over the TM-N-C materials through different pathways depending on different choices of the central transition metals. Fe typically catalyzes 4 electron reduction of O_2 to form H_2O [99, 135, 142, 143]. Co, however, which is also active can only catalyze the 2 electron reduction of O_2 and thus predominantly forms H_2O_2 [144-147]. Recent studies carried out with Co-porphyrin macromolecules indicate that Co can also catalyze the 4 electron reduction of O_2, if it's ligated with specific functional groups such as Ru-

pyridine complex [148], or two Co-porphyrin units to provide a co-facial configuration that can accommodate the necessary Co-O-O-Co transition state [146, 149-151]. Two metal centers are thought to assist the proton coupled electron transfer in mechanisms similar to the bi-functional Fe-Cu sites found in cytochrome c [104, 152]. These bi-functional Co and Fe sites, however, are not present in the Fe/Co N-doped graphene substrates.

First principle density functional theoretical calculations were carried out herein to examine the elementary steps and the possible mechanisms involved in the reduction of oxygen over Fe/Co N-doped model graphene surfaces shown in Fig. 3.1. The model structure has the central TM coordinated to four pyridinic nitrogen atoms simulating the structure of heme. The oxygen reduction reaction can proceed through a sequence of elementary steps involving, in general, the adsorption of O_2 (O_2*), electrochemical reduction of adsorbed O_2, the direct or PCET-assisted activation of O_2 and the subsequent reduction of the atomically adsorbed O (O*) and OH (OH*) intermediates that form, where the * is considered an adsorption site. These steps can be organized into two parallel PCET routes involving the reduction of O_2H_x and OH_x intermediates together with O-O activation steps to describe the $2e^-$ and $4e^-$ ORR that occurs under acidic conditions as shown in Fig. 1.4 and presented previously [90-92].

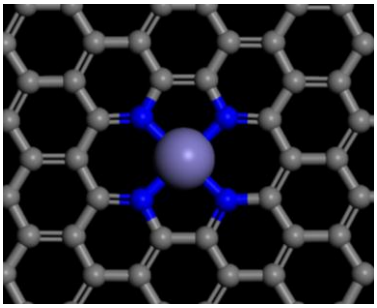

Figure 3.1. Fe/Co-N_4 graphene basal plane active site.

In the following sections we examine in detail the role of the transition metal and the influence of water and potential on ORR mechanisms for acidic PEMFC environments over model Fe-N_4 and Co-N_4 active sites impregnated into the basal plane of grapheme shown in Fig. 3.1. More specifically we examine the adsorption of O_2, the 1st and 2nd PCET reductions of O_2 and the PCET reduction of the O and OH intermediates that form and how they change as a function of potential.

3.1. Oxygen Adsorption and Direct O-O Bond Activation

The oxygen reduction reaction proceeds by the adsorption of molecular O_2 to the Fe^{3+} or Co^{3+} site in either an end-on configuration as a superoxo (O_2^{1-}) intermediate or a side-on configuration as a peroxo (O_2^{2-}) intermediate. The superoxo intermediate is thought to be more selective towards the overall 4 electron reduction to form water over the partial 2 electron reduction to hydrogen peroxide as it regulates the proton delivery together with multiple

electron transfer steps [151, 153, 154]. This aids in bypassing the overall 2 proton – 2 electron transfer paths that result in H_2O_2 formation.

Herein we examine the adsorption of O_2 in both the end-on configuration to form the superoxo intermediate and the side-on configuration to form the peroxo intermediate. The optimized structures and potential dependent energy profiles for both species along with the initial energies for the O_2 (g) + aqueous/graphene system are summarized in Fig. 3.2. We examine a wide range of potentials between 0 to 2 V v.s. NHE.

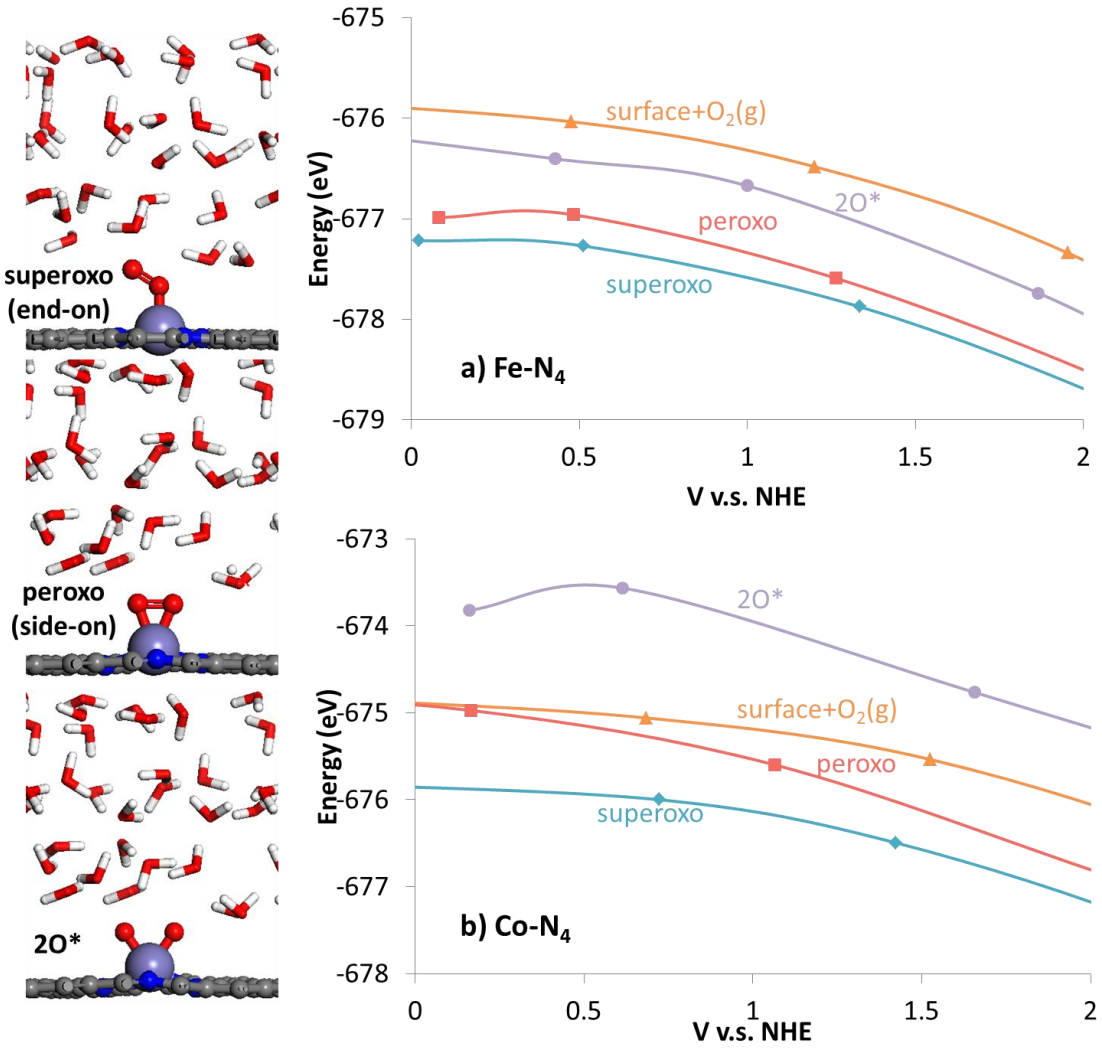

Figure 3.2. The adsorption of O_2 in superoxo (end-on) and peroxo (side-on) configurations and the direct dissociation to form two metal-O species as a function of potential on a) Fe-N_4 and b) Co-N_4 graphene basal plane.

Molecular oxygen can readily adsorb on both the Fe-N_4 and Co-N_4 sites to form stable superoxo (end-on) and peroxo (side-on) intermediates as can be seen in Fig. 3.2a and 3.2b. Both the end-on and side-on O_2 adsorption curves lie below that of free surface state where O_2 is in the gas phase (surface + O_2 (g)) over the entire potential range examined (0 - 2 V v.s. NHE), indicating

the O_2 adsorption is exothermic at both Fe and Co-N_4 active sites. The adsorption of O_2 in the superoxo (end-on) configuration is favored over the peroxo (side-on) configuration at both the Fe-N_4 and the Co-N_4 sites over the wide range of potentials examined. This can be understood by the fact that both Fe and Co adopt the d^2sp^3 hybridization that typically results in 6-coordinate octahedral configurations. The end-on adsorption which results in a single electron transfer results in a more favorable configuration. The direct activation of the O-O bond is over 0.9 and 2.0 eV higher in energy than the molecularly adsorbed O_2 state at the Fe-N_4 and Co-N_4 sites, respectively as is shown in Fig. 3.2a and 3.2b. The activation of O_2 results in the formation of two strong M-O bonds which bind strongly to the metal center and pull it up out of the graphene plane. The activation of O_2 over the Co-N_4 site was found to be even more difficult than over the Fe-N_4 site as it is over 1 eV higher than the gas phase O_2(g) + Co-N_4 state as shown in Fig. 3.2b. We find throughout all of the systems we've studied herein that Co is less effective than Fe in activating the O-O bond as will be highlighted in the sections 3.2 and 3.3 on the activation of OOH.

3.2. Reduction of Adsorbed Molecular Oxygen and Direct Dissociation of Adsorbed Hydroperoxy (OOH*)

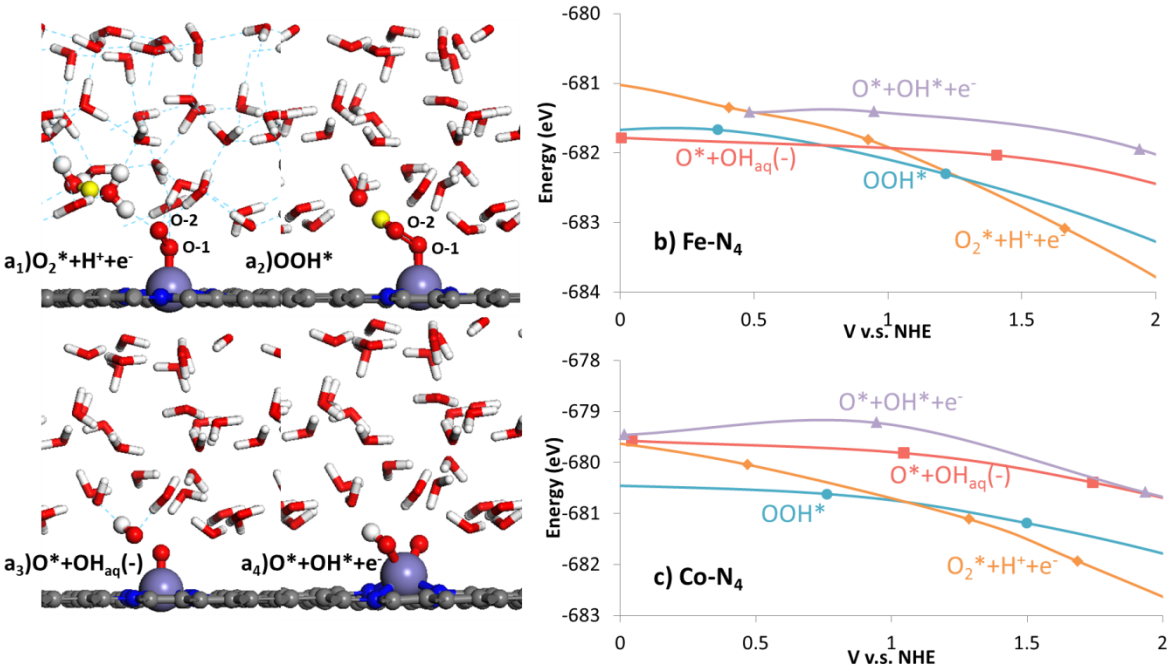

Figure 3.3. The reactant and product states for the reaction of O_2* + H^+ + e^- , where the proton shown in yellow is near the adsorbed O_2 (a_1), the OOH* (a_2) intermediate and the dissociation of OOH* to form O* + $OH_{aq}(-)$ (a_3) and O* + OH* + e^- (a_4) where * refers to the adsorbed intermediate to the metal-N_4 sites that reside in the graphene basal plane. $O\text{-}_1$ denotes the oxygen atom directly binding to TM in the end-on adsorption state and $O\text{-}_2$ denotes the terminal oxygen atom not directly binding to TM. The potential dependent reduction curves for each of the states reported in a_1 to a_4 are shown on Fe-N_4 and Co-N_4 active sites in b) and c) respectively. The energy differences between each of the reported states provide the relevant reaction energies.

Adsorbed O_2 does not directly dissociate as was shown above, but instead is reduced to a peroxo species which is considered to be a key intermediate in both $2e^-$ and $4e^-$ oxygen reductions to form hydrogen peroxide and water, respectively [39, 93]. The reaction proceeds via a proton-coupled electron transfer process as was highlighted in Fig. 3.3 a_1 and a_2 involving a proton (shown in yellow) transfer through water to the terminal oxygen atom ($O\text{-}_2$) of the

end-on adsorbed di-oxygen molecule together with a direct electron transfer from TM to the π^* state on adsorbed O_2. The cross-over in energy from the $O_2+H^++e^-$ and the OOH* curves at the Fe-N_4 site (Fig. 3.3b) occurs at 1.2 V, while the crossover in these curves for the Co-N_4 site (Fig. 3.3c) occurs at a slightly lower potential of 1.1V, indicating a lower catalytic activity of the Co-N_4 site in facilitating OOH* formation.

While both the Fe-N_4 and Co-N_4 sites promote hydroperoxo (OOH*) formation, they are rather different in their subsequent activation of the OOH* intermediate. The OOH* intermediate can either dissociate to form O* and OH* or can react to form a metal-oxo (O*) along with an aqueous phase hydroxyl intermediate the reacts in acidic media to form water. The energies for the O*+OH* and the O*+OH_{aq}(-) paths are shown in Fig. 3.3b and 3.3c in purple and red curves respectively. The dissociation to form the bound O* and OH* is energetically unfavorable on both Fe-N_4 and Co-N_4 sites as the metal is pulled out from the surface to form strong M=O and M-OH bonds similar to that found for the direct dissociation of O_2*.

The activation of OOH* to form the metal-oxo (O*) and OH_{aq}(-) intermediate that protonates in solution is also not favorable at the equilibrium potential of 1.2 V vs. NHE on either Fe-N_4 or Co-N_4 sites. As the potential is decreased to 0.7 V vs. NHE, there is, however, a crossover of the OOH* and O*+OH_{aq}(-) states for Fe-N_4 system as shown in Fig. 3.3b which indicates that this reaction can readily proceed as the potential is decreased to 0.7 V vs. NHE at the Fe-N_4 sites. This is consistent with recent cyclic voltammetric results [129, 130] which show that pyridinic

nitrogen coordinated Fe sites embedded into aligned carbon nanotubes result in significant ORR currents at cathode potential of 0.7 V vs. NHE. The activation of the OOH* intermediate does not occur at the Co-N_4 site at any of the potential examined herein as is shown in Fig. 3.3c where the OOH* curve is the lowest energy state from 0 to 1.1 V vs. NHE. This is consistent with experimental observations that show that the single Co-N_4 site is not active in dissociating the O-O bond but instead promotes the $2e^-$ reduction process to form hydrogen peroxide [144-146]. A more thorough molecular orbital analysis is carried out in section 3.5 to provide a more detailed understanding of the O-O activation over the Fe and Co-N_4 centers.

3.3. Reduction vs. Dissociation of Adsorbed Hydroperoxy (OOH*)

In addition to the direct dissociation of OOH* just discussed, the hydro-peroxo intermediate (OOH*) can react with a second hydrogen at the O_{-1} position to form adsorbed hydrogen peroxide (HOOH*). Potential dependent DFT calculations indicate that the hydrogen can also add to the O_{-2} position to form an M-O-OH_2* intermediate with a significantly weakened O-O bond that can rapidly decompose to metal oxo (O*) and H_2O. We have therefore explored the potential dependent energies for the three states that are involved in the $OOH^*+H^++e^- \rightarrow$ HOOH* and the $OOH^*+H^++e^- \rightarrow O^*+H_2O$ processes.

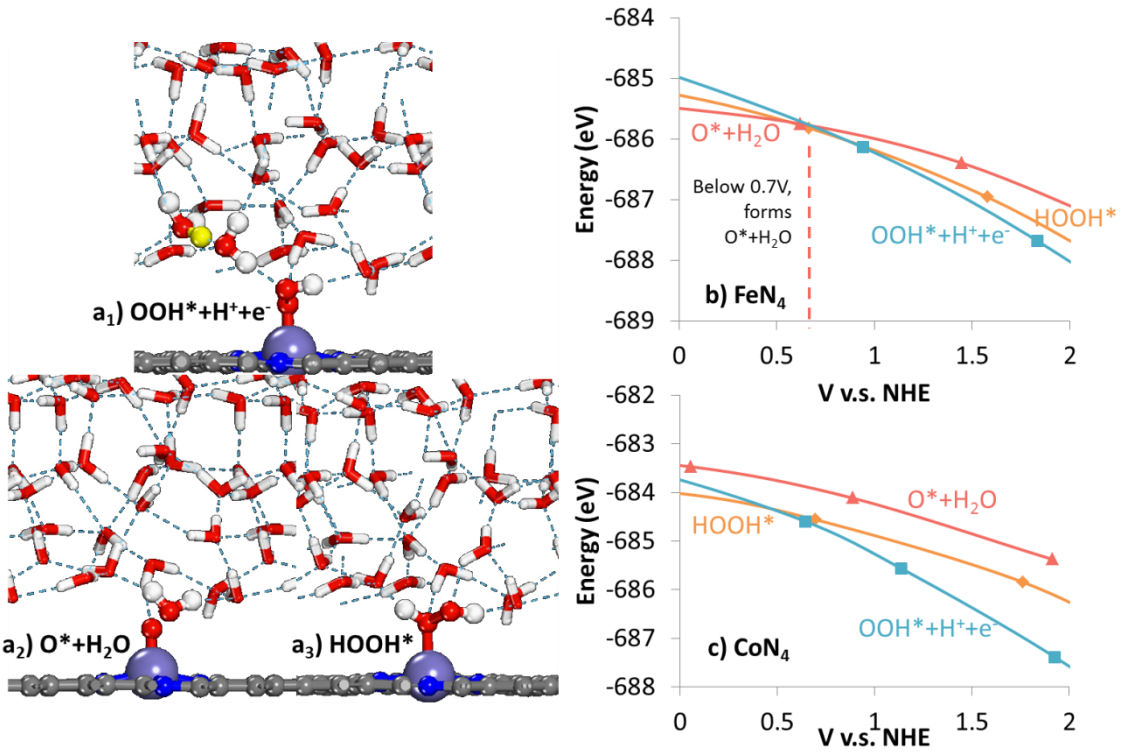

Figure 3.4. Hydrogen addition to either O_{-1} of OOH* that forms HOOH* (a_3) or O_{-2} of OOH* that leads to decomposition to O* and H_2O (a_2) on b) Fe-N_4 and c) Co-N_4 active sites.

The OOH*+H^++e^- state can react via a proton coupled electron transfer to the internal O_{-1} site to form adsorbed hydrogen peroxide (HOOH* shown in Fig. 3.4 a_3) which can subsequently desorb and completes the 2e^- reduction process. Alternatively, OOH* can undergo a proton-assisted activation of the O-O bond to form the metal-oxo species and water, M=O + H_2O (a_2, Fig. 3.4). The DFT-calculated potential energy curves for the HOOH* and O*+H_2O product states which represent the two different hydrogen addition paths (H to O_{-1} and H to O_{-2}) shown in both Fig. 3.4b and 3.4c indicate that O-O bond activation occurs at 0.7 V vs. NHE at the Fe-N_4 site but is prohibited on Co-N_4 active site over the wide range of potentials examined (0 - 1.2 V vs. NHE). The HOOH* intermediate is the only favored product species on the Co-N_4 site below 0.5V. This

is very similar to the results we reported in section 3.2 for the PCET activation of M-O_2. This suggests that the activation of O-O bond of M-O_2 is not influenced very much by the presence of additional protons and electrons. The results indicate that the Fe-N_4 active site readily promotes the $4e^-$ reduction of O_2 to H_2O at 0.7 V immediately following the formation of OOH*. In the reduction of O_2 at the Co-N_4 site, H_2O_2 is stable over a wide potential range and that PCET is decoupled from the O-O dissociation process. These results again are consistent with recent experimental observations showing that on Co-N_4 active sites, oxygen predominantly react via a $2e^-$ reduction route to form H_2O_2 [144-146], while the Fe-N_4 sites can further activate the O-O bond via the $4e^-$ reduction route [135, 137, 142], and promotes ORR at higher potentials than Co-N_4 [135].

The O-O bond activation process generates O* and OH* intermediates that are reduced to water and desorbed from the surface to regenerate the active sites.

3.4. O* reduction and OH* reduction

The final O* and OH* reduction steps which complete the $4e^-$ reduction path were examined only on the Fe-N_4 active site as the Co-N_4 site does not appear to dissociate O_2 and as such do not lead to the formation of O* and OH* but instead result in formation of hydrogen peroxide as discussed above. The Fe=O and Fe-OH intermediates that are formed as a result of the

activation of OOH* intermediates strongly bind to the Fe center. The first step in the reduction of the Fe=O intermediate involves a proton-coupled-electron transfer to form Fe-OH which is subsequently reduced to form water. The potential-dependent free energies of the Fe=O and Fe-OH states along with the final Fe-OH_2 product at the Fe-N_4 site are shown in Fig. 3.5.

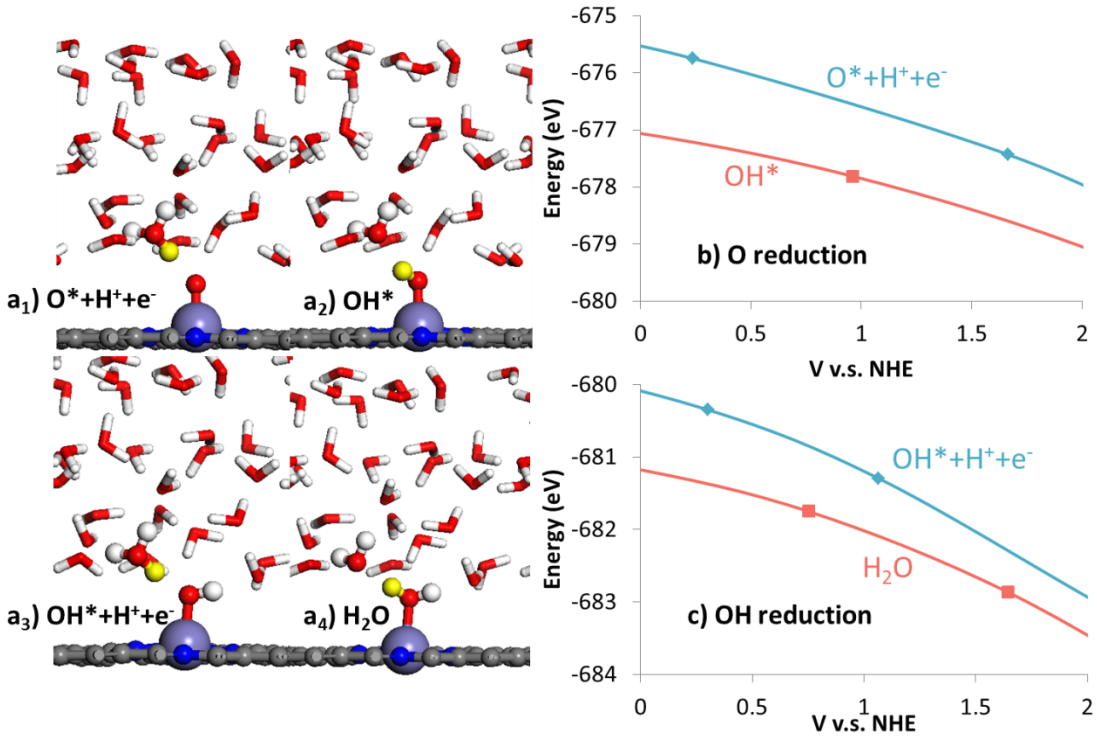

Figure 3.5. The Fe=O reactant (a_1) and Fe-OH product (a_2) in the initial reduction of Fe=O to Fe-OH and the Fe-OH reactant (a_3) and Fe-OH_2 product (a_4) in the subsequent reduction of Fe-OH to Fe-OH_2 at the Fe-N_4 site. The potential dependent free energies as a function of potential for the reduction of Fe=O to Fe-OH and Fe-OH to Fe-OH_2 are shown in (b) and (c).

The results shown in Fig. 3.5b and 3.5c clearly show that the reduction of both Fe=O to Fe-OH and subsequent reduction of Fe-OH to Fe-OH_2 are favored over the wide range of potentials examined as the Fe-OH and Fe-OH_2 product curves are lower by 1.3-1.5 eV and 0.9-1.2 eV than

the Fe=O and Fe-OH reactants, respectively. The Fe=O reduction is favored over the Fe-OH reduction by ~0.3-0.4 eV.

3.5. Band Decomposition Molecular Orbital Analysis

A more detailed and in depth understanding of the differences in catalytic activities of Fe and Co in the reduction and activation of O_2 can be given by analyzing the changes in geometric structure and by carrying out a decomposition of the electronic band structure.

The calculated O-O bond lengths for O_2 (g), Co-O_2 (end-on), Fe-O_2 (end-on), OOH (g), Fe-OOH, Co-OOH and HOOH (g) at charge zero are summarized in Table 3.1.

	O_2 (g)	Co-O_2 (end-on)	Fe-O_2 (end-on)	OOH (g)	Co-OOH	Fe-OOH	HOOH (g)
O-O bond length (Å)	1.236	1.325	1.330	1.348	1.459	**1.499**	1.470

Table 3.1. O-O bond lengths for the gas phase and Fe and Co coordinated O_2, OOH and HOOH species on Fe/Co-N_4 sites.

As might be expected, the O-O bond length increases with the addition of each H as the reaction order changes from 2 to 1. The addition of each proton is accompanied by an electron transfer from the metal into O_2 π^* antibonding states thus giving rise to the increase in the O-O bond length. The Co-O_2 and Fe-O_2 have O-O bond lengths of 1.325Å and 1.330Å which are significantly longer than that of O_2 (1.236Å) but very close to that of OOH (1.348Å, where there is a complete single electron transfer from hydrogen). This is indicative of a single electron transfer from the Fe^{II} (or Co^{II}) to antibonding O_2 states and the oxidation of the metal to Fe^{III} (or Co^{III}). Similarly the O-O bond lengths of Co-OOH and Fe-OOH (1.459Å and 1.499Å) are very close to that of HOOH (1.470 Å) which indicate a total of two electron transfer from TM to the O-O bond. The HO-OH bond is rather weak due to the occupation of the two O-O π^* states which include the highest occupied molecular orbital (HOMO) and next highest molecular orbital (HOMO-1)) of HOOH as is shown in Fig. 3.6a.

The Fe-OOH intermediate has an O-O bond that is 0.029 Å longer than the O-O bond of HOOH. This arises from the backdonation of electrons into the π^* states (HOMO, HOMO-1 and lower occupied states) as well as into the σ^* states (HOMO-2 and HOMO-3) as is shown in Fig. 3.6b which significantly weakens the O-O bond.

The O-O bond for Co-OOH, on the other hand, was found to be 0.011 Å and 0.04 Å shorter than that for HOOH and Fe-OOH. Despite the shorter distance, there is still direct occupation of the O-O π^* (HOMO and HOMO-1) and σ^* (HOMO-2) states as is shown in Fig. 3.6c.

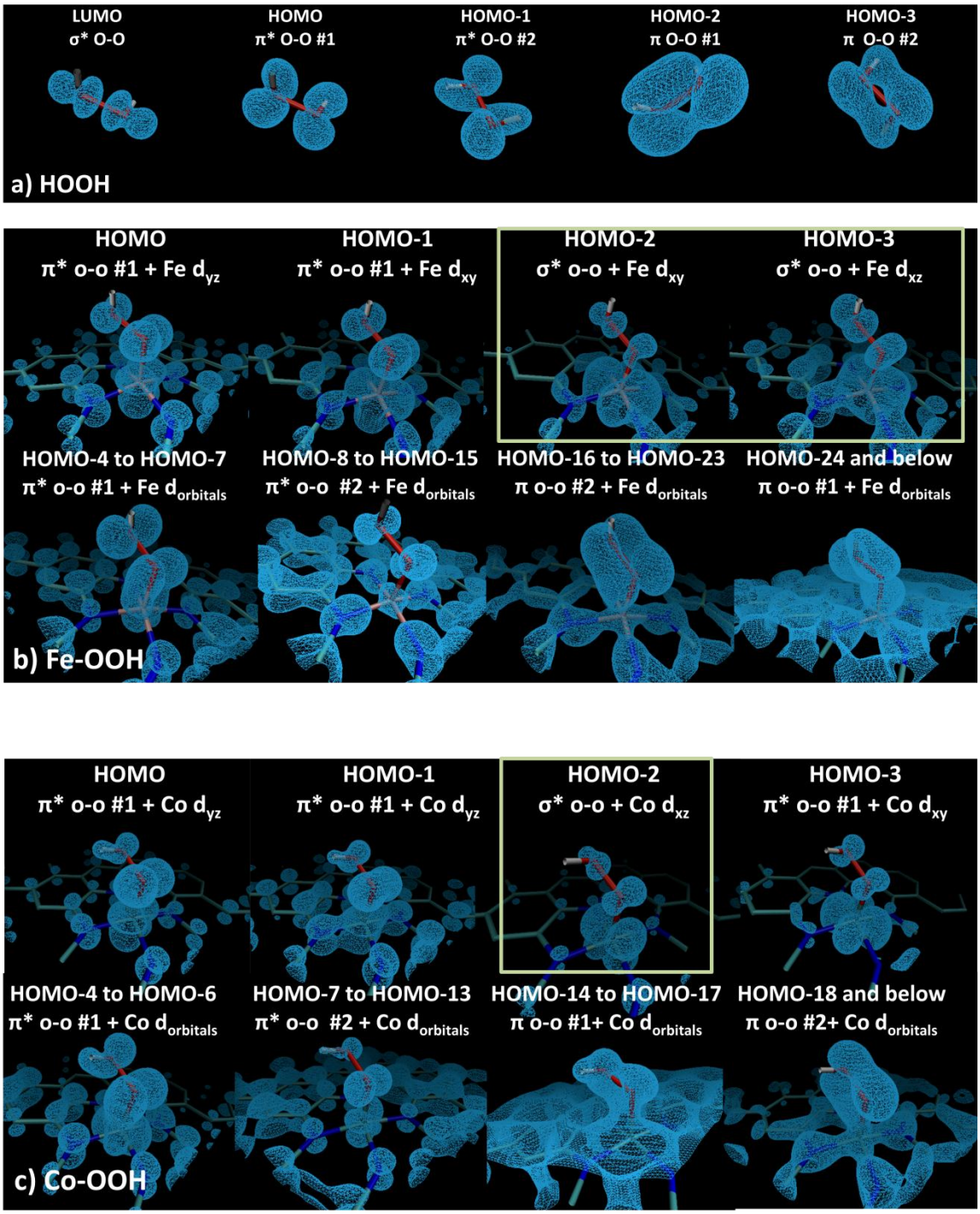

Figure 3.6. Band decomposition analysis for: a) HOOH, b) Fe-OOH and c) Co-OOH. HOMO-n indicates the nth occupied molecular orbital below HOMO. Each band in b) and c) is observed as a combination of an O-O orbital and a metal d orbital. The electron density is mapped using an isovalue of 0.01 e/Å^3.

A Bader charge analysis was carried out by projecting the electron densities for each of the bands onto the oxygen atoms to determine the number of electrons that were transferred to the antibonding O-O σ* and π* states. The results are presented in Table 3.2.

	σ* O-O	π* O-O	Total (σ* +π*)
Fe-OOH	0.48e	3.36e	3.84e
Co-OOH	0.15e	3.45e	3.60e

Table 3.2. Electron occupancy of the σ*, π* and Total (σ*+π*) O-O orbitals calculated by projecting bands onto the oxygen atoms.

The total electron transfer to the antibonding states of O_2 for both the Fe-OOH and Co-OOH systems (3.84 e for Fe-OOH and 3.60 e for Co-OOH) were calculated to be very close to that of HOOH (4e) which helps to explain the very similar O-O bond lengths for Fe-OOH, Co-OOH and HOOH reported in Table. 3.1. Fe shows a greater degree of electron transfer from the metal into the O-O antibonding π* and σ* states (3.84 e) than that of Co (3.60 e). This is generally consistent with the fact that Fe is less electronegative than Co. The Fe-OOH system also results in 0.33e greater charge transfer to the σ* O-O state than that of Co. The greater extent of electron transfer to the antibonding O-O σ* state increases the O-O lengths on Fe and favors the $4e^-$ oxygen reduction on Fe. This is consistent with the suggestions that active $4e^-$ reduction

systems involve increased electron transfer upon the delivery of the first proton [151]. The degree of charge transfer to the O-O σ* and the overall degree of charge transfer on Co is less than that on Fe and also less than that for HOOH. This helps to explain the high energetic penalties associated with dissociating the O-O of Co-OOH and the more favorable $2e^-$ reduction path.

The results reported in Table 3.1 and 3.2 also show that the occupation of the σ* O-O orbital weakens the O-O bond more than the occupation of the π* O-O orbital does. These observations are consistent with recent work showing that the electrophilicity of σ* O-O is closely related to reactivity for various processes involving O-O bond cleavage [155, 156], where interactions between the O-O bond and reaction environment lowers the σ* O-O state to below that of the lowest unoccupied molecular orbital thus promoting O-O activation.

3.6. Conclusion on ORR over TM-N4 basal plane systems

The potential dependent elementary steps involved in the oxygen reduction reaction were examined over model Fe/Co-N_4 graphene basal plane active sites. The results indicate that both Fe and Co-N_4 active sites favor the end-on oxygen adsorption to form a superoxo species over the side-on peroxo intermediate and promote the proton-coupled electron transfer to bound O_2 thus resulting in the formation of the hydroperoxy intermediate at around 1.2V v.s NHE. The

Fe-N_4 site induces a greater degree of electron transfer to antibonding σ* state that subsequently promotes a second PCET step which aids in the dissociation of O-O to form Fe(V)=O and water at around 0.6 V. The Co-N_4 site, however, cannot dissociate the O-O bond of Co-OOH but instead reduces the OOH to form the $2e^-$ product HOOH. The results are consistent with those from experiments which observe only the $2e^-$ ORR to form hydrogen peroxide on Co-N_4, while Fe-N_4 promotes a complete $4e^-$ ORR to form water with only trace amount of hydrogen peroxide detected. The resulting single oxygen species that form can readily be reduced at the Fe-N_4 active site to complete the $4e^-$ reduction. More detailed molecular orbital analyses show that at the Fe-N_4 site the energy of the σ* O-O state is lowered below the HOMO state on the Fe-N_4 thus allowing for the backdonation of electrons into this state which weakens the O-O bond and allows for direct dissociation. The degree of backdonation from the Co-N_4 site to the bound O_2 and OOH* is significantly less than that for Fe-N_4 and as a result it does not promote subsequent O-O activation and instead results in the $2e^-$ path that leads to HOOH formation [157, 158].

Chapter 4. Oxygen Reduction Reaction over Fe-N_4 sites between graphene edges

Recently, Dodelet and coworkers demonstrated the synthesis of Fe-N_4 sites that are reported to exhibit considerable catalytic activity and durability for ORR via sequential pyrolysis [131-133]. They pretreat the carbon support by ball-milling it with phenanthroline and ferrous acetate, which leads them to believe that the active site is located between armchair graphene edges of the carbon substrates. The polarization curve showed that the cathode ORR current density on their Fe-N_4 graphene edge material with a 5.3 mg/cm^{-2} loading is equal to that of the traditional Pt catalyst with a 0.4 mg/cm^{-2} loading at 0.9V iR-free cell voltage. The overall cost of catalysts, however, is significantly lower [131]. Graphene edges possess distinctly different electronic structures than those on the basal planes of graphene, which can contribute to changes in the catalytic activity of the TM-N_4 sites due to the interaction between the edges and the central TM via the doped nitrogen atoms. However, how changes in graphene edge structures result in different interactions with the TM center and thus different ORR activities remains unclear. Also, a study of possible tuning of the ORR activity via ligation to the TM center from additional N-containing ligands is missing from literature. Such an additional N-containing ligand to the active TM center does exist in the natural cytochrome c enzyme structure though [104]. To study these effects, we propose the following three systems featuring an Fe-N_4 active site

located between two armchair graphene edges with varying edge gaps, and a third system featuring an edge Fe-N_4 site possessing an additional pyridine ligand.

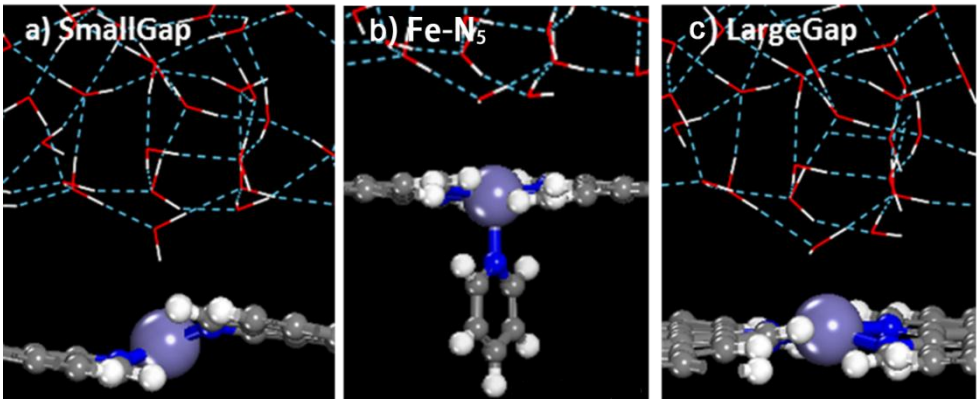

Figure 4.1. Fe-N_4 graphene edge sites with a) small edge gap, b) additional ligand and c) large edge gap.

Our calculations indicate that there is a transition in structure at the edges as the distance between the two edges is decreased. As the distance in the graphene edge falls below 3.1 Å there is a change in the edge structure which buckles away from the planar edge state shown in Fig. 4.1c to the staggered edge geometry, shown in Fig. 4.1a. Under experimental conditions, both cases are expected to exist. The additional pyridine ligand shown in Fig. 4.1b is thought to be able to weaken the interaction between Fe and O* species generated by the O-O bond activation process due to the decrease in the coordination number of Fe. The vulnerability of some Fe-N_4 edge sites to single O* poisoning as will be discussed later might be one reason that causes the catalytic activity loss recently observed in 100-hour durability tests [131].

The study in this section will focus on the three most essential ORR steps: the adsorption of O_2, the 1st PCET process, and the reduction of O*, to understand the influence of graphene edges and metal ligands on the ORR catalytic activity of the Fe-N_4 site. The adsorption of O_2 is discussed in section 4.1.

4.1. O_2 adsorption and direct O-O dissociation over Fe-N_4 graphene edge sites

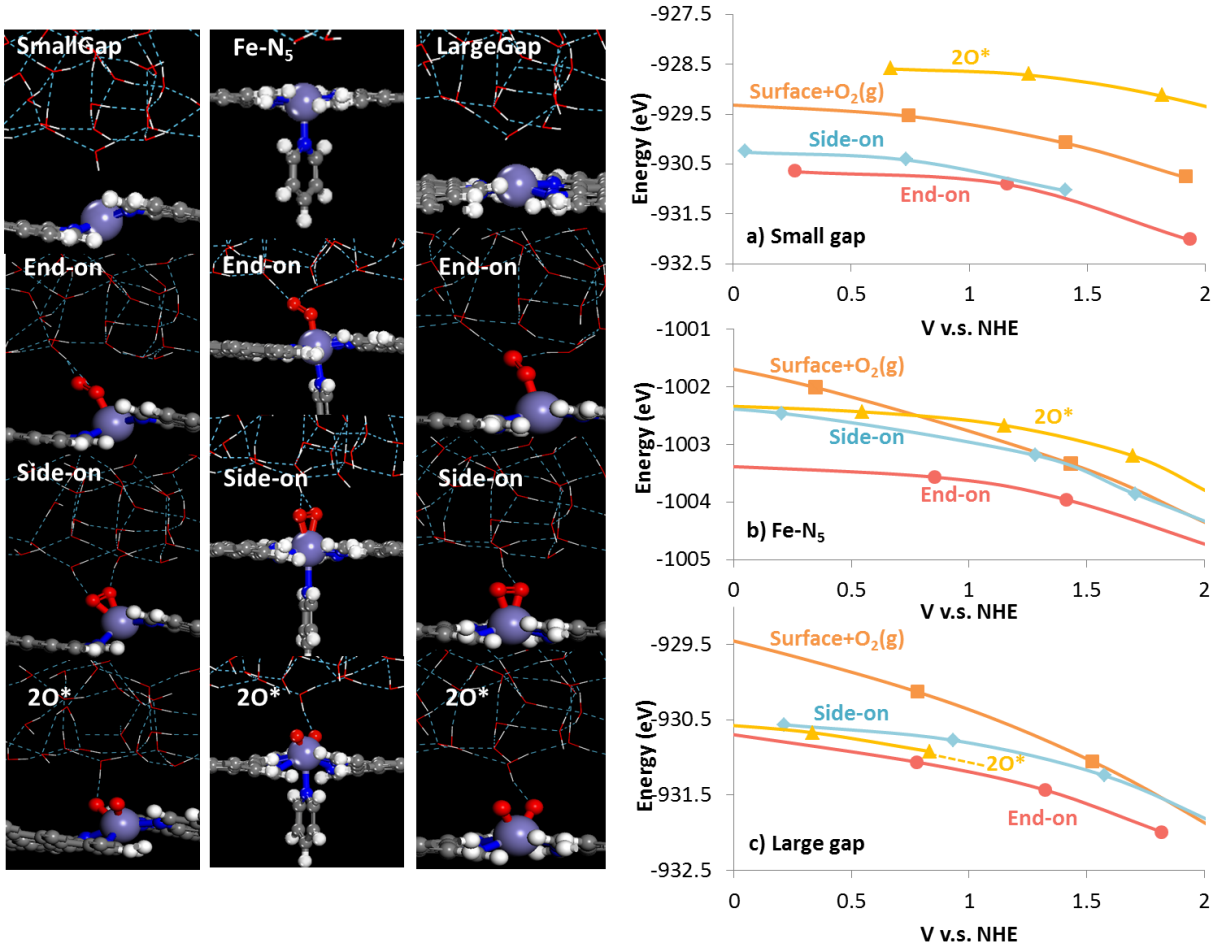

Figure 4.2. O_2 adsorption and dissociation on a) Fe-N_4 small gap b) Fe-N_5 and c) Fe-N_4 large gap sites. The orange curve corresponds to the state of bare surface plus a free O_2 molecule in the gas phase, the red and blue curves correspond to the end-on and side-on adsorption states of O_2 respectively, and the yellow curve corresponds to the product state of direct O-O bond dissociation that forms two strongly bound single O* species.

All three systems favor the end-on adsorption state as shown in Fig. 4.2. The fact that the side-on adsorption state and the subsequent direct O-O bond activation that leads to the 2O* state are less favored for all three systems indicates that the O-O bond is not sufficiently weakened

at this stage. Although direct O-O bond activation is not the most favored process, it is still exothermic on the Fe-N_4 large gap active site, as can be seen in Fig. 4.2c that the energy of the 2O* state lies even below that of the side-on adsorption state. The 2O* state on the Fe-N_5 site (Fe-N_4 with additional ligand as shown in Fig. 4.2b), however, shifts higher in energy than the side-on state and become favored relative to the surface+O_2(g) state only at a potential of 0.7V. The 2O* state becomes totally unfavored relative to the surface+O_2(g) state on the Fe-N_4 small gap active site. The observation suggests an increase in reactivity from Fe-N_4 small gap site to Fe-N_5 site and to Fe-N_4 large gap site for the $4e^-$ oxygen reduction. Also the introduction of the additional ligand in the Fe-N_5 system causes the catalytic activity of the active site to stay between those of the large gap and small gap systems. This trend will be further confirmed by the subsequent study of PCET and O* reduction processes. The 1st PCET process following O_2 adsorption is discussed in section 4.2.

4.2. PCET process leads to OOH* formation and subsequent O-O bond activation

The PCET process that forms OOH* is shown in Fig. 4.3.

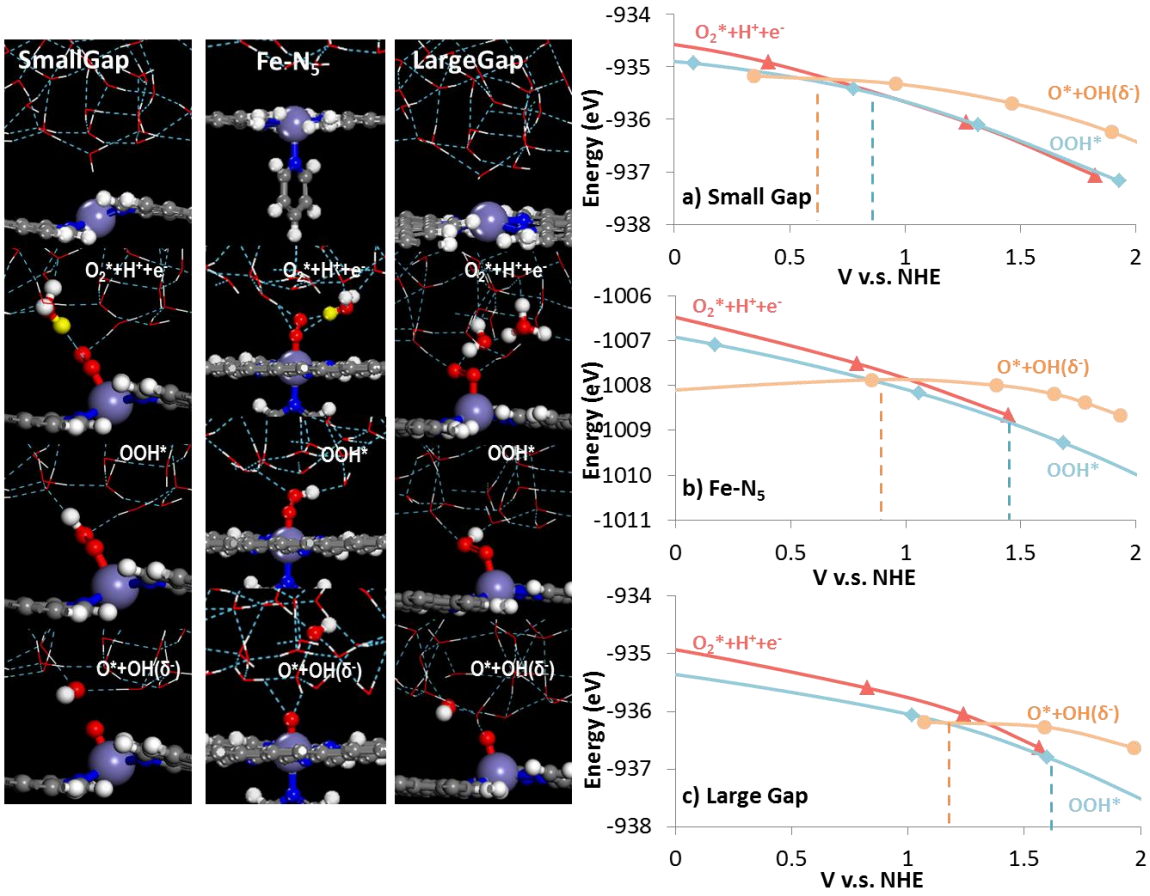

Figure 4.3. Initial reduction of O_2 to a peroxo intermediate on a) Fe-N_4 small gap b) Fe-N_5 and c) Fe-N_4 large gap active sites at the edges of the graphene plane. The red, blue and orange curves represent the O_2*+H^++e^-, OOH* and O*+OH (δ^-) states respectively. The intersection between the red and blue curves indicates the potential (marked by the vertical blue dashed line) at which the O_2+H^++e^-→OOH* process becomes favored and the intersection between the blue and orange curves indicates the potential (marked by the vertical orange dashed line) at which the OOH*→O*+OH (δ^-) process becomes favored.

Fig. 4.3 shows the PCET process following the end-on adsorption of O_2 that forms OOH*. Upon the addition of the proton, an electron is transferred simultaneously from Fe to O_2, weakening the O-O bond. The process should be similar to that on the TM-N_4 graphene basal plane sites as

described by the band decomposition analysis from the previous chapter. It is found that the OOH* dissociates mainly upon interactions with the surrounding water molecules to result in an O*+OH (δ^-) state. The reduction of the adsorbed O_2 to form OOH* and the subsequent dissociation of O_2 occur at higher potentials (>1.5 V for OOH* and 1.1 V for O*+OH (δ^-)) on Fe-N_4 large gap site than on Fe-N_5 site (>1.4V for OOH* formation and 0.7V for O*+OH (δ^-) formation), which is in turn higher than on Fe-N_4 small gap site (0.6V for OOH* formation and 0.5V for O*+OH (δ^-) formation). Again, a similar trend of decreasing catalytic activities towards the PCET process from the Fe-N_4 large gap site to the Fe-N_5 site then to the Fe-N_4 small gap site is observed. The fact that O-O bond activation, a step that is not favored at the adsorption stage, becomes favored after the PCET process is an evidence of the further weakening of the O-O bond upon proton addition. The higher ORR activity of the Fe-N_4 large gap site is accompanied by its stronger interaction with the O* species. As will be discussed in section 4.3, unlike Fe-N_4 small gap and Fe-N_5 sites, the Fe-N_4 large gap site is severely poisoned by the O* species, causing the catalytic turnover on this site to be greatly limited.

4.3. O* reduction

The reduction of O* is another essential step involved in the $4e^-$ ORR process.

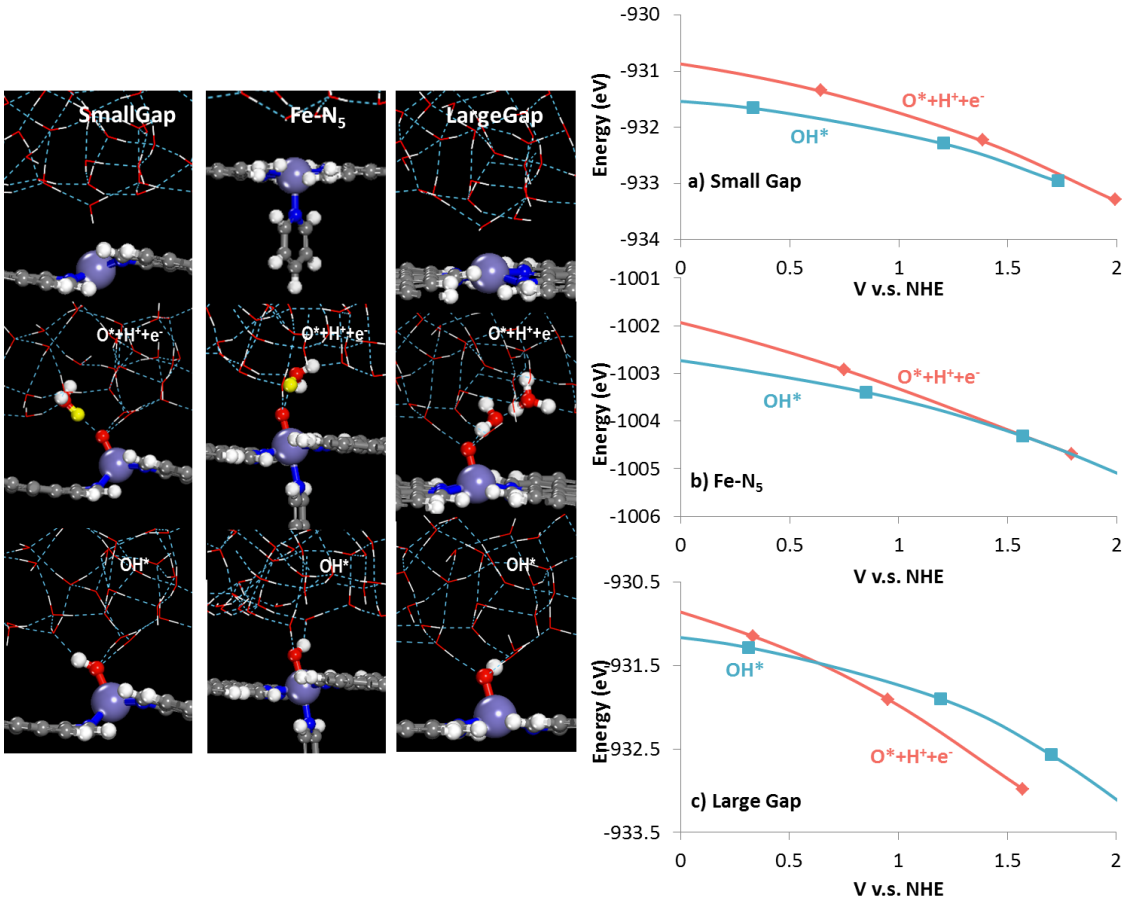

Figure 4.4. Single O* reduction on a) Fe-N_4 small gap b) Fe-N_5 and c) Fe-N_4 large gap sites. The red and blue curves represent the $O^*+H^++e^-$ and OH* states respectively, and the intersection between the two curves corresponds to the potential at which the $O^*+H^++e^- \rightarrow OH^*$ process becomes favored.

The single O* reduction again involves proton shuttling to O* as shown in Fig. 4.4. Active sites that possess higher reduction activity generally suffers from more severe poisoning from single O* species. The Fe-N_4 large gap system is more vulnerable to single O* poisoning as shown in Fig. 4.4c where the single O* species can only be reductively removed at a rather low potential around 0.5V. Again this from one side supports the experimental observation of the activity loss of the Fe-N_4 graphene edge materials during 100-hour durability tests [131], in which case the

most active Fe-N_4 sites might become poisoned, leading to decreased catalytic turnover. This indicates that although the Fe-N_4 large gap site can promote OOH* formation and dissociation at relatively higher potentials, the Fe site might not be available for further reduction cycles until a low potential due to single O* poisoning. The Fe-N_4 small gap and Fe-N_5 sites, however, do not show an apparent vulnerability to single O* poisoning as indicated in Fig. 4.4a and 4.4b that single O* species can be reduced at potentials above 1.5V in both cases. By comparing the three systems, it can be concluded that while Fe-N_4 large gap and Fe-N_4 small gap systems lie at two extremes (one with high initial catalytic activity but low resistance to O* poisoning and the other with low initial catalytic activity but high resistance to O* poisoning), the addition of the pyridine ligand maintains the overall ORR activity between the two ends by partially sacrificing the catalytic activity towards PCET and O-O bond activation in return for better resistance to single O* poisoning. This point can be further elucidated by analyzing the charges and the O-O bond lengths of O_2* and OOH* adsorbates for all three systems.

4.4. A Bader Charge and O-O Bond Length Analysis

To better understand the different reduction behaviors observed on different edge sites discussed in the previous sections, a bader charge analysis on the oxygen atoms for both the O_2* and OOH* adsorbates in all three systems is carried out. A more negative charge on the oxygen atoms indicates a stronger tendency of electron backdonation from the metal to the di-oxygen adsorbates, thereby suggesting a higher degree of O-O bond weakening due to the

occupation of anti-bonding O-O orbitals as discussed in Chapter 3. The bader charges on oxygen atoms for all three systems studied are shown in Table 4.1.

Bader Charge on O-O	**Fe-N_4 Small Gap**	**Fe-N_5**	**Fe-N_4 Large Gap**
O_2*	-0.74	-0.77	-0.82
OOH*	-1.07	-1.14	-1.29

Table 4.1. Calculated Bader charges on oxygen atoms for both O_2* and OOH* adsorbates over Fe-N_4 small gap, Fe-N_5 and Fe-N_4 large gap sites.

Table 4.1 shows that the negative charges on the oxygen atoms accumulate towards higher levels from Fe-N_4 small gap site to Fe-N_5 site then to Fe-N_4 large gap site, suggesting an increasing tendency for the central Fe atom to backdonate its d-band electrons to the O_2 adsorbate, which is in consistency with our previous observations regarding ORR activities of the three systems. The variances in ORR activity should originate from the differences in edge structures and ligands the central Fe atom possesses, since these are the only varying factors among the three systems. It can also be observed from Table 4.1 that for each of the systems, the negative charges on oxygen increase from O_2* to OOH*, indicating an additional and simultaneous transfer of electron from the metal to O_2* once a proton is added to it.

The charge analysis is also consistent with the calculated O-O bond lengths of the adsorbed O_2* and OOH* species. The O-O bond distances for O_2* and OOH* are listed in Table 4.2 for all three systems.

O-O bond distance (Å)	**Fe-N_4 Small Gap**	**Fe-N_5**	**Fe-N_4 Large Gap**
O_2*	1.340	1.359	1.364
OOH*	1.457	1.463	1.475

Table 4.2. O-O bond distances of O_2* and OOH* for Fe-N_4 small gap, Fe-N_5 and Fe-N_5 large gap systems.

The donation of electrons to the anti-bonding orbitals of O_2 usually results in elongation of the O-O bond as previously discussed in Chapter 3. This can be first seen from the increase in the calculated O-O bond lengths for free gas phase molecules from O_2 (1.236 Å) to OOH (1.348 Å) and to HOOH (1.470 Å) as electrons from H are charged into the anti-π-bonding orbitals of O_2. The O-O bond lengths in each column of Table 4.2 also increase from O_2* to OOH* for each of the three systems, and it is notable that upon adsorption, the O_2* state already has a O-O bond length (averagely 1.35 Å as shown in Table 4.2) close to that of the free hydroperoxyl radical OOH (1.348 Å), indicating an electron transfer has already occurred from the central Fe site to O_2. The further increase in O-O bond length from O_2* to OOH* in all three systems shown in Table 4.2 indicates additional electron donation from the metal to the O_2* state accompanied by the addition of the proton to the O_2*, and is therefore a direct proof for the PCET process.

Comparing bond lengths in each row of Table 4.2, an increase in O-O bond length for both O_2* and OOH* adsorbates can be observed from Fe-N_4 small gap to Fe-N_5 and then to Fe-N_4 large gap sites, which is in alignment with the increase in negative charges on O_2* and OOH* shown in Table 4.1. This from another aspect suggests a variation in the amount of electrons donated from the metal center to the O_2* and OOH* species for each system, with the Fe-N_4 small gap system having the lowest degree of electron backdonation and the Fe-N_4 large gap system having the highest.

4.5. Conclusion

In this chapter, three systems containing Fe-N_4 active sites residing between graphene armchair edges with varying edge structures and number of metal ligands are examined for their catalytic activities towards ORR. It is observed that the Fe-N_4 large gap system possesses higher initial catalytic activity but suffers more from singe O* poisoning, while the Fe-N_4 small gap system is less active towards ORR but possesses higher resistance to single O* poisoning. The Fe-N_5 system achieves moderate catalytic activity towards ORR and tolerance to single O* poisoning via the addition of an extra ligand. Further bader charge and O-O bond length calculations reveal that various graphene edge structures and ligands interact with the central Fe atom via the doped N atoms to adjust the electron backdonation capability of the central metal. The negative charges and O-O bond lengths increases from Fe-N_4 small gap to Fe-N_5 then

to Fe-N_4 large gap systems, which well explains the corresponding increasing catalytic activity towards ORR for the three systems studied.

Chapter 5. Oxygen Reduction Reaction Over Metal-free N-doped Graphene Surfaces in Acidic and Basic Media

Much of the recent efforts in catalyst development for proton exchange membrane (PEM) fuel cells have focused on the synthesis of cheap earth-abundant catalytic materials comprised of metal and nitrogen doped carbon substrates that can replace Pt in carrying out the oxygen reduction reaction at the cathode. Some of the earliest efforts to synthesize such materials were focused on Fe and Co porphyrin macrocycles that mimic the active heme sites in cytochrome c that are very efficient in carrying out oxygen reduction in our body [95, 101, 103, 159]. Pioneering work by Gojkovic and Gupta showed that Fe-N_4 and Co-N_4 macrocycles could be pyrolyzed to produce active materials for ORR [160, 161]. Subsequent efforts indicated that even cheaper synthetic routes that simply pyrolyze NH_3, polyacrylonitrile or polyanaline precursors at temperatures of 500-1000^{o}C also result in the development of active and durable ORR catalysts [131, 135, 162]. Most of the initial efforts were carried out over Fe and Co N-doped carbon substrates [131, 132, 159]. A recent debate, however, has emerged in the literature as to whether or not the metal is actually required to catalyze these reactions as the reactions appear to also proceed on carbon sites in contact with the nitrogen in a “metal-free” system [94, 107, 109, 120, 163-169]. There is still a debate of whether trace amounts of metals may be present that are responsible for ORR activity [107, 131, 132, 159, 170]. Herein we examine the oxygen reduction under acidic conditions over model graphene substrates to help

identify the nature of the active sites and the overall reaction paths and provide mechanistic insights.

Recent techniques of synthesizing metal-free N-doped carbon materials mainly involve pyrolyzing carbon substrates in N environment, typically ammonia [120, 166], although variations in the synthesis process may result in different distributions of N-doping sites on the graphene surface which could act as the active sites. The three most commonly observed N centers that may act as active centers are the pyridinic-N, pyrolic-N and graphitic-N (quaternary-N) [171-173]. The rather high instability of pyrolic-N sites during heat treatment as indicated by recent experimental results [174, 175] suggest that it is not present or active for ORR catalysis and that the pyridinic-N and graphitic-N doped sites are much more likely sites for the observed ORR activity. Which of these two sites, however, can carry out catalysis under operating conditions, is still debated [176, 177]. There is some evidence of enhanced rates of ORR with higher content of pyridinic-N sites [171]. This observation, however, was recently challenged by the thoughts that only pyridinic-N sites present at the defect sites or edges on carbon materials are responsible for the measured ORR activities and that their reactivity can be tied to the electronic structures of edges and defects and their influence on O_2 activation [120, 166, 177, 178]. Most of the experimental result suggest that the reaction proceeds via a $4e^-$ process as the $2e^-$ path which proceeds through hydrogen peroxide is rarely seen as there is little to no formation of H_2O_2 [166, 179, 180]. In order to better understand the nature of the

active site as well as the pathways and mechanisms that carry out ORR we examine a series of pyridinic-N and graphitic-N doped sites and their role in carrying out the oxygen reduction.

The detailed N-doping configurations for pyridinic-N and graphitic-N sites are well characterized by STM experiments [174, 176, 181]. Increased levels of N also appear to increase the number of graphitic-N sites with two (or more) N centers that sit at para and meta positions in the aromatic rings embedded into the graphite/graphene layer [181]. The two pyrindic-N and graphitic-N sites with lowest formation energies [181] are shown in Fig. 5.1a and 5.1b. Increasing the N-doping content within the surface appears to lead to an increase in ORR activity [182-184]. In order to probe these higher N-doped sites, we examined the 2N-containing graphitic structure shown in Figure 5.1c. The carbon centers that bind directly to the N sites are believed to be the active sites responsible for ORR activity as they are partially positively charged. As such they are the most likely sites to donate electrons to the O_2 when the catalyst surface is maintained at low potentials and rich in electrons [109, 174, 185].

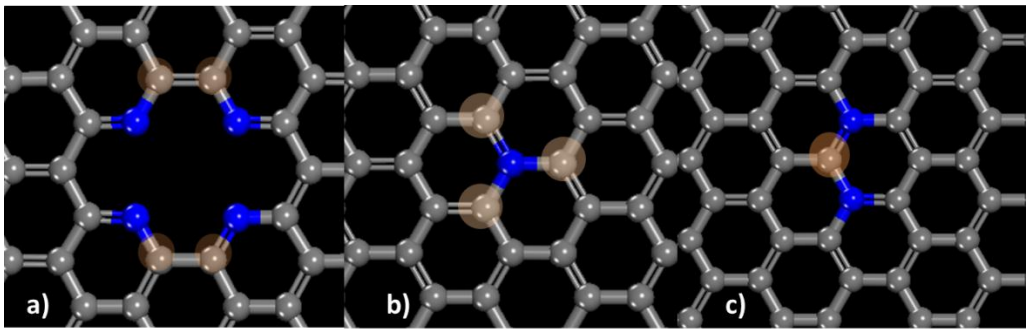

Figure 5.1. Proposed N-doped graphene systems: a) pyridinic-N_4 system, b) graphitic-N_1 system and c) graphitic-N_2 system. The carbon sites that are most active towards ORR in each system are highlighted.

While ORR over Pt and Pt alloys is predominantly carried out at acidic condition [94, 95, 120], it is most often carried out in alkaline conditions over the N-doped systems due to the greater durability and improved catalytic performance [186-189]. Herein we examine the pathways and potential dependent energies to carry out ORR at the different pyridinic and graphitic N sites highlighted in Fig. 5.1 in both acidic as well as basic media.

The general paths involved in the reduction of oxygen over metals in acidic and basic media are fairly well established in the literature [90, 187]. In general, the $2e^-$ reduction of oxygen leads to the formation of $HOOH/OOH^-$ in acidic/basic conditions whereas the $4e^-$ paths leads to the formation of H_2O/OH^- under acidic/basic conditions as illustrated by Fig. 5.2a and Fig. 5.2b.

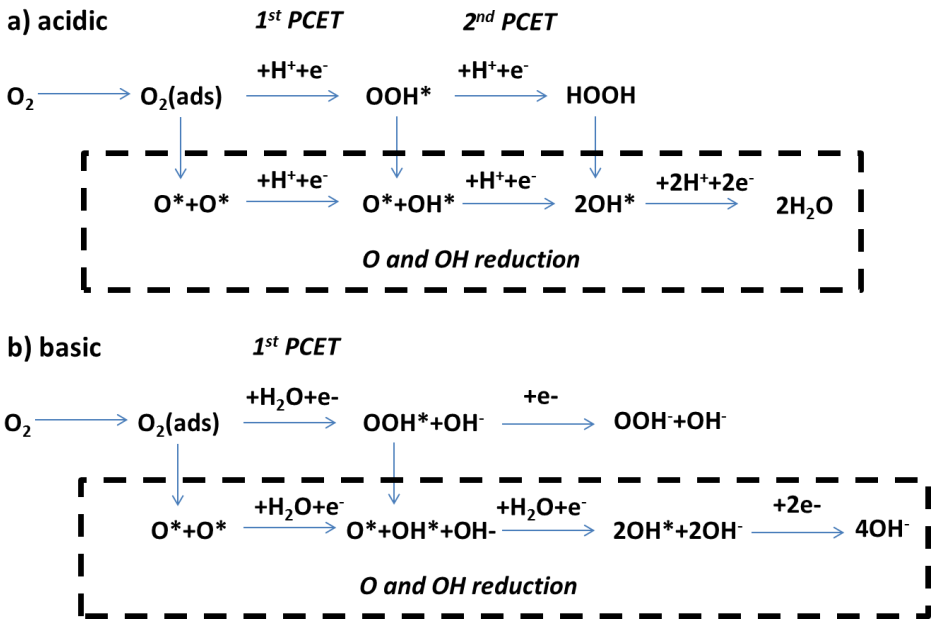

Figure 5.2. Overall reaction paths proposed for the oxygen reduction reaction when carried out in a) acidic and b) basic media. The steps involve the complete $4e^-$ reduction of O_2 to water (in acid) an OH^- (in base). The total number of electrons transferred during the reduction process can be determined by summing up all electrons transferred along a specific path from left to right.

While the general pathways involved in ORR appear to be well established, the mechanisms and elementary steps are still greatly debated in the literature. The reduction of oxygen in an acidic environment is thought to proceed by the adsorption and activation of O_2 followed by a series of proton-coupled electron transfer steps that proceed via protons present in solution. In basic conditions, the O_2 is adsorbed and activated but now PCET reactions proceed via water molecules and OH^- is generated as a result. The molecular adsorption and activation of O_2, the 1^{st} PCET process and the reduction of the resulting O* intermediate appear to be the most important steps in the ORR process and as such are discussed in detail for all three proposed N-doped graphene systems under both acidic and basic conditions.

5.1. ORR under acidic conditions

5.1.1. ORR on pyridinic-N active site under acidic conditions

The adsorption of oxygen in all of the examples examined herein appears to proceed at the sp^2 carbon sites that bind to N within the graphene basal plane as these are positively charged centers that can accept electrons. This is consistent with previous theoretical and experimental work reported in the literature [109, 174, 185]. The adsorption of O_2 to sp^2 C centers at the pyridinic-N_4 active site is shown in Fig. 5.3.

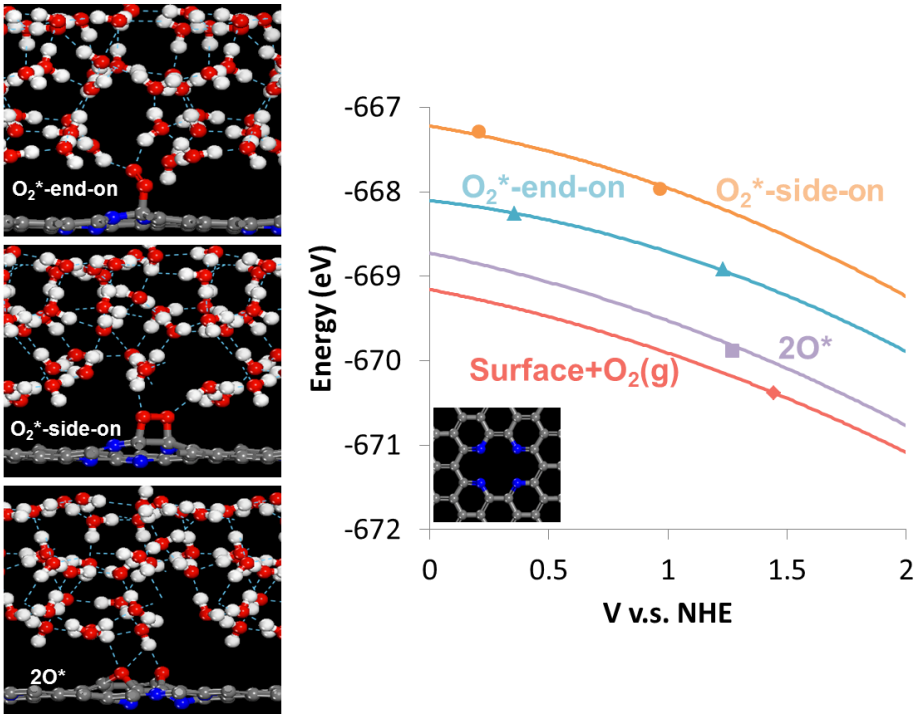

Figure 5.3. The adsorption of O_2 at the pyridinic-N_4 site under acidic conditions.

O_2 can adsorb in an end-on configuration as a superoxo intermediate where there is a single electron transfer from the graphene to bound O_2 or in a side-on configuration as a peroxo intermediate involving a $2e^-$ transfer from the graphene into the antibonding $2\pi^*$ state of the bound O_2. The potential dependent energies for the O_2*-end-on (superoxo), O_2*-side-on (peroxo) and the dissociated 2O* states are shown together with the initial free O_2 in the gas phase state (surface+O_2(g)) in the four curves shown in Fig. 5.3. All three of the product states lie above that for the initial surface+O_2(g) state (the red curve in Fig. 5.3) in energy, suggesting neither the superoxo or peroxo adsorption states nor the dissociated oxygen state are favored at any point over the entire potential range of interest on the active carbon sites in acidic media. While the dissociated oxygen state, 2O*, is not favored relative to the surface+O_2 (g) state, it is lower in energy than either the end-on or the side-on adsorption states. This is characteristically different from our previous results reported on the dissociative adsorption of O_2 on TM-N_4 systems which show that the 2O* state is never the favored state. Further examination of the 2O* state shows that the O* species that form are incorporated into the graphene surface via insertion into nearby C-C bonds (as shown by the bottom left 2O* states in Fig. 5.3). As will be discussed later, the single O* species generated on the graphitic-N carbon sites does not adopt this orientation but instead preferentially sits atop of the C site and is closer to a C-O single bond than the C-O bond here. No further reduction paths under acidic conditions were examined on the pyridinic-N_4 surface as it is believed that further reduction of oxygen (especially the PCET process) predominantly proceeds through an outer sphere

mechanism in which the adsorption of O_2 or the electron transfer from the carbon to the bound O_2 is rate limiting [163, 190, 191].

5.1.2. ORR on graphitic-N active sites under acidic conditions

The same oxygen adsorption process is examined on the graphitic-N_1 and graphitic-N_2 surfaces. The potential energy curves are shown in Fig. 5.4.

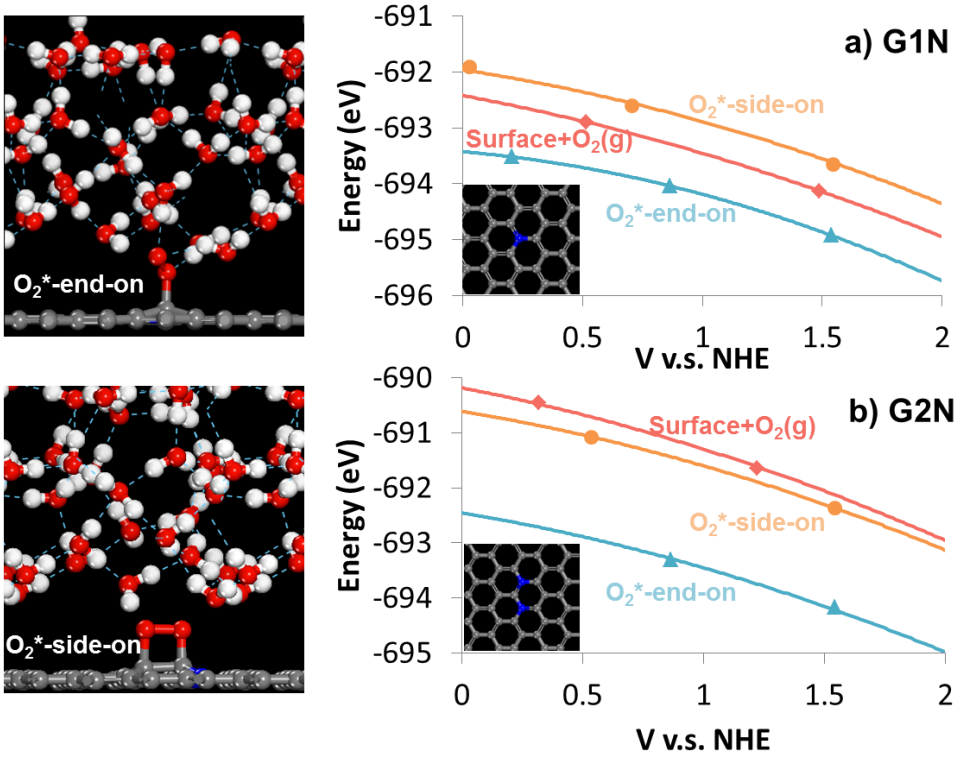

Figure 5.4. The adsorption of O_2 on the a) graphitic-N_1 (G1N) and b) graphitic-N_2 (G2N) active sites under acidic conditions.

In contrast to the pyridinic-N_4 active site, the end-on adsorption of oxygen to form the superoxo (O_2^-) intermediate on the graphitic-N_1 active site is favored over the entire potential range. The side-on adsorption to form the peroxo (O_2^{2-}) intermediate as indicated by the O_2*-side-on curve in Fig. 5.4a, however, is still higher in energy than the free surface and gas phase oxygen state (surface + O_2(g)).

Recent experimental evidence suggests that increasing N-doping content can increase the ORR activity of the carbon sites [182-184]. As such, one could conclude that increasing the number of neighboring N-sites within nitrogen-doped graphitic system should increase the activity of the neighboring carbon sites. It is found in Fig. 5.4b that on the graphitic-N_2 site, the end-on adsorption of O_2 as a superoxo (O_2^-) intermediate is again the most favored state. The more active C centers at the graphite-N_2 sites also allow for the side-on adsorption of O_2 (peroxide O_2^{2-}) to become favorable relative to the surface+O_2(g) state over the full range of potentials examined. Both the side-on and end-on adsorption states decrease in energy relative to the surface+O_2(g) state as the N content increases from graphitic-N_1 to graphitic-N_2, suggesting a general increase in oxygen reduction activity from the graphitic-N_1 site to the graphitic-N_2 site. In both systems, the active carbon sites are pulled out from the graphene plane by the adsorbed oxygen as a result of change in the electronic structure on the carbon site from sp^2 to sp^3 hybridization. The C-O bond length in the graphitic-N_1 system is 1.50 Å, as compared to the C-O bond length of an average single C-O bond (1.43 Å). The C-O bond length in the graphitic-N_2

system was calculated to decrease from that in the graphitic-N_1 system to 1.44 Å. This suggests an increase in the interaction between the active carbon site and the adsorbed oxygen.

Unlike the adsorption of oxygen on the pyridinic-N sites, O_2 adsorbed on graphitic-N_1 and graphitic-N_2 sites does not want to dissociate to form 2O* as the superoxo as well as the peroxo forms are energetically much more favorable than the 2O* state at the C-N sites over the range of potentials examined from 0 – 2 V. The 2O* state is never favored as the direct activation of the O-O bond is energetically very difficult. Both the graphitic-N_1 and N_2 sites favor the adsorption of O_2 as a superoxo intermediate which subsequently reacts in a PCET process to form OOH* as shown in Fig. 5.5.

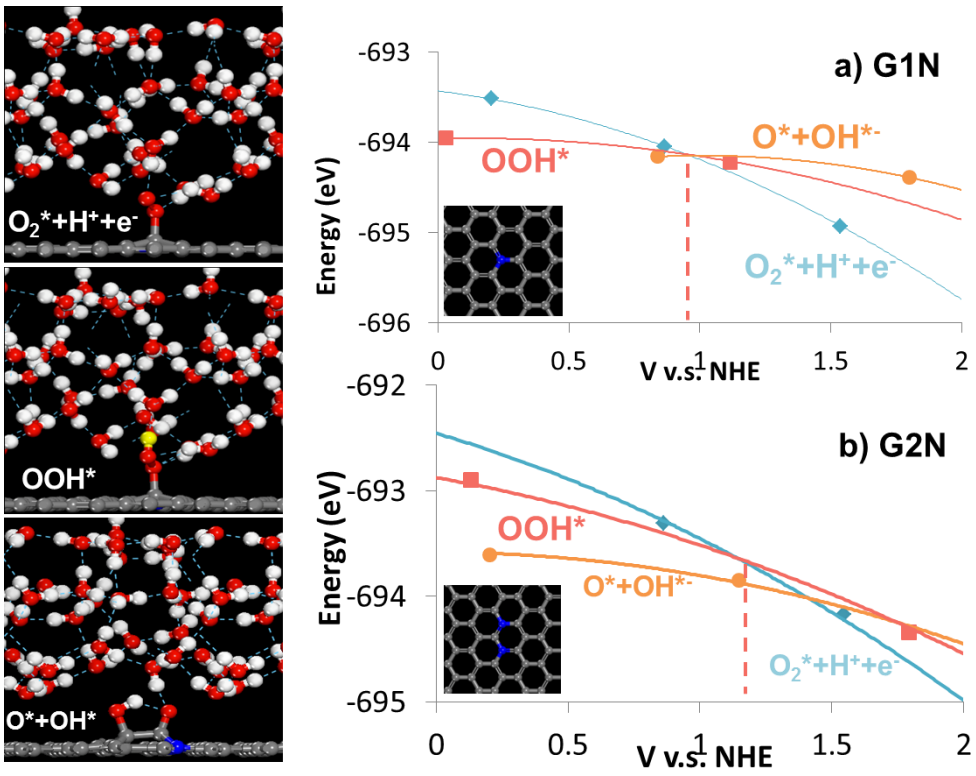

Figure 5.5. OOH* formation and subsequent O-O bond activation over a) graphitic-N_1 (G1N) and b) graphitic-N_2 (G2N) sites under acidic conditions.

The OOH* product appears to intersect the O_2*+H^++e^- reactant state at a potential near 0.9 V vs. NHE at the graphitic-N_1 site. The subsequent activation of the O-O bond of OOH* to form the O* and OH* products also occurs at about 0.9 V vs. NHE as can be seen at the triple point intersection shown in Fig. 5.5a. The activation of the OOH* to form O*+OH* was found to require the initial active carbon center to which the OOH* is bound as well as a second carbon center that is further away from the N dopant site as is shown in Fig. 5.1b. This is unlike other ORR catalytic systems such as organometallic systems where only a single active metal site in

the TM-N_4 participates through the whole ORR process. We will show later that, however, the subsequent reduction of O* sets the lowest operating potential for ORR at the graphitic-N_1 site.

Both the first and second PCET steps that result in the formation of OOH* and its subsequent dissociation to O*+OH*, respectively, proceed at higher potentials on the graphitic-N_2 active site as shown in Fig. 5.5b. The formation of OOH* occurs at 1.2 V which is 0.3V higher than that at the graphitic-N_1 active site. The higher reduction potential would suggest lower overpotential and higher catalytic activity of the graphitic-N_2 system towards ORR. The second PCET step results in the rupture of the O-O bond and the formation of O*+OH* state which lies below both the O_2* and the OOH* curves in Fig. 5.5b, indicating that this state is much more favorable from 0 – 1.2 V and proceeds immediately following the formation of the OOH* intermediate. The observation is consistent with the expectation that the graphitic-N_2 site possesses a higher ORR activity than the graphitic-N_1 site due to higher N content [182-184].

The final steps in the ORR process involve the subsequent reduction of O* and OH* to form water which also occur via PCET processes. The O* and OH* products that form, however, will bind to the active C sites much more strongly than O_2* and OOH* and may act to block or poison the active sites. The results for reduction of O* to OH* are shown in Fig. 5.6.

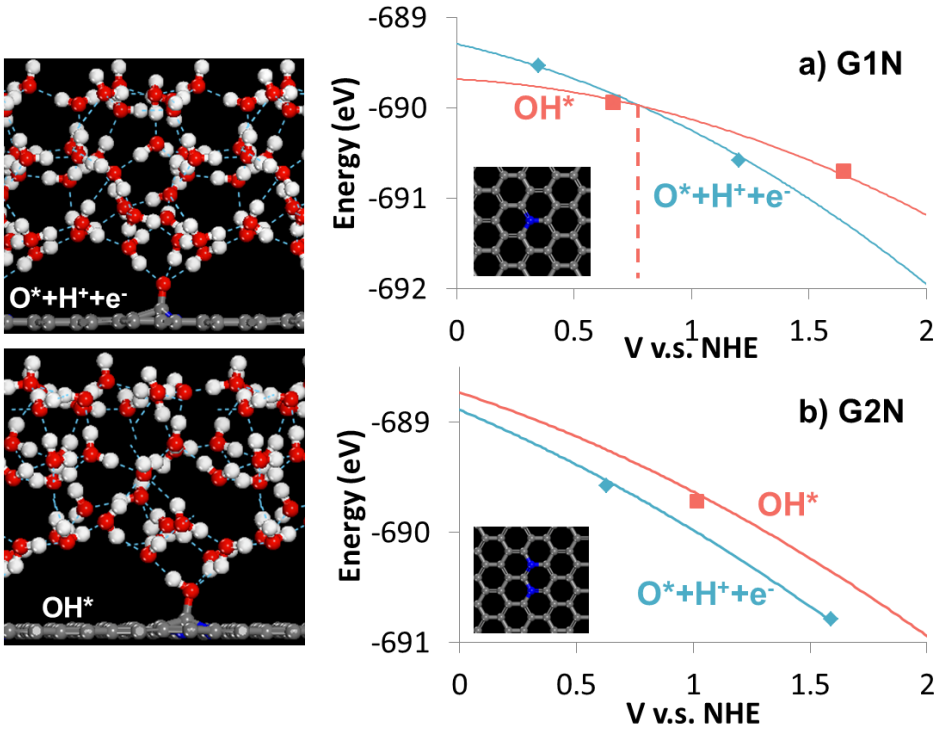

Figure 5.6. Reductive removal of single O* species at the a) graphitic-N_1 (G1N) and b) graphitic-N_2 (G2N) sites under acidic conditions.

The strong interaction between O* and the carbon site lifts the carbon out of the plane of the graphene in both the graphitic-N_1 and graphitic-N_2 systems. The C-O bond length for the graphitic-N_1 system is 1.37 Å which is close to that of a single C-O bond. The C-O bond length for the adsorbed O* species at the graphitic-N_2 carbon is somewhat shorter at 1.32 Å. The shorter C-O bond length in the graphitic-N_2 system over that in the graphitic-N_1 system is the result of the stronger C-O interaction in graphitic-N_2. This strong interaction between O* and the carbon atom in the graphitic-N_2 site makes it difficult to remove the O* from this site. This results in poisoning of the C center. The results shown in Fig. 5.6a reveal that O* at the graphitic-N_2 site is strongly bound to the carbon and sits well below the reduction curve to form

OH*. As such O* cannot be reduced or removed at potentials of interest. This indicates that while the graphitic-N_2 system may demonstrate higher initial ORR activity, the active sites are severely poisoned by O*.

The results for the graphitic-N_1 site, on the other hand, indicate that O* is reduced to form OH* at potentials slightly lower than the potential of 0.7 V. Both the adsorption of oxygen and O_2* PCET are promoted at the graphitic-N_1 site thus indicating that the reduction of single O* species is the limiting step on graphitic-N_1 active site under acidic conditions. This is consistent with recent experimental observation showing that synthesized N-doped carbon nanosheets can effectively promote the $4e^-$ reduction of oxygen with an initial onset potential of 0.66 V vs. NHE (0.72V vs. RHE) and a high stable current density achieved further at 0.44 V vs. NHE (0.50V vs. RHE) [192].

As will be explained later by a charge analysis, the general trend of the increase in ORR activity under acidic conditions from pyridinic-N_4 to graphitic-N_1 then to graphitic-N_2 system is consistent with the increase in charges on the active carbon sites. The same ORR process is studied further under basic conditions and discussed in the following sections. A similar trend is also observed under basic conditions for the three N-doping systems.

5.2. ORR under basic conditions

Many of the current experimental studies on metal-free N-doped carbons have been carried out in alkaline media to avoid the corrosion issues. The alkaline fuel cells (AFC) were extensively examined well before the emergence of PEMFCs, and can theoretically outperform PEMFCs and support more facile ORR kinetics. Recent developments in anion exchange membranes have mitigated issues associated with the progressive carbonation of the alkaline electrolyte by CO_2 and have thus led to a resurgent study of AFCs in recent years [1, 193, 194]. The base catalyzed ORR paths use water as the source of protons and are somewhat different than those carried out in acid as was discussed previously and shown in Fig. 5.2a. We examine here the ORR paths in the presence of base on the pyridinic as well as the graphitic nitrogen containing systems presented in Fig. 5.1.

At higher values of pH, the potential (vs. NHE) at which each ORR step occurs generally decreases as compared to the same steps carried out at lower pH. The decrease in the reduction potential that occurs at the cathode is accompanied by the decrease in the potentials for oxidation processes at the anode. As a result, the reversible hydrogen electrode (RHE) is more often used for electrochemical measurements in basic environment. The NHE and RHE can convert between each other according to the relation RHE = NHE – 0.0591*pH, which indicates that the cathode reduction potential as measured with respect to NHE would be approximately 0.8V less than that measured using RHE under a pH of 14. So instead of focusing

on a 0 to 2 V vs. NHE potential range, the study of ORR under basic conditions here aims to analyze potentials from -1.5 to 0.5 V vs. NHE. We will show in section 5.2.1 to 5.2.2 that there is a similar trend of increasing ORR catalytic activity in alkaline media in moving from the pyridinic-N_4 to graphitic-N_1 and to graphitic-N_2 systems as we saw for the acidic conditions.

5.2.1. ORR on pyridinc-N_4 active site under basic conditions

In the pyridinic-N_4 system, ORR reaction initially proceeds by the initial adsorption and activation of oxygen via electron transfer from the active carbon site to the antibonding π^* state of the adsorbed O_2. Under basic conditions the steps are similar to those reported in acidic conditions. O_2 can bind either as end-on as a superoxo or side-on as a peroxo intermediate. The changes in energies for these states as well as for the initial state of O_2(g) and the dissociated 2O* product state at the pyridinic-N_4 site are shown as a function of potential in Fig. 5.7.

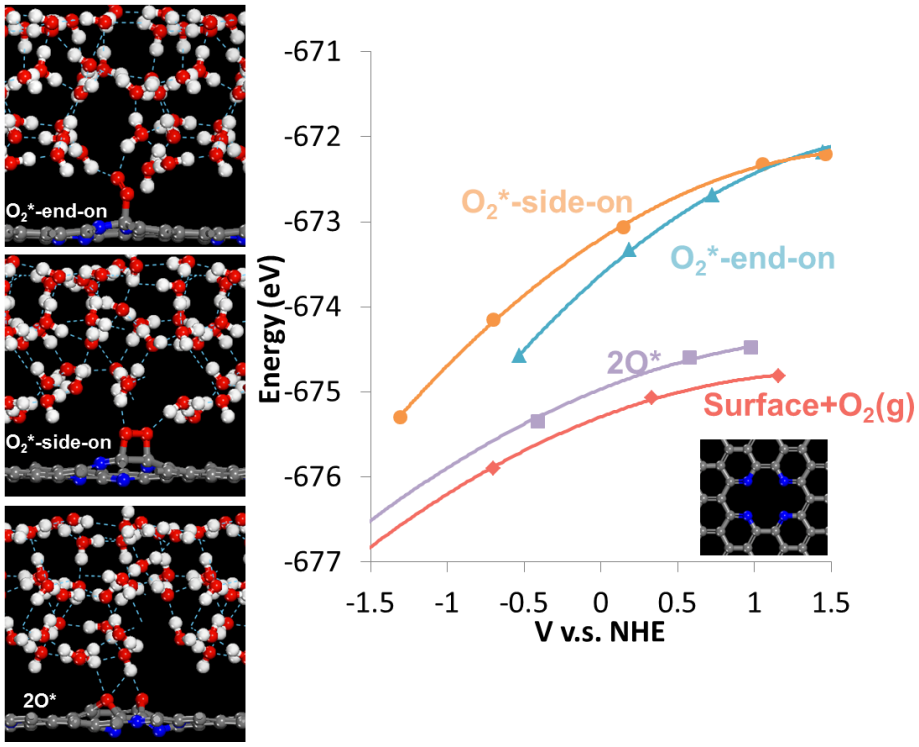

Figure 5.7. O_2 adsorption over pyridinic-N_4 site under basic conditions.

Neither of the O_2 adsorption states are favored at the pyridinic-N_4 site under basic conditions as they are significantly higher in energy than the O_2 (g) + surface reactant state over the entire range of potentials examined as is shown in Figure 5.7. This is similar to the results that were reported earlier in Fig. 5.3 for the adsorption of O_2 at the pyridinic-N_4 sites in acidic media. While the dissociative 2O* state is energetically more favorable than either of the O_2* adsorption states, it is still about 0.3 eV higher in energy than the O_2 (g) + surface state over the range of potentials of interest. The higher energy to form the 2O* product is predominantly due to the energetic penalties that are incurred in breaking C-C bonds in the graphene surface as the single O* products prefer to incorporate into the graphene sheet. These single O* species are also much more difficult to remove via reduction as was also found in acidic

conditions. There does not appear to be a viable route to adsorb or activate O_2 on the pyridinic-N_4 sites and thus ORR at these sites appears unlikely. This is further supported by a detailed analysis of the charge at the carbon sites that is presented later in section 5.3. The results here support experimental suggestions that the pyridinic-N_4 sites in the basal plane are not responsible for ORR in alkaline media [177]. The results do not rule out the reactivity of pyridinic-N_4 sites at graphene edges or defect sites.

5.2.2. ORR on graphitic-N active sites under basic conditions

We examined the elementary O_2 adsorption and activation, O_2 reduction, OOH* activation and reduction of the resulting single O* products at the graphitic-N_1 and graphitic-N_2 sites under basic conditions. The overall energies for O_2 adsorbed in the end-on and side-on configurations to form the superoxo and peroxo O_2* intermediates, respectively, are reported along with the energies for the initial O_2(g) + surface state as a function of cathode potential in Fig. 5.8.

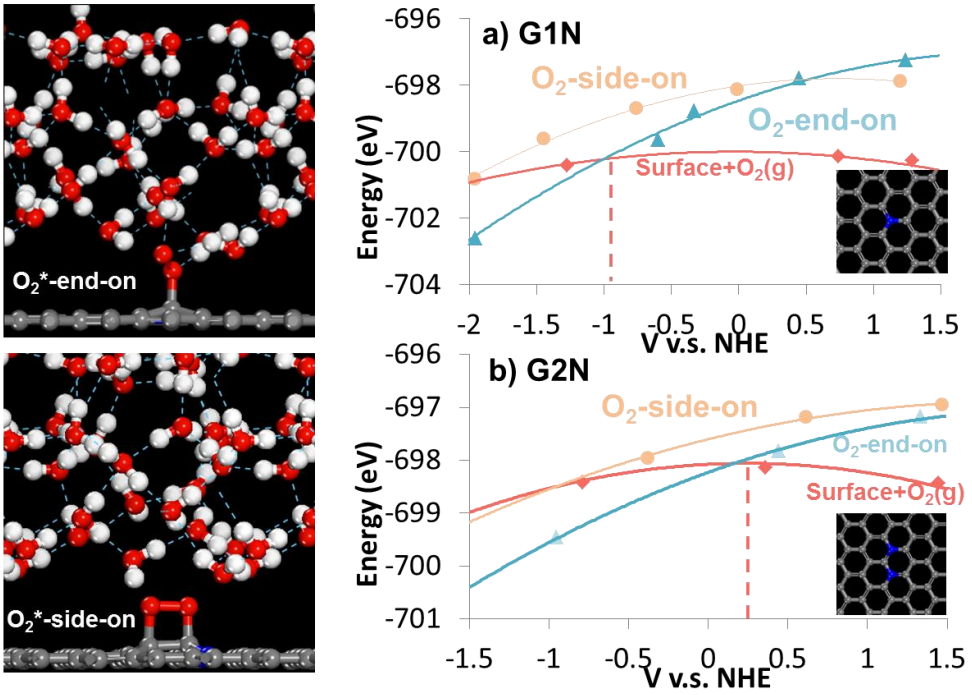

Figure 5.8. O_2 adsorption on a) graphitic-N_1 (G1N) and b) graphitic-N_2 (G2N) active sites under basic conditions.

The adsorption of O_2 in the end-on configuration is favored over the side-on configuration on both graphitic-N sites under basic conditions over all potentials examined which is consistent with the results for O_2 adsorption on graphitic-N in acidic conditions. The end-on adsorption of O_2 on the graphitic-N_1 active site, however, only becomes favored at potentials less than -1 V. This suggests that, unlike acidic conditions, the graphitic-N_1 site is inactive in alkaline media. An increase in catalytic activity towards ORR is again expected under basic conditions when the N doping content increases from the graphitic-N_1 system to the graphitic-N_2 system. The end-on adsorption of O_2 initiates at a much higher potential of 0.2 V on the graphitic-N_2 site as indicated by Fig. 5.8b. The C-O distance in the end-on configuration is 1.53 Å for the graphitic-

N_1 system and 1.42 Å for the graphitic-N_2 system. The decrease in the C-O distance is a reflection of a stronger interaction between O_2 and the carbon site in the graphitic-N_2 system. Similar to results under acidic conditions, the direct activation of the adsorbed O-O does not occur at any potential on the graphitic-N_1 or graphitic-N_2 active sites within the interested potential range.

The fact that O_2 adsorption is favored only at a relatively low potential and that O-O activation does not occur on the graphitic-N_1 site suggest that these sites may not be active. Subsequent calculations for the formation of OOH* confirms this hypothesis.

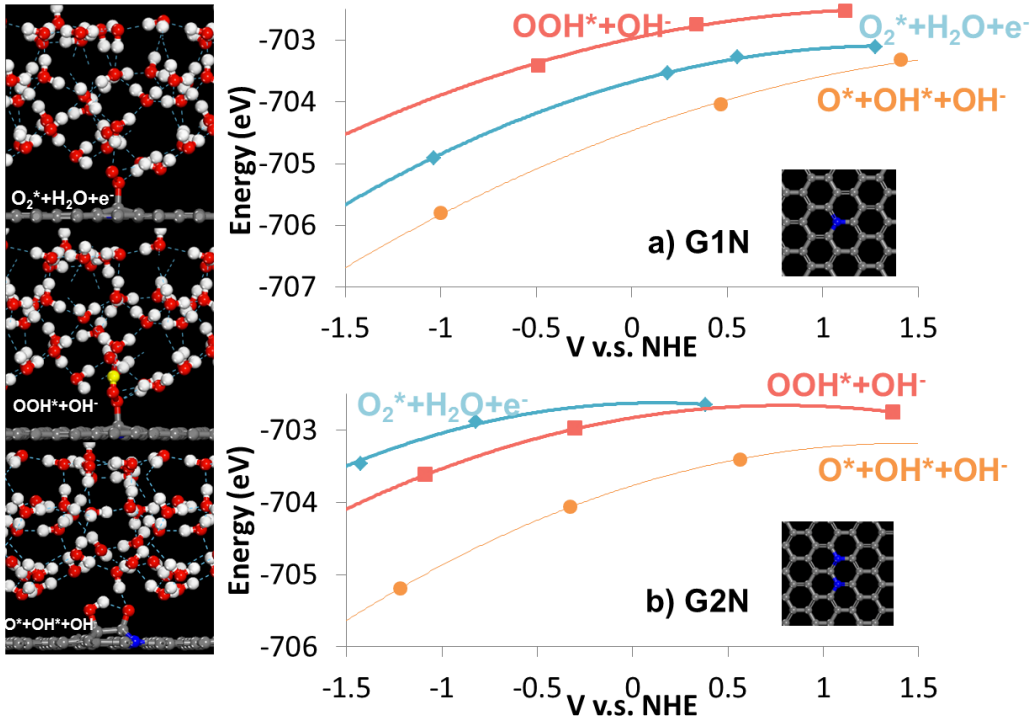

Figure 5.9. OOH* formation and subsequent O-O bond activation on a) graphitic-N_1 (G1N) and b) graphitic-N_2 (G2N) sites under basic conditions.

The results for O_2* vs. OOH* presented in Fig. 5.9a confirms that the formation of OOH* is not favored at the graphitic-N_1 site at any potential over the range of potential examined. This is possibly due to the weak interaction between the carbon site and the oxygen molecule. While the O*+OH*+OH^- state is energetically very favorable, we cannot activate O_2 directly or via PCET to reach this state. As opposed to our previous observation that the graphitic-N_1 system is the most active system towards ORR under acidic conditions, the results under basic conditions here indicate that the graphitic-N_1 site is not catalytic active.

The results for the adsorption and activation of O_2 at the graphitic-N_2 site were found to be quite different than those on the graphitic-N_1 site. O_2 readily adsorbs as a peroxo species in an end-on configuration at the graphitic-N_2 site at potentials up to 0.2 V as was discussed and readily undergoes PCET to form OOH* at potentials as high as 0.5V (Fig. 5.9b). The subsequent activation of the O-OH bond for OOH* can occur over the entire potential range of interest. The observation that the graphitic-N_2 system is able to promote OOH* formation and O-OH bond activation is consistent with the fact that the carbon site in the graphitic-N_2 system is more active than in the graphitic-N_1 system.

The weak interaction between that was found for the graphitic-N_1 site and O_2 would suggest that if you could activate O_2, O* reduction would readily occur due to weaker interactions between oxygen and the active carbon site. The results for the reduction of O* on the graphitic-N_1 site under basic conditions were examined and compared with the results for O* reduction from the graphitic-N_2 site in Fig. 5.10.

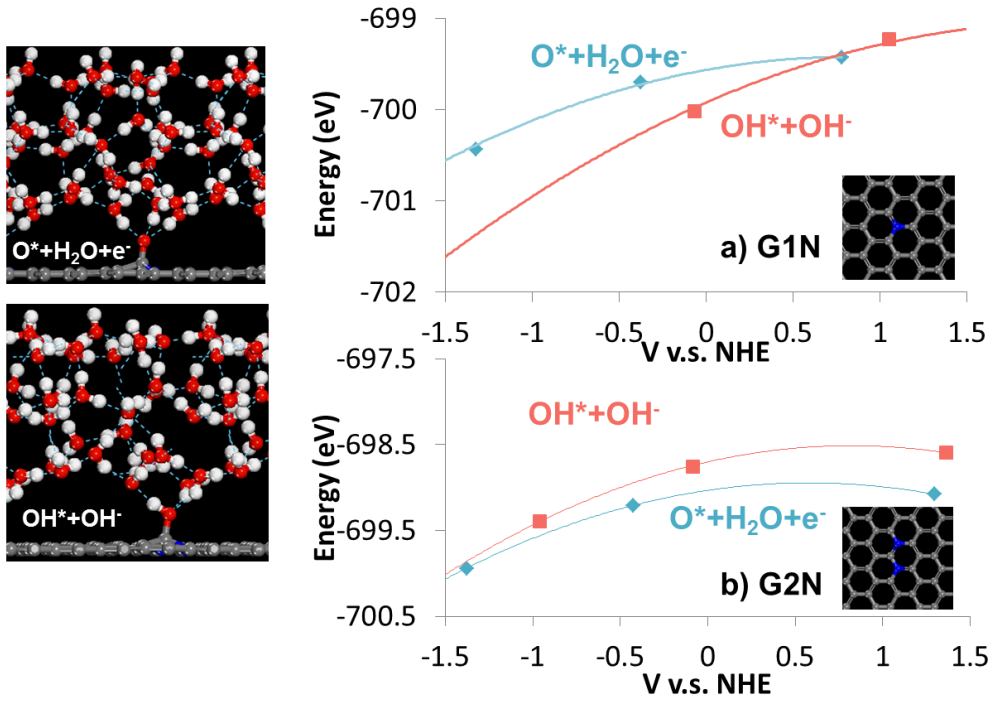

Figure 5.10. Reductive removal via PCET of O* at: a) graphitic-N_1 (G1N) and b) graphitic-N_2 (G2N) sites under basic conditions.

The reduction of O* at the graphitic-N_1 site as shown in Fig. 5.10a is favored at a rather high potential of 0.8V under basic conditions, suggesting that if O* forms it can be readily removed from the carbon site. The binding of O* to the graphitic-N_2 site, however, is too strong and as such the reduction of O* does not occur at any of the potentials of interest as can be seen in Fig. 5.10b where the O*+H_2O+e^- state is lower in energy than the OH*+OH^- state over the entire potential range. This site appears to be poisoned by the strongly held O*.

The C-O distance for adsorbed single O* species under basic conditions is 1.36 Å for the graphitic-N_1 site and 1.31 Å for the graphitic-N_2 site. The decrease in C-O distance from graphitic-N_1 system to graphitic-N_2 system is indicative of an increasing interaction between carbon and O*, which is consistent with the observed differences in O* reduction activities between the two sites. The results here suggest that the graphitic-N_1 site cannot easily adsorb or activate O_2* under basic conditions, and the active carbon site in the graphitic-N_2 system is severely poisoned by O* and is therefore also unavailable for further ORR cycles.

None of the three N-doping systems examined here appears to be catalytic active towards ORR under basic conditions. They are found to either possess no initial ORR activity at all, or suffer from severe O* poisoning such that catalysis would be shutdown. A possible extension to this part of study might be on other possible N-doping configurations or contents that can lead to moderate active carbon sites whose ORR activity lies between that of graphitic-N_1 and graphitic-N_2 sites.

5.3. Charge analysis

To better understand how different N doping configurations and N doping contents contribute to differences in the ORR reactivity, a charge analysis on the local C and N sites was performed. The charges on the doped N atoms and the surrounding carbon atoms that are either direct or indirect neighbors to the N atoms are shown in Fig. 5.11.

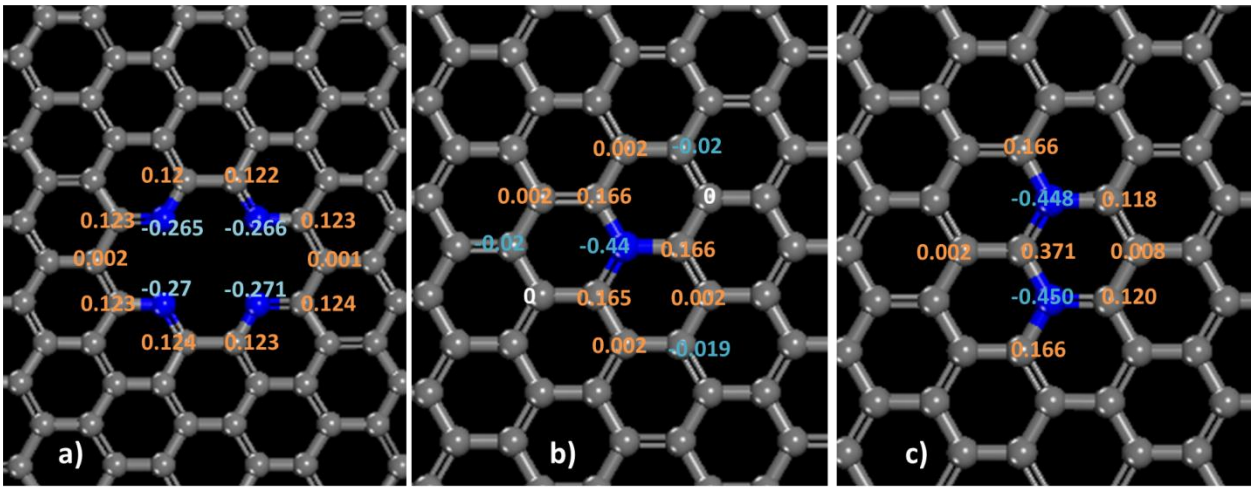

Figure 5.11. Charge analysis of nitrogen and carbon sites that are likely involved in the ORR process for a) pyridinic-N_4 b) graphitic-N_1 and c) graphitic-N_2 systems.

The results show that the carbon atoms that directly bind to the nitrogen centers are the most positively charged sites and likely the most active carbon centers. The positive charge on these sites increases from the pyridinic-N_4 system (+0.12 e average), to the graphitic-N_1 system (+0.17 e average) and then to the graphitic-N_2 system (+0.371 e average). The increase in the positive charge results from the coordination and positioning of the nitrogen. In the pyridinic site N binds to only two neighboring carbon centers and only abstracts so much charge from these sites. The graphitic-N_1 nitrogen sites bind to three carbons and as such the charge on the N increases from ~-0.266 e to ~-0.44 e and more efficiently removes charge from the C centers. The central carbon in the graphitic-N_2 site results in bonds to two different nitrogens and as such loses charge to both resulting in essentially a doubling of its positive charge from ~+0.166 e (for graphitic-N_1) to ~0.371 e (for graphitic-N_2).

The increase in the positive charge on the active carbon site would suggest that these sites could withstand a higher positive charge and facilitate electron transfer from the surface electrode in carrying out the PCET reactions. The higher positive charge would also increase its bonding to the O_2, OOH*, O* and OH* intermediates. This would stabilize reactions which involve bond breaking transition states (O-O and O-OH activation) and destabilize those involving the weakening or breaking of the C-O bond (O* and OH* reduction).

The two graphitic-N doping configurations result in more positively charged carbon atoms than the pyridinic-N doping configuration, and are therefore more catalytic active towards ORR. A comparison between the two graphitic-N doping configurations indicates that an increase in N-doping content leads to a further decrease in the barriers for the activation of O-OH but an increase in the barriers for the O* and OH* reduction.

It has been reported recently that the spin density on the carbon active site resulting from N doping on CNTs and carbon nano-ribbons (CNRs) might also play an important role due to the belief that the spin density indicates the amount of unpaired electrons a certain carbon site possesses [185]. Our calculations, however, suggest that the carbon sites on graphitic-N doped graphene basal planes that possess the highest spin density are not catalytically active towards ORR. The carbon atoms in the pyridinic-N system generally possess zero spin density. The different electronic structures between CNTs or edge-rich CNRs and graphene basal planes might be a possible cause for this discrepancy. The results herein indicate that the spin density

on the carbon sites is less important than the charge distribution in the ORR process for N-doped carbon sites on graphene basal planes.

5.4. Conclusion

To better understand the ORR process on metal-free N-doped carbon materials, three representative N-doped systems including pyridinic-N_4, graphitic-N_1 and graphitic-N_2, were used to examine the reaction energetics for the three most essential ORR steps under both acidic and basic conditions. A charge analysis of the N-doped graphene surface for different N-doping configurations indicates that the carbon sites that are directly adjacent to the doped N atoms are positively charged due to the electron extraction by the neighboring N sites. These positively carbon sites are more active towards ORR compared to other less positively charged carbons on the graphene basal plane. By comparing the three systems, we find that the carbon sites near the pyridinic-N atoms are not catalytic active for ORR under either acidic or basic conditions. Further study of the graphitic-N_1 and graphitic-N_2 systems indicates a positive relationship between ORR activity and N-doping content under both acidic and basic conditions. However, the higher activity of the graphitic-N_2 system in promoting the PCET process and the subsequent O-O bond activation is accompanied by more severe O* poisoning that forms stable carbonyl surface groups. It is therefore possible that the experimentally observed ORR activity might be a collective behavior of various N-doping configurations with ORR activities ranging between that of the graphitic-N_1 and graphitic-N_2 systems.

Chapter 6. Complete ethanol oxidation at a Pt-Mo alloy anode

The use of ethanol as a fuel for PEM fuel cells would help to solve the issues of hydrogen generation, storage and portability that have prevented the adoption of hydrogen fuel cells as we discussed in Chapter 1. The oxidation of ethanol however is limited by our ability to activate the C-C bond and to ultimately prevent the poisoning of Pt by CO. The addition of an oxophillic promoter may aid in the activation of the C-C bond and the removal of CO as CO_2 from the surface. Recent experiments show both an enhancement in catalytic performance in terms of the overall ethanol oxidation current and the resistance to CO poisoning for Pt-Mo alloys [69, 80, 81].

In order to aid in understanding the mechanism for ethanol oxidation and the enhancement effects reported by the addition of Mo, we have examined the detailed elementary steps involved in the dehydrogenation, C-C bond scission as well as the subsequent oxidation of the C1 species over the model Pt (111) and the model Pt-Mo alloy surfaces shown in Fig. 6.1. The Pt-Mo model surface was chosen to represent a well-dispersed alloy with a Pt-Mo ratio of 2:1 that is within the range of attempted Pt-Mo ratios in experiments [81]. Sections 6.1 to 6.5 will focus on the three most essential steps involved in the complete oxidation process: the dehydrogenation of ethanol, C-C bond activation and C1 species oxidation. The results will be compared side by side to those on the Pt (111) surface to establish a clear understanding of the role of Mo in aiding the complete oxidation of ethanol.

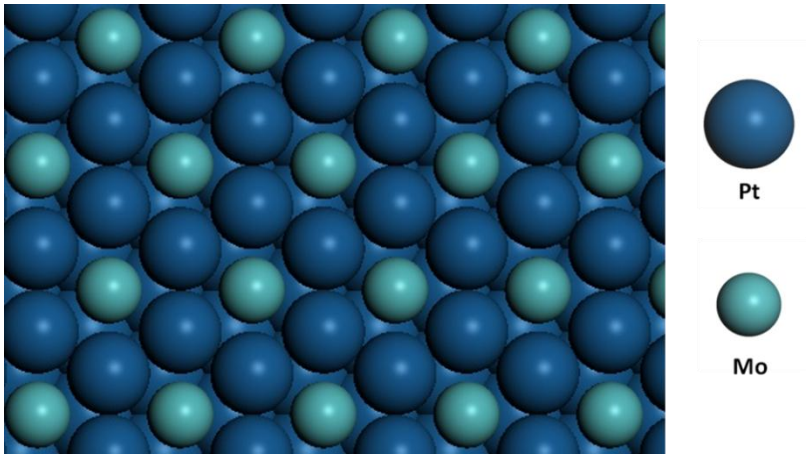

Figure 6.1. Pt_2Mo_1 surface alloy

6.1. Ethanol dehydrogenation

Previous studies indicate that the specific adsorption configuration for ethanol on Pt can influence its oxidation paths. Ethanol can bind to the surface via its oxygen atom sitting in an upright configuration which would promote O-H bond activation. Ethanol can also bind in a more parallel configuration via the weak dispersive interactions with the hydrocarbon backbone thus making σ-C-H bond activation a viable path [46, 195]. Acetaldehyde tends to be the predominant product that forms and is likely the key intermediate for subsequent oxidation [5, 45, 196].

The adsorption energies for ethanol in both configurations and reaction energies and activation barriers for the C-H and O-H activation steps were calculated over both Pt (111) and Pt-Mo alloy

surfaces. We report the results for only the most favorable paths in Fig. 6.2. The energies are all referenced to the gas phase ethanol and the bare metal surface.

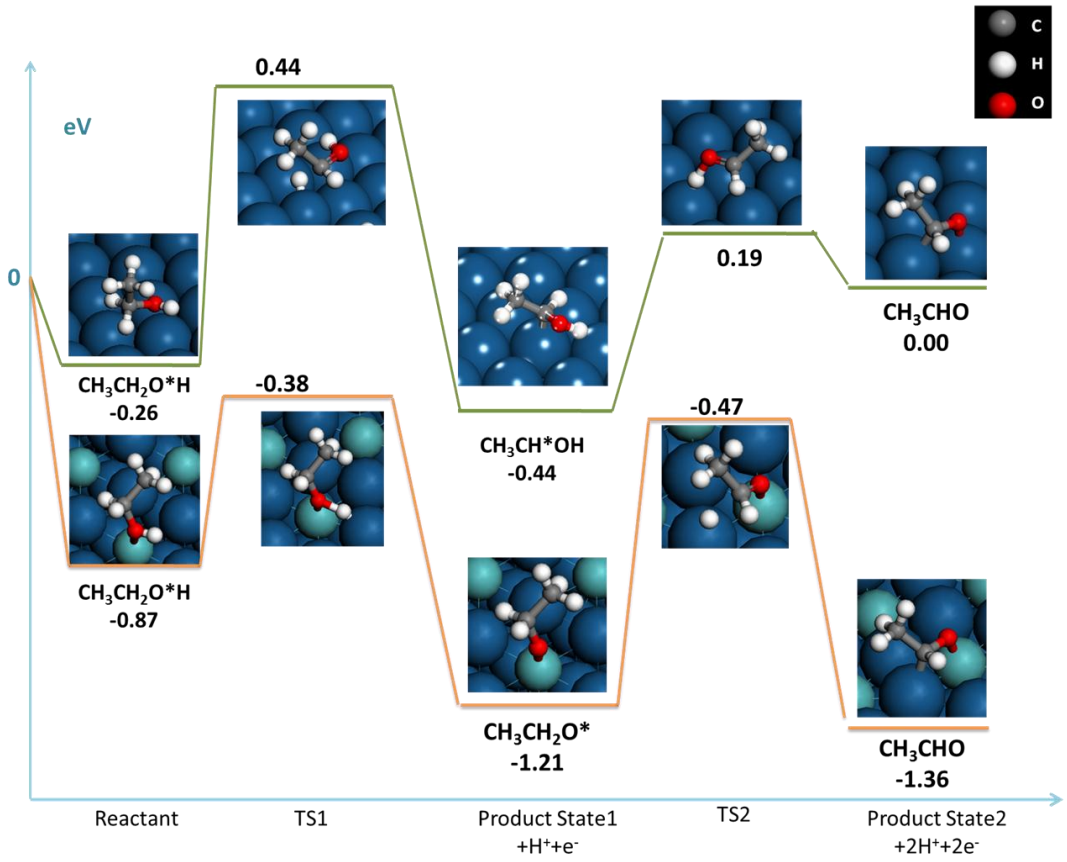

Figure 6.2. Ethanol dehydrogenation to acetaldehyde over the Pt (111) and Pt-Mo (111) surfaces are shown in the green and orange paths respectively.

The interaction between the ethanol O atom and the Pt (111) surface is rather weak with an adsorption energy of -0.26 eV. The adsorption of ethanol on the Pt-Mo (111) surface, on the other hand, is considerably stronger at -0.87 eV as the O of ethanol preferentially binds to the Mo site.

On Pt (111), the activation of ethanol proceeds first via the activation of the α-C-H which has an intrinsic barrier of 0.7 eV. The subsequent activation of the O-H bond was calculated to be 0.63 eV as shown by the green curve in Fig. 6.2. The strong interaction between Mo and O, however, readily promotes the activation of the O-H bond resulting in an intrinsic activation barrier from the adsorbed state of 0.49 eV. The subsequent activation of the α-C-H bond of the strongly held ethoxide is also significantly promoted resulting in a barrier of 0.74 eV as shown by the orange curve in Fig. 6.2. The strong Mo-O interaction helps to promote both the O-H and C-H transition states and leads to an overall potential energy curve that falls below that of Pt.

The strong oxophilicity of Mo results in the formation of a strong Mo-O bond which aids in the activation of the O-H bond of the ethanol, and as will be discussed later, the activation of water, which generates surface OH groups that can play an important role in the oxidation of single C species. It is also found in Fig. 6.2 that the orange curve (Pt-Mo) lies below the green curve (Pt (111)) in energy throughout the dehydrogenation process. The barriers for the activation of both the O-H and C-H bonds on Pt-Mo alloy surface are both lower than those on Pt (111) surface thus indicating that the formation of acetaldehyde is favored on the alloy over that on Pt (111). In both cases, the activation of the β-C-H bond was found to be over 1 eV and as such was considered to be unfavorable.

6.2. C-C activation for acetaldehyde

Carbon-carbon bond activation typically occurs more readily for unsaturated C-C bonds than for saturated C-C bonds. Previous studies for the C-C activation of ethanol over Pt, indicates that ethanol dehydrogenates to form acetaldehyde before C-C activation on Pt as well as Pt based alloys [44, 63, 197]. We therefore start with acetaldehyde in our analysis of the C-C bond activation over Pt and Pt-Mo alloy. The results for the C-C bond activation over both surfaces are reported in Fig. 6.3.

The barriers for C-C activation over both surfaces are greater than 1.5 eV which would suggest that further dehydrogenation of acetaldehyde is necessary before the C-C bond can activate.

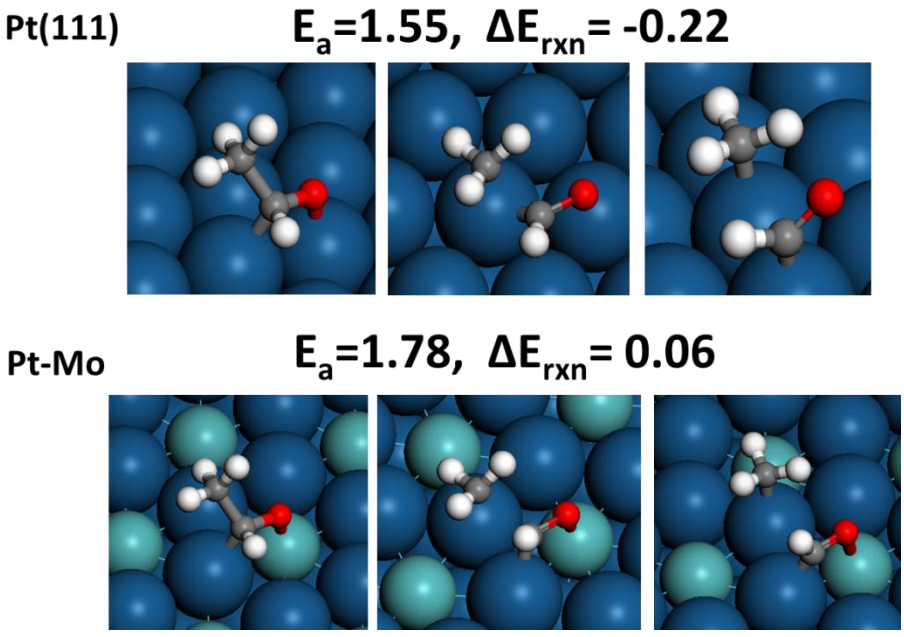

Figure 6.3. C-C bond activation for acetaldehyde adsorbed onto Pt (111) and Pt-Mo alloy surfaces.

6.3. Acetaldehyde dehydrogenation

The elementary C-H activation steps and their energies for the dehydrogenation of acetaldehyde to form CHCO over Pt (111) and Pt-Mo alloy surfaces are reported in Fig. 6.4. Only the most favored paths on both surfaces are shown. The reaction path which proceeds via the primary C-H bond activation have much higher activation barriers than those starting from the activation of the secondary C-H bond regardless of whether the Pt or Pt-Mo alloy is examined. They are therefore not further considered. Complete dehydrogenation paths for acetaldehyde are summarized in Appendix A. On both the Pt (111) and Pt-Mo surfaces, the dehydrogenation of acetaldehyde proceeds via the activation of the α-C-H bond followed by two consecutive β-C-H bond activation steps to form the CHCO* intermediate. By choosing gas phase acetaldehyde as the common reference state, we again find that the catalytic dehydrogenation is thermodynamically more favored over the alloy surface than on Pt. This is attributed to the stronger interaction between the dehydrogenated species and the metal sites on alloy surface. We do not consider starting with the β-C-H activation paths directly as they are not favored due to the strong β-C-H bond thus resulting in activation barriers that are over 1eV.

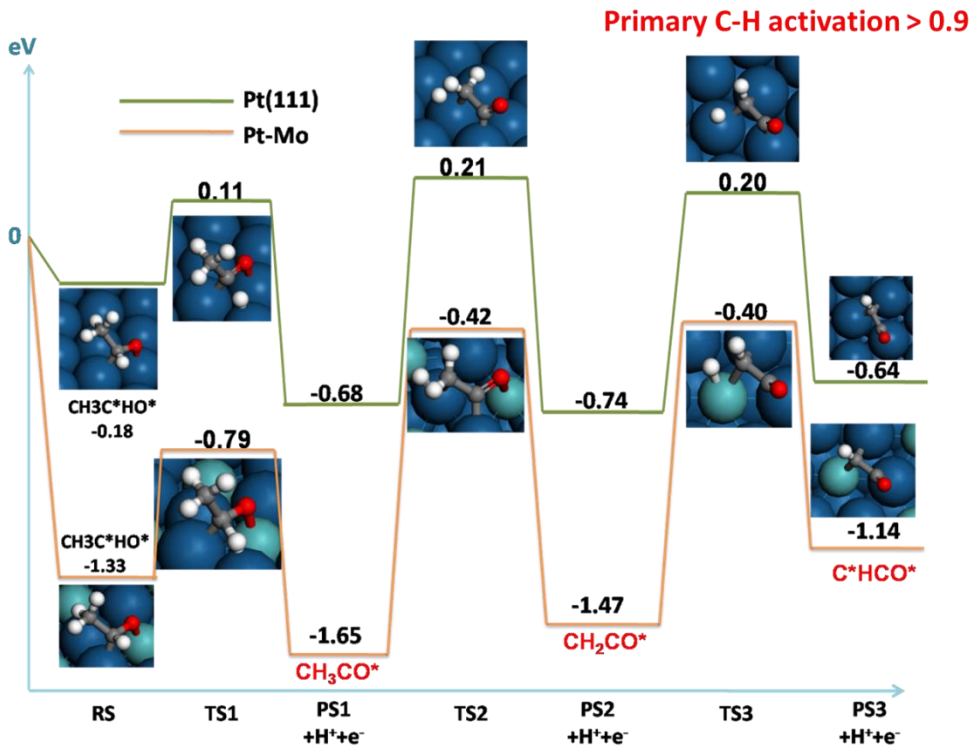

Figure 6.4. The dehydrogenation of acetaldehyde over Pt (111) and Pt-Mo(111) surfaces are shown in the green and orange paths respectively.

The results presented in Fig. 6.4 indicate that the further dehydrogenation of acetaldehyde is thermodynamically more favored on the Pt-Mo alloy surface than on the pure Pt surface, with the entire potential energy diagram for dehydrogenation over the Pt-Mo alloy lying below the energy diagram for pure Pt. A closer inspection of Fig. 6.4, however, indicates that while the overall reaction energies for dehydrogenation are more favorable on the alloy surface, the intrinsic barriers are on average 0.3 eV higher than those on the pure Pt surface. This is characteristically different than the results reported in section 6.1 concerning ethanol dehydrogenation to acetaldehyde, where the alloy surface results in both lower overall energies and intrinsic activation barriers compared to the Pt (111) surface. The predominant

differences in the results reported in Figure 6.4 over the Pt and Pt-Mo surfaces are directly related to the differences in the strength of the surface-oxygen interaction, which again indicates the important role that strong surface Mo-O interaction plays in the reaction. On Pt-Mo alloy surface, as the species become increasingly dehydrogenated, the strong Mo-O interaction together with the strong Pt-C interaction anchor the intermediates to the Mo and Pt surface sites. These strong interactions lead to an increased molecular rigidness, which hinders the ability of the molecule to orient itself to enable further C-H bond activation. This can be demonstrated by the strong binding energy (-1.33 eV) of acetaldehyde on Pt-Mo alloy surface. The absence of these strong Mo-O interactions on the pure Pt (111) surfaces, however, provides enough flexibility to allow both the primary and secondary C-H bonds to freely interact with surface Pt atoms, thus leading to much lower intrinsic dehydrogenation barriers.

The dehydrogenation of acetaldehyde generates three main surface intermediates: CH_3CO, CH_2CO and CHCO, with increasing dehydrogenation extent. The barriers as well as the overall reaction energies for the activation of C-C bonds for each of these intermediates are discussed in the next section.

6.4. C-C bond activation for highly dehydrogenated C2 species

The C-C bond activation paths for the highly dehydrogenated C2 species generated from the dehydrogenation of acetaldehyde discussed above (CH_3CO, CH_2CO and CHCO) were examined over the Pt (111) and the Pt-Mo alloy surfaces. The results which are summarized in Fig. 6.5 are arranged in the order of increasing dehydrogenation extent.

The results show a general decrease in the C-C activation barriers with an increasing degree of dehydrogenation of the C2 surface intermediates on both the Pt (111) and the Pt-Mo surfaces. The C-C activation barriers decrease on Pt (111) from 1.30eV to 0.92eV, while that on the Pt-Mo surface decrease from 1.54eV to 0.47eV. In addition, the overall reaction energies for C-C bond dissociation become increasingly more exothermic with an increase in the extent of dehydrogenation of the reactant. This can be explained, in part, by the increased strength of the Pt-C bond that results upon increasing the degree of C2 dehydrogenation of the acetaldehyde reactant and the increased strength of the Mo-O interaction on the alloy surface. The highly dehydrogenated primary and secondary carbon atoms bind strongly to surface Pt sites, leading to weakened C-C bond and thus lower C-C bond activation barriers. The strong Mo-O interaction also plays a role in coordinating with the Pt-C interaction to enable the activation of the dehydrogenated C2 intermediates, which is illustrated by the C-C activation of CH_3CO and CH_2CO on Pt-Mo in Fig. 6.5. The results on the model Pt-Mo alloy shows that the highly dehydrogenated CHCO surface intermediate leads to a very low C-C activation barrier. The most favored configuration of CHCO on the alloy is one where the primary carbon atom binds to both the Pt and Mo atoms whereas the secondary carbon binds to a neighboring Pt

atom with its oxygen oriented away from the surface. The C-C cleavage occurs within the triangular Pt-Pt-Mo ensemble resulting in the strongly bound CH and CO intermediates. The activation barrier at this site is only 0.47 eV which is significantly lower than the barriers to activate the C-C bonds of CH_3CO (1.54 eV) and CH_2CO (1.24 eV) intermediates. The higher barriers for the CH_3CO and CH_2CO intermediates result from the significant energy penalty required to break the strong Mo-O interactions in the transition state. The CHCO* intermediate binds to the surface predominantly through its C-C bond with little to no interaction with its oxygen and as a result does not require breaking the Mo-O bond.

The decrease in the C-C activation barriers over Pt with increasing dehydrogenation is less significant than those on the Pt-Mo surface. This is due to the absence of Mo atoms on the Pt (111) surface, where the C-C bond cleaves only via the primary and secondary C-Pt interactions, which are less affected by the extent of dehydrogenation. On the Pt-Mo alloy surface, the decrease is more specifically related to the loss of Mo-O interactions during the transition states for CH_3CO and CH_2CO which are not present for CHCO, as well as the change in the specific surface metal atoms that CH_3CO and CH_2CO interact with. These changes do not occur on the homogeneous Pt (111) surface. The C-C bond activation on Pt (111) starts out with a barrier that is 0.2 eV lower than that on the model Pt-Mo alloy surface, but ends up staying at around 1.0 eV as the dehydrogenation extent continues to increase.

The results in Figure 6.5 as was discussed indicate that C-C activation becomes increasingly more favorable as the surface intermediates become increasingly more dehydrogenated. As such, it can be assumed that dehydrogenation of ethanol proceeds on either the Pt or Pt-Mo sites on the Pt (111) or model Pt-Mo surfaces, respectively until the intermediates reach a high extent of dehydrogenation. The C-C bond cleavage path will then follow, catalyzed by the alloy sites.

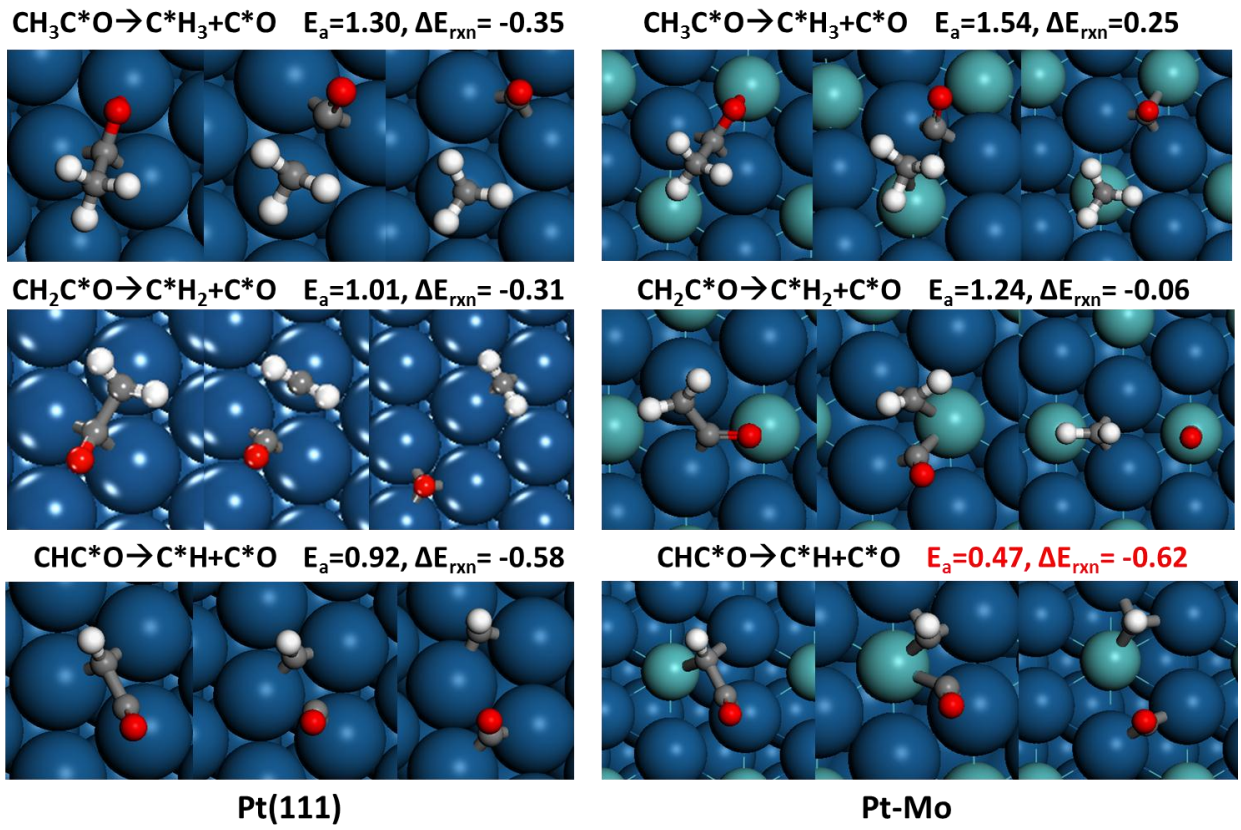

Figure 6.5. The activation of the C-C bond on the Pt (111) and Pt-Mo surfaces with increasing extents of dehydrogenation of the β-C bonds.

6.5. A microkinetic study of the dehydrogenation and C-C bond activation process

The results presented in Fig. 6.4 indicate that while the overall energetics favor the dehydrogenation of the acetaldehyde over the Pt-Mo alloy surface than over the pure Pt (111) surface as the intermediates that form on the alloy are strongly held to the surface via the strong interactions between the O of the CH_xCO intermediates and the Mo sites, the activation barriers, however, were found to be significantly lower over the Pt (111) surface than those on the alloys.

The results presented in Fig. 6.5 indicate that while the C-C activation barrier are lower for CH_3CO and CH_2CO over the Pt surface, the Pt-Mo alloy has the lowest barrier of all but requires very high extents of dehydrogenation and the formation of the CHCO surface intermediate. The Pt (111) surface may be able to promote the dehydrogenation of CH_3CHO to CHCO, but fail to cleave the C-C bond.

While the C-H and C-C activation barriers and energies reported in Fig. 6.4 and 6.5 are helpful, they cannot be used alone to determine the catalytic outcome from such a complex set of reactions. We therefore constructed a simple microkinetic model to simulate the catalytic kinetics for the catalytic dehydrogenation and C-C activation of acetaldehyde over the model Pt

(111) and Pt-Mo surfaces. All seven of the calculated elementary steps presented in Fig. 6.4 and 6.5 involved in the dehydrogenation and decomposition of CH_3CHO to CO are incorporated into the analysis.

The microkinetic model is thoroughly described and widely applied in literatures [198-205]. The rate for adsorption is given by $k_{ADS}P_A\theta_*$, where P_A and θ_* refer to the partial pressure (acetaldehyde) and fractional surface coverage of free sites. The rate constant for adsorption, k_{ADS}, is estimated from collision theory to be $10^7 s^{-1}$ [206-208]. The rate constant k_i for surface reactions is $\nu_i e^{-\frac{\Delta E_i}{RT}}$, where ν_i is the pre-expotential factor and ΔE_i is the calculated energy barrier for each elementary step. The pre-expotential factors for the surface elementary reaction rate constants are estimated from transition state theory to be on the order of $10^{13} s^{-1}$ [205, 209]. The pre-expotential factor for desorption is also estimated to be around the magnitude of $10^{13} s^{-1}$ [199]. The simulation results were found to depend only weakly on the chosen values for the pre-expontential factors [209].

The microkinetic simulations were carried out here by assuming that all seven elementary steps involved in CO formation from CH_3CHO could proceed by their forward and reverse paths. A temperature of 350 K (operating temperature for PEMFCs), along with the DFT-calculated activation barriers were used to calculate the rate constants for each of the elementary steps. The simulations were then carried out to determine the equilibrium concentrations for each intermediate (expressed in terms of surface coverage). More Details regarding the microkinetic

model are included in Appendix B. The results are shown in Fig. 6.6. We focus herein solely on the changes in the magnitudes of surface coverages of different surface species due to the approximations used to establish the microkinetic model.

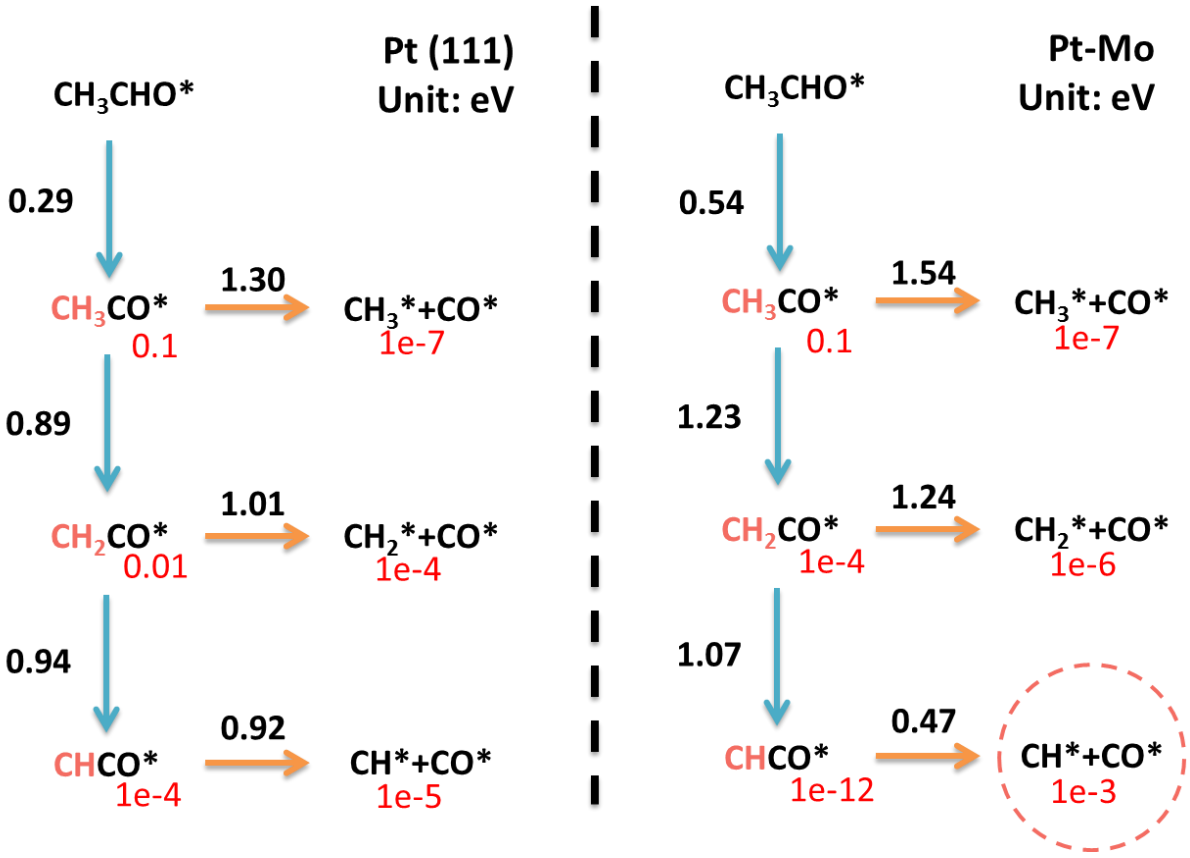

Figure 6.6. The orders of simulated steady state surface coverages for reaction intermediates during the dehydrogenation and C-C bond activation processes as calculated by the microkinetic model are shown in red. The vertical paths represent the dehydrogenation of CH_3CHO down to CHCO. The horizontal paths represent the C-C bond activation processes that generate C1 species from the CH_3CO, CH_2CO and CHCO intermediates.

The simulated steady state surface coverage results reported in Fig. 6.6 indicate that dehydrogenation proceeds more readily over Pt (111) than on Pt-Mo as the equilibrium surface coverage of CH_2CO on Pt is 0.01 and only 1e-4 on Pt-Mo whereas CHCO is 1e-4 on Pt and only trace amount on Pt-Mo. The results also show that dehydrogenation process becomes increasingly more difficult as the dehydrogenation extent increases, as indicated by the dramatic drop in surface concentrations of the C2 species as the dehydrogenation proceeds deeper.

A detailed analysis of the surface coverage of C1 intermediates reveals that surface coverage of C1 species on the Pt (111) surface is rather small with 1e-4 highest. The surface coverage of CO species that form on Pt-Mo at high extents of dehydrogenation, however, was calculated to be nearly 10 times higher (1e-3 as highlighted by the red circle in Fig. 6.6). The results suggest that while the dehydrogenation of CH_3CHO to CHCO is difficult on the alloy surface, the trace amount of CHCO formed is enough to generate higher CO concentrations on the Pt-Mo surface than on the Pt (111) surface due to the low C-C activation barrier for CHCO on the alloy surface. The result indicate that the higher catalytic activity towards C-C cleavage at high dehydrogenation levels on Pt-Mo might be one reason for the experimentally observed enhancement in the overall ethanol oxidation current on Pt-Mo alloy surfaces [69, 80, 81].

Another reason for the enhancement in the oxidation current that might account for the increase in the overall ethanol oxidation current on the alloy surface is the possible bimetallic

or bi-functional effect of Mo in aiding the removal of CO from Pt sites. The oxidative removal of C1 species is further studied in the subsequent sections.

6.6. Oxidative removal of C1 species

The C1 species, and more specifically CO, that form during the oxidation of ethanol are strongly bound to the surface Pt sites as suggested by experiments and shown in our calculations [5, 46, 195]. The oxidative removal of CO as well as the C_1H_x intermediates is necessary in order to expose active surface Pt sites needed to sustain the oxidation cycle. Both the bi-functional and the ligand effects may be present which will aid in the oxidation of CO [43, 84-89]. In the bi-functional mechanism, the oxidation process of the C1 species bound to Pt proceeds via the reaction with OH* that forms via the activation of water molecules at the neighboring oxophillic metal site. In the ligand effect, the strong Pt-Mo bond acts to weaken the binding of CO to Pt thus facilitating its desorption. Our calculation indicates that while both mechanisms are operative the bi-functional effect is the dominant mechanism, as we find only small variations in activation barriers and reactions energies as additional Mo atoms are introduced to the second layer of the metal to account for additional ligand effect. Therefore the subsequent sections will mainly focus on the illustration of Mo's bi-functional effect in promoting CO oxidation. A further discussion of the ligand effect is also provided at the end of this section.

6.6.1. Water activation on surface Mo

The water activation process on both Pt and Pt-Mo alloy surfaces is shown in Fig. 6.7. The binding energies in Fig. 6.7a and 6.7b indicate that water binds more strongly to the surface Mo sites than to the surface Pt sites. The subsequent activation of the O-H bonds also proceeds with considerably lower barriers on the Mo sites (~0.5 eV) shown in Fig. 6.7b than on the Pt sites (~1.0 eV) shown in Fig. 6.7a. It is noted that the two O-H activation steps on the alloy surface shown in 6.7b and 6.7c that sequentially convert water to O* both have barriers of approximately 0.5 eV, which are very similar to the barriers for the O-H activation processes of C2 species on the alloy surface, indicating it is the same strong Mo-O interaction that acts to lower the O-H activation barrier. The results here help to explain in part the improved activity of Pt-Mo over Pt. It is difficult for pure Pt alone to drive the $12e^-$ process involved in the oxidation of ethanol as it cannot generate OH* intermediates fast enough to oxidatively remove the C1 species that form on the surface. As a result, CO can build up and poison the surface. The addition of Mo can ultimately aid in the generation of OH* sites which are active in the dehydrogenation of C1 and C2 intermediates and oxidation of the C1 species to form CO_2.

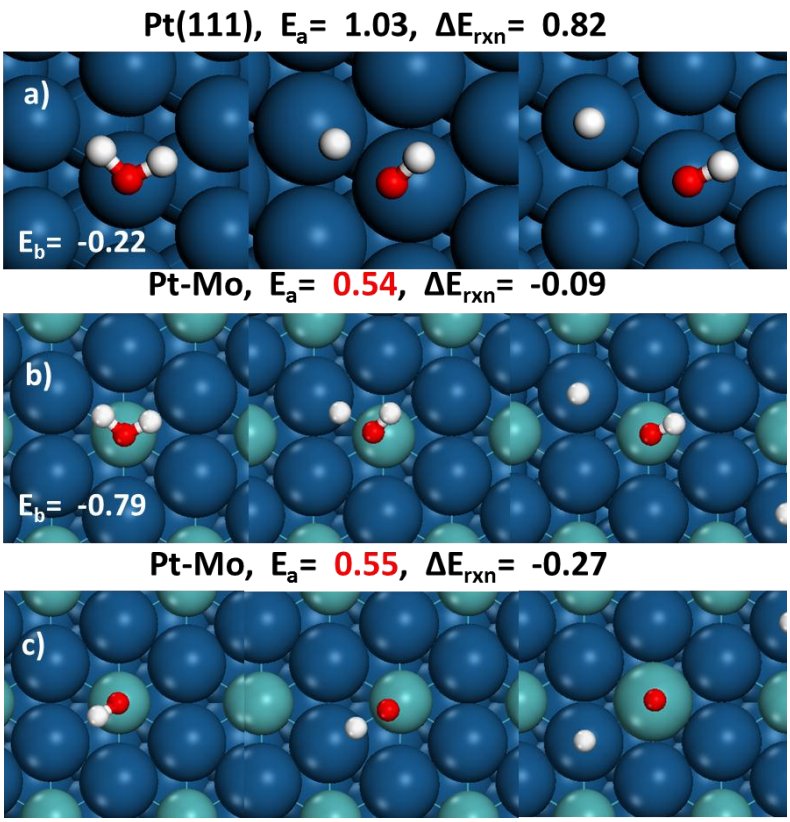

Figure 6.7. The activation of water to OH* and H* and the subsequent activation of OH* to O* and H* over the Pt (111) and Pt-Mo surfaces.

6.6.2. C1 species oxidation/dehydrogenation

A thorough study of the removal of C1 species is complicated since there are at least five surface species, CH_3, CH_2, CH, CHO and CO that can form and each of them can be oxidized by either OH* or O* or go through further dehydrogenation either by the metal or via OH* or O* surface intermediates. The final product is CO_2 which typically marks the end of the complete oxidation process. Fig. 6.8 illustrates the most favored reaction path for the dehydrogenation of

CH_3 to CO_2. Complete C1 species oxidation and dehydrogenation paths are summarized in Appendix C.

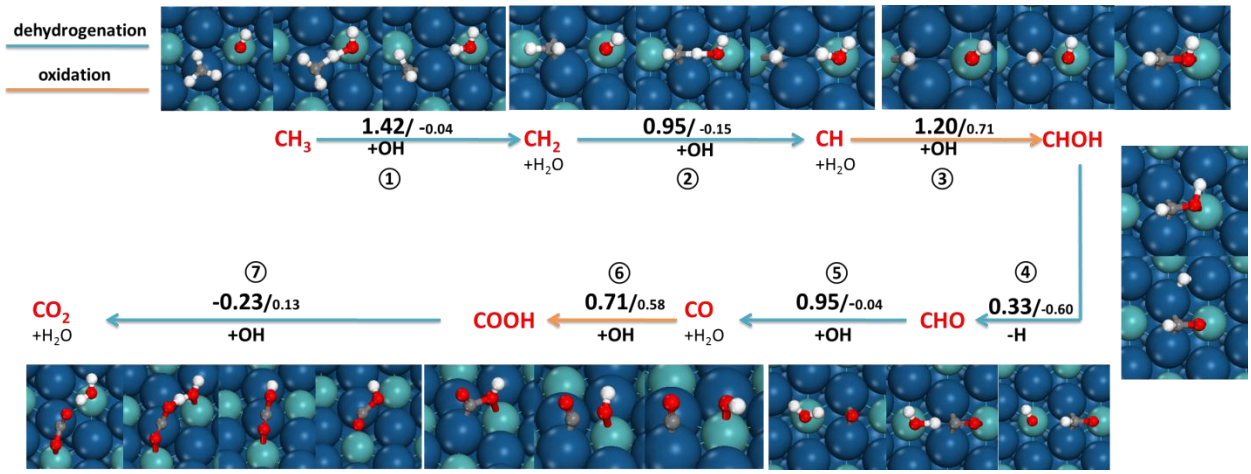

Figure 6.8. Most favored paths in the oxidative removal of the C1 species from the Pt-Mo surface.

Most of the dehydrogenation and oxidation steps reported for the oxidation of CH_x species over the Pt-Mo alloy presented in Fig. 6.8 require direct assistance from surface OH groups bound to Mo. CH_3, CH_2 mainly proceed through the dehydrogenation of CH_3 and CH_2 to CH. In this stage (① and ② in Fig. 6.8) the C1 species gradually migrate from the atop Pt site to the 3-fold site. Further dehydrogenation of CH is not favored since it results in the formation of C atoms that are less stable than the CH species on the surface. CH predominantly reacts on the Pt-Mo surface with OH* to form CHOH, which can readily decompose to CHO upon the activation of the O-H bond. CHO can then continue via a second dehydrogenation reaction to form CO. During this stage (③, ④ and ⑤in Fig. 6.8), the C1 species gradually migrate from the 3-fold site back to the Pt-atop site. The activation barriers for these dehydrogenation/oxidation steps are all on average ~1eV. The higher barriers here are the result of the strong interaction

between the C1 species and the Pt surface. This strong interaction increases the barriers associated with the migration of C1 intermediates between different metal sites. The final step in the oxidation of the C1 species involves the addition of OH to CO to form COOH. This step proceeds with a barrier of 0.73 eV. The COOH is readily deprotonated to form CO_2 that desorbs from the surface with an energy barrier of 0.46 eV.

All of the paths shown in Fig. 6.8 require either OH bound to Mo to assist in C-H and O-H activation or to add to the adsorbed C1 intermediate or an adjacent surface Mo site to activate the O-H bonds of ethanol or water. As these sites are not present on Pt, the Mo helps to promote the overall oxidation of ethanol to CO_2.

6.6.3. A comparison study of main C1 dehydrogenation/oxidation steps with additional Mo atoms introduced to the subsurface layer

It is well established that an alloy can induces both ensemble (geometric) as well as ligand (electronic) effects that can influence the catalytic kinetics. While the model Pt-Mo surface provides both ensemble as well as ligand effects due to the interaction of surface or neighboring Mo sites, it did not consider the electronic or ligand effects via subsurface Mo sites. Electronic or ligand effects can be significant and so we explicitly included Mo to the subsurface to examine its effect. The results in Table 6.1 indicate there is very little change in most of the

barriers due to the incorporation of the subsurface Mo sites. Complete C1 species dehydrogenation and oxidation paths on Pt-Mo alloy surface with additional subsurface Mo sites are also included in Appendix C.

	Pt-Mo (Mo also in subsurface layer)		Pt-Mo	
	ΔE_{act} (eV)	ΔE_{rxn} (eV)	ΔE_{act} (eV)	ΔE_{rxn} (eV)
$H_2O^* \rightarrow OH^* + H^*$	0.54	-0.14	0.53	-0.09
$OH^* \rightarrow O^* + H^*$	0.55	-0.31	0.55	-0.27
$CH_3^* + OH^* \rightarrow CH_2^* + H_2O^*$	**1.22**	0.04	**1.42**	-0.04
$CH_2^* + OH^* \rightarrow CH^* + H_2O^*$	**0.79**	-0.24	**0.95**	-0.15
$CH^* + OH^* \rightarrow CHOH^*$	1.27	0.75	1.20	0.71
$CHOH^* \rightarrow CHO^* + H^*$	**0.63**	-0.57	**0.33**	-0.60
$CHO^* + OH^* \rightarrow CO^* + H_2O^*$	1.06	0.13	0.95	-0.04
$CO^* + OH^* \rightarrow COOH^*$	0.66	0.52	0.71	0.58
$COOH^* + OH^* \rightarrow CO_2^* + H_2O^*$	-0.21	0.16	-0.23	0.13

Table 6.1. C1 dehydrogenation/oxidation barriers and reaction energies for Pt-Mo alloy surfaces with Mo sites present in subsurface, as compared to the case with no Mo added to the subsurface layer.

It can be seen from Table 6.1 that other than three reactions ($CH_3^* + OH^* \rightarrow CH_2^* + H_2O^*$, $CH_2^* + OH^* \rightarrow CH^* + H_2O^*$ and $CHOH^* \rightarrow CHO^* + H^*$), the majority of the activation barriers and reaction energies roughly stay the same when additional Mo atoms have been introduced to

the metal subsurface layer. This suggests that their electronic or ligand effects in the C1 dehydrogenation/oxidation process are weak. There are, however, a few steps which show a decrease in activation barriers upon the addition of subsurface Mo which include the dehydrogenation of CH_3* and CH_2* via adsorbed OH*. There is also one reaction for which the barrier increases due to the presence of subsurface Mo. This involves the direct O-H bond activation via (CHOH*→CHO*+H*) where dehydrogenation proceeds without the aid from OH* groups. This may be due to the fact that this reaction requires stretching the O-H bond between a Mo-Pt metal site pair. Increasing the Mo content within the subsurface layer will strengthen the interaction between the oxygen atom of CHOH* and the surface Mo atoms, leading to increased dehydrogenation barrier. The result that the ligand effect is generally less dominant in the C1 dehydrogenation/oxidation process than the bi-functional effect is consistent with recent experimental observations [80, 87].

6.7. Conclusion

The complete ethanol oxidation proceeds via dehydrogenation of ethanol to acetaldehyde which is consistent with the results reported in the literature [5, 44, 45, 63, 196, 197]. On the ideal Pt (111) surface, the dehydrogenation of ethanol proceeds via α-C-H activation followed by O-H activation, while on the Pt-Mo surface, the O-H bond activation preferentially occurs at the Mo centers due to the strong Mo-O interactions. C-C bond activation generally requires high extent of dehydrogenation of the C2 species. It was observed that the C-C bond activation

barriers decrease as the dehydrogenation extent increases on both pure Pt and Pt-Mo alloy surfaces. A low C-C activation barrier of 0.47 eV can be achieved for CHCO on the Pt-Mo surface. A microkinetic study reveals that the Pt-Mo alloy surface further promotes C-C bond activation as it can readily dissociate CHCO via a low barrier process. While the Pt (111) surface has a higher surface coverage of CHCO intermediates, it cannot readily promote the subsequent activation of the C-C bond due to high C-C activation barriers.

The C1 species generated by the C-C activation process can severely poison the surface Pt sites. The removal of these requires the assistance from surface OH groups, which predominantly form at the Mo sites which readily activate water. All the O-H bond activation steps on the alloy surface are dominated by the same Mo-O interaction, and as a result they all have similar activation barriers of 0.5 eV. The C1 species proceed through a sequence of dehydrogenation/oxidation steps aided by the surfaced OH groups and eventually form CO, which will then be further oxidized to CO_2. Water is not activated on the Pt surface, as the barriers to break the O-H bond are higher on Pt alone and these surfaces are covered in CO. As such the C1 oxidation pathways are only viable on the Pt-Mo alloy surface.

Chapter 7. Summary and recommendations for future work

We have analyzed a range of non-precious metal carbon materials that can begin to compete with Pt as electrocatalysts for the reduction of oxygen at the cathode as well as a 2-to-1 Pt-Mo alloy that may improve the performance of Pt catalysts used at the anode in the oxidation of ethanol for proton exchange membrane fuel cells.

On the cathode, we have shown that the very cheap nitrogen and transition metal doped carbon based catalysts identified in the literature can readily promote ORR in a mechanism that is consistent with how ORR is carried out over Fe heme structures in nature. The results presented herein indicate that the choice of transition metal and the location and composition of the N within carbon (graphene) are essential factors that control the overall ORR activities of these catalysts. Fe centers within the nitrogen doped graphene predominantly promote the $4e^-$ ORR process at potentials of about 0.6 - 0.7 V. The Co center on the other hand tends to catalyzes only $2e^-$ ORR. The difference in ORR activity was found to consist in the different abilities of the metal centers to backdonate d electrons to the antibonding orbitals of oxygen, especially the σ* orbital, of oxygen. The results indicate that the Fe-N_4 sites between graphene edges generally possess the highest catalytic activity, but suffer more from structure instability and poisoning from O* species as compared to Fe-N_4 sites on graphene basal planes. Further studies on the N-doped carbon materials indicate the carbon sites near the doped N atoms can

also serve as active sites and promote ORR, though the activity was found to be slightly lower than the systems that contain metals.

A 2-to-1 Pt-Mo surface alloy was examined at the anode for its catalytic activity in promoting the complete oxidation of ethanol. As compared to pure Pt, the alloy surface was calculated to facilitate a higher degree of C-C bond activation resulting from the formation of the highly dehydrogenated CHCO species that is readily activated on the Pt-Mo surface. The dehydrogenation of CH_3CHO to form CHCO, however, was found to be more difficult on the alloy surface than on the Pt (111) surface. Kinetic analysis suggests that while the dehydrogenation is slow it still proceeds over the alloy and results in much higher rates of C-C activation over the alloy than on pure Pt. The subsequent removal of C1 species is further promoted on the alloy surface predominantly due to Mo's bi-functional effect. The Pt (111) surface, on the other hand, suffers from severe poisoning from C1 species due to the lack of oxophilic surface Mo sites.

It has been reported that co-facial double Co-N_4 centers can significantly increase ORR activity as compared to single Co-N_4 centers and are capable of catalyzing the $4e^-$ ORR [149-151]. It is also known that cytochrome c efficiently carries out ORR over the Fe^{II} center at the heme Fe-N_4 together with the coexistence and co-promotion from a neighboring histidine group which contains a Cu center[104]. Both of these systems suggest that bi-functional metal centers are effective in the activation of O_2. Therefore one possible extension of this work would be to

examine bi-functional metal sites that mimic the Fe-Cu sites in cytochrome c. The Cu site may act as a Lewis acid which can help promote the proton coupled electron transfer. We can therefore attempt to analyze both the 2e- and 4e- paths over the TM-N_4 carbon systems in microporous systems where we can anchor Cu and other transition metal complexes that could help to promote the reaction. The computation intensity of examining complex systems such as this will require significant computational resources to model the site, the interfaces, the presence of water and an applied potential thus making such a study challenging.

The work on metal free N-doped carbon materials can also be further expanded to examine the various other N-doping configurations on graphene basal planes as well as on graphene edges to establish a more general correlation between N-doping configurations and the ORR catalytic activities of the resulting carbon active sites. The challenge in this direction is the prohibitive number of possible N-doping configurations that might arise from various synthesis techniques and the lack of experimental evidences for detailed active site structures.

The work on ethanol oxidation presented in chapter 6 clearly indicated that the resulting performance of such systems is rather complex and requires a more detailed kinetic studies. A more rigorous KMC model has been developed in our group and can be used to more accurately treat the surface kinetics for the overall oxidation process other than just estimates of surface species coverage. The results reported herein suggest that OH* species formed via the activation of water at the Mo sites can oxidize CO and dehydrogenate and oxidize other C1

species on the neighboring Pt sites thus promoting the removal of CO and C1 and mitigating poisoning [87, 210, 211]. Kinetic Monte Carlo simulations would allow us to simulate the activation barriers and reaction energies for all of the elementary steps and fully establish the effects of alloying on the ethanol oxidation. Additional DFT calculations along with these simulations could then be carried out to explore the effects of alloy composition and the spatial arrangement effects of the Pt and Mo. The work can also be extended to other metal alloy surfaces.

Acknowledgement

This work was supported as part of the Fluid Interface Reactions, Structures and Transport (FIRST) Center, an Energy Frontier Research Center funded by the U.S. Department of Energy, Office of Science, Office of Basic Energy Sciences under Award Number ERKCC61.

References

1. Antolini, E. and E.R. Gonzalez, *Alkaline direct alcohol fuel cells.* J. Power Sources, 2010. **195**(11): p. 3431-3450.
2. Maget, H.J.R., Handbook of Fuel Cell Technology, 1968. **Chapter 2**.
3. Vishnyakov, A. and A.V. Neimark, *Molecular dynamics simulation of microstructure and molecular mobilities in swollen Nafion membranes.* J. Phys. Chem. B, 2001. **105**(39): p. 9586-9594.
4. Wakizoe, M., O.A. Velev, and S. Spinivasan, *Analysis of proton exchange membrane fuel cell performance with alternate membranes.* Electrochim. Acta, 1995. **40**(3): p. 335-44.
5. Lamy, C., A. Lima, V. LeRhun, F. Delime, C. Coutanceau, and J.M. Leger, *Recent advances in the development of direct alcohol fuel cells (DAFC).* Journal of Power Sources, 2002. **105**(2): p. 283-296.
6. Ogden, J.M., M.M. Steinbugler, and T.G. Kreutz, *A comparison of hydrogen, methanal and gasoline as fuels for fuel cell vehicles: implications for vehicle design and infrastructure development.* Journal of Power Sources, 1999. **79**(2): p. 143-168.
7. Wee, J.-H., *Applications of proton exchange membrane fuel cell systems.* Renewable Sustainable Energy Rev., 2007. **11**(Copyright (C) 2014 American Chemical Society (ACS). All Rights Reserved.): p. 1720-1738.
8. Li, Q., R. He, J.O. Jensen, and N.J. Bjerrum, *Approaches and recent development of polymer electrolyte membranes for fuel cells operating above 100°.* Chem. Mater., 2003. **15**(26): p. 4896-4915.
9. Litster, S. and G. McLean, *PEM fuel cell electrodes.* J. Power Sources, 2004. **130**(1-2): p. 61-76.
10. Smitha, B., S. Sridhar, and A.A. Khan, *Solid polymer electrolyte membranes for fuel cell applications - a review.* J. Membr. Sci., 2005. **259**(1-2): p. 10-26.
11. Owejan, J.P., J.E. Owejan, W.B. Gu, T.A. Trabold, T.W. Tighe, and M.F. Mathias, *Water Transport Mechanisms in PEMFC Gas Diffusion Layers.* Journal of the Electrochemical Society, 2010. **157**(10): p. B1456-B1464.
12. Yousfi-Steiner, N., P. Mocoteguy, D. Candusso, and D. Hissel, *A review on polymer electrolyte membrane fuel cell catalyst degradation and starvation issues: Causes, consequences and diagnostic for mitigation.* Journal of Power Sources, 2009. **194**(1): p. 130-145.
13. Miller, M. and A. Bazylak, *A review of polymer electrolyte membrane fuel cell stack testing.* Journal of Power Sources, 2011. **196**(2): p. 601-613.
14. Chu, D. and R.Z. Jiang, *Comparative studies of polymer electrolyte membrane fuel cell stack and single cell.* Journal of Power Sources, 1999. **80**(1-2): p. 226-234.
15. Urbani, F., O. Barbera, G. Giacoppo, G. Squadrito, and E. Passalacqua, *Effect of operative conditions on a PEFC stack performance.* International Journal of Hydrogen Energy, 2008. **33**(12): p. 3137-3141.
16. Giddey, S., F.T. Ciacchi, and S.P.S. Badwal, *Design, assembly and operation of polymer electrolyte membrane fuel cell stacks to 1 kW(e) capacity.* Journal of Power Sources, 2004. **125**(2): p. 155-165.
17. Berg, P., K. Promislow, J. St. Pierre, J. Stumper, and B. Wetton, *Water Management in PEM Fuel Cells.* J. Electrochem. Soc., 2004. **151**(3): p. A341-A353.
18. Zawodzinski, T.A., Jr., T.E. Springer, J. Davey, R. Jestel, C. Lopez, J. Valerio, and S. Gottesfeld, *A comparative study of water uptake by and transport through ionomeric fuel cell membranes.* J. Electrochem. Soc., 1993. **140**(7): p. 1981-5.

19. Zawodzinski, T.A., Jr., C. Derouin, S. Radzinski, R.J. Sherman, V.T. Smith, T.E. Springer, and S. Gottesfeld, *Water uptake by and transport through Nafion 117 membranes.* J. Electrochem. Soc., 1993. **140**(4): p. 1041-7.
20. Zawodzinski, T.A., J. Davey, J. Valerio, and S. Gottesfeld, *The water content dependence of electro-osmotic drag in proton-conducting polymer electrolytes.* Electrochim. Acta, 1995. **40**(3): p. 297-302.
21. Ji, M. and Z. Wei, *A review of water management in polymer electrolyte membrane fuel cells.* Energies (Basel, Switz.), 2009. **2**(4): p. 1057-1106.
22. Le Canut, J.-M., R.M. Abouatallah, and D.A. Harrington, *Detection of Membrane Drying, Fuel Cell Flooding, and Anode Catalyst Poisoning on PEMFC Stacks by Electrochemical Impedance Spectroscopy.* J. Electrochem. Soc., 2006. **153**(5): p. A857-A864.
23. Van Nguyen, T. and M.W. Knobbe, *A liquid water management strategy for PEM fuel cell stacks.* J. Power Sources, 2003. **114**(1): p. 70-79.
24. Springer, T.E., T.A. Zawodzinski, and S. Gottesfeld, *Polymer electrolyte fuel cell model.* J. Electrochem. Soc., 1991. **138**(8): p. 2334-42.
25. Watanabe, M., H. Uchida, and M. Emori, *Polymer Electrolyte Membranes Incorporated with Nanometer-Size Particles of Pt and/or Metal-Oxides: Experimental Analysis of the Self-Humidification and Suppression of Gas-Crossover in Fuel Cells.* J. Phys. Chem. B, 1998. **102**(17): p. 3129-3137.
26. Inaba, M., T. Kinumoto, M. Kiriake, R. Umebayashi, A. Tasaka, and Z. Ogumi, *Gas crossover and membrane degradation in polymer electrolyte fuel cells.* Electrochim. Acta, 2006. **51**(26): p. 5746-5753.
27. Liu, W., K. Ruth, and G. Rusch, *Membrane durability in PEM fuel cells.* J. New Mater. Electrochem. Syst., 2001. **4**(4): p. 227-231.
28. Hansen, J.-P. and H. Lowen, *Effective interactions between electric double layers.* Annu. Rev. Phys. Chem., 2000. **51**: p. 209-242.
29. Parsons, R., *The electrical double layer: recent experimental and theoretical developments.* Chemical Reviews, 1990. **90**(5): p. 813-826.
30. Stern, O., *The theory of the electrolytic double-layer.* Z. Elektrochem. Angew. Phys. Chem., 1924. **30**: p. 508-16.
31. Grahame, D.C., *Effects of dielectric saturation on the diffuse double layer and the free energy of hydration of ions.* J. Chem. Phys., 1950. **18**: p. 903-9.
32. Proskurnin, M. and A. Frumkin, *A new determination of the capacity of the electrical double layer.* Transactions of the Faraday Society, 1935. **31**(0): p. 110-115.
33. Grahame, D.C., *The Electrical Double Layer and the Theory of Electrocapillarity.* Chemical Reviews, 1947. **41**(3): p. 441-501.
34. Filhol, J.S. and M. Neurock, *Elucidation of the electrochemical activation of water over Pd by first principles.* Angewandte Chemie-International Edition, 2006. **45**(3): p. 402-406.
35. Haile, S.M., *Fuel cell materials and components.* Acta Mater., 2003. **51**(19): p. 5981-6000.
36. Herrera, O.E., D.P. Wilkinson, and W. Merida, *Anode and cathode overpotentials and temperature profiles in a PEMFC.* J. Power Sources, 2012. **198**: p. 132-142.
37. Greeley, J., I.E.L. Stephens, A.S. Bondarenko, T.P. Johansson, H.A. Hansen, T.F. Jaramillo, J. Rossmeisl, I. Chorkendorff, and J.K. Norskov, *Alloys of platinum and early transition metals as oxygen reduction electrocatalysts.* Nat. Chem., 2009. **1**(7): p. 552-556.
38. Taylor, C.D., S.A. Wasileski, J.S. Filhol, and M. Neurock, *First principles reaction modeling of the electrochemical interface: Consideration and calculation of a tunable surface potential from atomic and electronic structure.* Physical Review B, 2006. **73**(16).

39. Janik, M.J., C.D. Taylor, and M. Neurock, *First-Principles Analysis of the Initial Electroreduction Steps of Oxygen over Pt(111).* Journal of the Electrochemical Society, 2009. **156**(1): p. B126-B135.
40. Yu, X. and S. Ye, *Recent advances in activity and durability enhancement of Pt/C catalytic cathode in PEMFC.* J. Power Sources, 2007. **172**(Copyright (C) 2014 American Chemical Society (ACS). All Rights Reserved.): p. 145-154.
41. Song, S. and P. Tsiakaras, *Recent progress in direct ethanol proton exchange membrane fuel cells (DE-PEMFCs).* Appl. Catal., B, 2006. **63**(Copyright (C) 2014 American Chemical Society (ACS). All Rights Reserved.): p. 187-193.
42. Yu, X. and S. Ye, *Recent advances in activity and durability enhancement of Pt/C catalytic cathode in PEMFC.* J. Power Sources, 2007. **172**(Copyright (C) 2014 American Chemical Society (ACS). All Rights Reserved.): p. 133-144.
43. Vigier, F., S. Rousseau, C. Coutanceau, J.M. Leger, and C. Lamy, *Electrocatalysis for the direct alcohol fuel cell.* Topics in Catalysis, 2006. **40**(1-4): p. 111-121.
44. Neurock, M., *First-principles modeling for the electro-oxidation of small molecules*, in *Handbook of Fuel Cells*. 2010, John Wiley & Sons, Ltd.
45. Taneda, K. and Y. Yamazaki, *Study of direct type ethanol fuel cells - Analysis of anode products and effect of acetaldehyde.* Electrochimica Acta, 2006. **52**(4): p. 1627-1631.
46. Vigier, F., C. Coutanceau, A. Perrard, E.M. Belgsir, and C. Lamy, *Development of anode catalysts for a direct ethanol fuel cell.* Journal of Applied Electrochemistry, 2004. **34**(4): p. 439-446.
47. Gacutan, E.M., M.I. Climaco, G.J. Telan, F. Malijan, H.Y. Hsu, J. Garcia, H. Fulo, and B.J. Tongol, *Nanostructured carbon-supported Pd electrocatalysts for ethanol oxidation: synthesis and characterization.* Adv. Nat. Sci.: Nanosci. Nanotechnol., 2012. **3**(Copyright (C) 2014 American Chemical Society (ACS). All Rights Reserved.): p. 045016, 5 pp.
48. Geraldes, A.N., D. Furtunato da Silva, E.S. Pino, J.C. Martins da Silva, R.F. Brambilla de Souza, P. Hammer, E.V. Spinace, A. Oliveira Neto, M. Linardi, and M. Coelho dos Santos, *Ethanol electro-oxidation in an alkaline medium using Pd/C, Au/C and PdAu/C electrocatalysts prepared by electron beam irradiation.* Electrochim. Acta, 2013. **111**(Copyright (C) 2014 American Chemical Society (ACS). All Rights Reserved.): p. 455-465.
49. Hibbitts, D.D. and M. Neurock, *Influence of oxygen and pH on the selective oxidation of ethanol on Pd catalysts.* J. Catal., 2013. **299**(Copyright (C) 2014 American Chemical Society (ACS). All Rights Reserved.): p. 261-271.
50. Hong, W., Y. Fang, J. Wang, and E. Wang, *One-step and rapid synthesis of porous Pd nanoparticles with superior catalytic activity toward ethanol/formic acid electrooxidation.* J. Power Sources, 2014. **248**(Copyright (C) 2014 American Chemical Society (ACS). All Rights Reserved.): p. 553-559.
51. Zope, B.N., D.D. Hibbitts, M. Neurock, and R.J. Davis, *Reactivity of the Gold/Water Interface During Selective Oxidation Catalysis.* Science (Washington, DC, U. S.), 2010. **330**(Copyright (C) 2014 American Chemical Society (ACS). All Rights Reserved.): p. 74-78.
52. Beyhan, S., K. Uosaki, J.M. Feliu, and E. Herrero, *Electrochemical and in situ FTIR studies of ethanol adsorption and oxidation on gold single crystal electrodes in alkaline media.* J. Electroanal. Chem., 2013. **707**(Copyright (C) 2014 American Chemical Society (ACS). All Rights Reserved.): p. 89-94.
53. Feng, Y.-Y., Z.-H. Liu, Y. Xu, P. Wang, W.-H. Wang, and D.-S. Kong, *Highly active PdAu alloy catalysts for ethanol electro-oxidation.* J. Power Sources, 2013. **232**(Copyright (C) 2014 American Chemical Society (ACS). All Rights Reserved.): p. 99-105.
54. Ding, K., Y. Wang, L. Liu, L. Liu, X. Zhang, and Z. Guo, *Hydrothermal process synthesized electrocatalytic multi-walled carbon nanotubes-inserted gold composite microparticles toward*

ethanol oxidation reaction. J. Appl. Electrochem., 2013. **43**(Copyright (C) 2014 American Chemical Society (ACS). All Rights Reserved.): p. 567-574.
55. Ksar, F., L. Ramos, B. Keita, L. Nadjo, P. Beaunier, and H. Remita, *Bimetallic Palladium-Gold Nanostructures: Application in Ethanol Oxidation.* Chem. Mater., 2009. **21**(Copyright (C) 2014 American Chemical Society (ACS). All Rights Reserved.): p. 3677-3683.
56. de Souza, J.P.I., S.L. Queiroz, K. Bergamaski, E.R. Gonzalez, and F.C. Nart, *Electro-Oxidation of Ethanol on Pt, Rh, and PtRh Electrodes. A Study Using DEMS and in-Situ FTIR Techniques.* J. Phys. Chem. B, 2002. **106**(Copyright (C) 2014 American Chemical Society (ACS). All Rights Reserved.): p. 9825-9830.
57. Santos, V.P., S.A.C. Carabineiro, P.B. Tavares, M.F.R. Pereira, J.J.M. Orfao, and J.L. Figueiredo, *Oxidation of CO, ethanol and toluene over TiO2 supported noble metal catalysts.* Appl. Catal., B, 2010. **99**(Copyright (C) 2014 American Chemical Society (ACS). All Rights Reserved.): p. 198-205.
58. Guan, Y. and E.J.M. Hensen, *Selective oxidation of ethanol to acetaldehyde by Au-Ir catalysts.* J. Catal., 2013. **305**(Copyright (C) 2014 American Chemical Society (ACS). All Rights Reserved.): p. 135-145.
59. Wang, X., G. Ma, F. Zhu, N. Lin, B. Tang, and Z. Zhang, *Preparation and characterization of micro-arc-induced Pd/TM(TM = Ni, Co and Ti) catalysts and comparison of their electrocatalytic activities toward ethanol oxidation.* Electrochim. Acta, 2013. **114**(Copyright (C) 2014 American Chemical Society (ACS). All Rights Reserved.): p. 500-508.
60. Liu, J., J. Ye, C. Xu, S.P. Jiang, and Y. Tong, *Kinetics of ethanol electrooxidation at Pd electrodeposited on Ti.* Electrochem. Commun., 2007. **9**(Copyright (C) 2014 American Chemical Society (ACS). All Rights Reserved.): p. 2334-2339.
61. Vielstich, W., V.A. Paganin, O.B. Alves, and E.G. Ciapina, *On the pathways of methanol and ethanol oxidation*, in *Handbook of Fuel Cells*. 2010, John Wiley & Sons, Ltd.
62. Brouzgou, A., S.Q. Song, and P. Tsiakaras, *Low and non-platinum electrocatalysts for PEMFCs: Current status, challenges and prospects.* Appl. Catal., B, 2012. **127**(Copyright (C) 2014 American Chemical Society (ACS). All Rights Reserved.): p. 371-388.
63. Lai, S.C.S. and M.T.M. Koper, *Electro-oxidation of ethanol and acetaldehyde on platinum single-crystal electrodes.* Faraday Discussions, 2009. **140**(0): p. 399-416.
64. Wang, Q., G.Q. Sun, L.H. Jiang, Q. Xin, S.G. Sun, Y.X. Jiang, S.P. Chen, Z. Jusys, and R.J. Behm, *Adsorption and oxidation of ethanol on colloid-based Pt/C, PtRu/C and Pt3Sn/C catalysts: In situ FTIR spectroscopy and on-line DEMS studies.* Physical Chemistry Chemical Physics, 2007. **9**(21): p. 2686-2696.
65. Lamy, C., S. Rousseau, E.M. Belgsir, C. Coutanceau, and J.M. Leger, *Recent progress in the direct ethanol fuel cell: development of new platinum-tin electrocatalysts.* Electrochimica Acta, 2004. **49**(22-23): p. 3901-3908.
66. El-Shafei, A.A. and M. Eiswirth, *Electrochemical activity of Sn-modified Pt single crystal electrodes for ethanol oxidation.* Surface Science, 2010. **604**(9-10): p. 862-867.
67. Souza, J.P.I., F.J.B. Rabelo, I.R. deMoraes, and F.C. Nart, *Performance of a co-electrodeposited Pt-Ru electrode for the electro-oxidation of ethanol studied by in situ FTIR spectroscopy.* Journal of Electroanalytical Chemistry, 1997. **420**(1-2): p. 17-20.
68. Tsiakaras, P.E., *PtM/C (M = Sn, Ru, Pd, W) based anode direct ethanol-PEMFCs: Structural characteristics and cell performance.* Journal of Power Sources, 2007. **171**(1): p. 107-112.
69. Neto, A.O., E.G. Franco, E. Arico, M. Linardi, and E.R. Gonzalez, *Electro-oxidation of methanol and ethanol on Pt-Ru/C and Pt-Ru-Mo/C electrocatalysts prepared by Bonnemann's method.* Journal of the European Ceramic Society, 2003. **23**(15): p. 2987-2992.
70. Grinberg, V.A., N.A. Mayorova, and A.A. Pasynskii, *A Cluster Pt-Sn-Catalyst for the Ethanol Direct Oxidation.* Russian Journal of Electrochemistry, 2009. **45**(12): p. 1321-1326.

71. Wang, J.T., S. Wasmus, and R.F. Savinell, *Evaluation of ethanol, 1-propanol, and 5-propanol in a direct oxidation polymer-electrolyte fuel cell - A real-time mass spectrometry study.* Journal of the Electrochemical Society, 1995. **142**(12): p. 4218-4224.
72. Neto, A.O., M.J. Giz, J. Perez, E.A. Ticianelli, and E.R. Gonzalez, *The electro-oxidation of ethanol on Pt-Ru and Pt-Mo particles supported on high-surface-area carbon.* Journal of the Electrochemical Society, 2002. **149**(3): p. A272-A279.
73. Jian, X.H., D.S. Tsai, W.H. Chung, Y.S. Huang, and F.J. Liu, *Pt-Ru and Pt-Mo electrodeposited onto Ir-IrO2 nanorods and their catalytic activities in methanol and ethanol oxidation.* Journal of Materials Chemistry, 2009. **19**(11): p. 1601-1607.
74. Zhou, W.J., Z.H. Zhou, S.Q. Song, W.Z. Li, G.Q. Sun, P. Tsiakaras, and Q. Xin, *Pt based anode catalysts for direct ethanol fuel cells.* Applied Catalysis B-Environmental, 2003. **46**(2): p. 273-285.
75. Zhou, W., Z. Zhou, S. Song, W. Li, G. Sun, P. Tsiakaras, and Q. Xin, *Pt based anode catalysts for direct ethanol fuel cells.* Appl. Catal., B, 2003. **46**(Copyright (C) 2014 American Chemical Society (ACS). All Rights Reserved.): p. 273-285.
76. Beyhan, S., J.-M. Leger, and F. Kadirgan, *Understanding the influence of Ni, Co, Rh and Pd addition to PtSn/C catalyst for the oxidation of ethanol by in situ Fourier transform infrared spectroscopy.* Appl. Catal., B, 2014. **144**(Copyright (C) 2014 American Chemical Society (ACS). All Rights Reserved.): p. 66-74.
77. Bonesi, A., G. Garaventa, W.E. Triaca, and A.M. Castro Luna, *Synthesis and characterization of new electrocatalysts for ethanol oxidation.* Int. J. Hydrogen Energy, 2008. **33**(Copyright (C) 2014 American Chemical Society (ACS). All Rights Reserved.): p. 3499-3501.
78. Spinace, E.V., A.O. Neto, T.R.R. Vasconcelos, and M. Linardi, *Electro-oxidation of ethanol using PtRu/C electrocatalysts prepared by alcohol-reduction process.* J. Power Sources, 2004. **137**(Copyright (C) 2014 American Chemical Society (ACS). All Rights Reserved.): p. 17-23.
79. Wang, H., Z. Jusys, and R.J. Behm, *Ethanol electro-oxidation on carbon-supported Pt, PtRu and Pt3Sn catalysts: A quantitative DEMS study.* J. Power Sources, 2006. **154**(Copyright (C) 2014 American Chemical Society (ACS). All Rights Reserved.): p. 351-359.
80. Samjeske, G., H.S. Wang, T. Loffler, and H. Baltruschat, *CO and methanol oxidation at Pt-electrodes modified by Mo.* Electrochimica Acta, 2002. **47**(22-23): p. 3681-3692.
81. Dos Anjos, D.M., K.B. Kokoh, J.M. Leger, A.R. De Andrade, P. Olivi, and G. Tremiliosi, *Electrocatalytic oxidation of ethanol on Pt-Mo bimetallic electrodes in acid medium.* Journal of Applied Electrochemistry, 2006. **36**(12): p. 1391-1397.
82. Ioroi, T., T. Akita, S. Yamazaki, Z. Siroma, N. Fujiwara, and K. Yasuda, *Comparative study of carbon-supported Pt/Mo-oxide and PtRu for use as CO-tolerant anode catalysts.* Electrochimica Acta, 2006. **52**(2): p. 491-498.
83. Massong, H., H.S. Wang, G. Samjeske, and H. Baltruschat, *The co-catalytic effect of Sn, Ru and Mo decorating steps of Pt(111) vicinal electrode surfaces on the oxidation of CO.* Electrochimica Acta, 2000. **46**(5): p. 701-707.
84. Mukerjee, S., R.C. Urian, S.J. Lee, E.A. Ticianelli, and J. McBreen, *Electrocatalysis of CO tolerance by carbon-supported PtMo electrocatalysts in PEMFCs.* J. Electrochem. Soc., 2004. **151**(Copyright (C) 2014 American Chemical Society (ACS). All Rights Reserved.): p. A1094-A1103.
85. Wang, Z.-B., G.-P. Yin, and Y.-G. Lin, *Synthesis and characterization of PtRuMo/C nanoparticle electrocatalyst for direct ethanol fuel cell.* J. Power Sources, 2007. **170**(Copyright (C) 2014 American Chemical Society (ACS). All Rights Reserved.): p. 242-250.
86. Watanabe, M. and S. Motoo, *Electrocatalysis by ad-atoms: Part III. Enhancement of the oxidation of carbon monoxide on platinum by ruthenium ad-atoms.* Journal of Electroanalytical Chemistry and Interfacial Electrochemistry, 1975. **60**(3): p. 275-283.

87. Koper, M.T.M., *Electrocatalysis on bimetallic and alloy surfaces.* Surf. Sci., 2004. **548**(Copyright (C) 2014 American Chemical Society (ACS). All Rights Reserved.): p. 1-3.
88. Samjeske, G., X.-Y. Xiao, and H. Baltruschat, *Ru decoration of stepped Pt single crystals and the role of the terrace width on the electrocatalytic CO oxidation.* Langmuir, 2002. **18**(Copyright (C) 2014 American Chemical Society (ACS). All Rights Reserved.): p. 4659-4666.
89. Liu, P., A. Logadottir, and J.K. Norskov, *Modeling the electro-oxidation of CO and H-2/CO on Pt, Ru, PtRu and Pt3Sn.* Electrochimica Acta, 2003. **48**(25-26): p. 3731-3742.
90. Morozan, A., B. Jousselme, and S. Palacin, *Low-platinum and platinum-free catalysts for the oxygen reduction reaction at fuel cell cathodes.* Energy & Environmental Science, 2011. **4**(4): p. 1238-1254.
91. Kim, H., K. Lee, S.I. Woo, and Y. Jung, *On the mechanism of enhanced oxygen reduction reaction in nitrogen-doped graphene nanoribbons.* Physical Chemistry Chemical Physics, 2011. **13**(39): p. 17505-17510.
92. Okamoto, Y., *First-principles molecular dynamics simulation of O2 reduction on nitrogen-doped carbon.* Applied Surface Science, 2009. **256**(1): p. 335-341.
93. Yu, L., X.L. Pan, X.M. Cao, P. Hu, and X.H. Bao, *Oxygen reduction reaction mechanism on nitrogen-doped graphene: A density functional theory study.* Journal of Catalysis, 2011. **282**(1): p. 183-190.
94. Jaouen, F., E. Proietti, M. Lefevre, R. Chenitz, J.P. Dodelet, G. Wu, H.T. Chung, C.M. Johnston, and P. Zelenay, *Recent advances in non-precious metal catalysis for oxygen-reduction reaction in polymer electrolyte fuel cells.* Energy & Environmental Science, 2011. **4**(1): p. 114-130.
95. Wang, B., *Recent development of non-platinum catalysts for oxygen reduction reaction.* Journal of Power Sources, 2005. **152**(1): p. 1-15.
96. Kannan, R., U. Bipinlal, S. Kurungot, and V.K. Pillai, *Enhanced electrocatalytic performance of functionalized carbon nanotube electrodes for oxygen reduction in proton exchange membrane fuel cells.* Physical Chemistry Chemical Physics, 2011. **13**(21): p. 10312-10317.
97. Shao, Y.Y., J.H. Sui, G.P. Yin, and Y.Z. Gao, *Nitrogen-doped carbon nanostructures and their composites as catalytic materials for proton exchange membrane fuel cell.* Applied Catalysis B-Environmental, 2008. **79**(1-2): p. 89-99.
98. Morozan, A., S. Campidelli, A. Filoramo, B. Jousselme, and S. Palacin, *Catalytic activity of cobalt and iron phthalocyanines or porphyrins supported on different carbon nanotubes towards oxygen reduction reaction.* Carbon, 2011. **49**(14): p. 4839-4847.
99. Bouwkamp-Wijnoltz, A.L., W. Visscher, and J.A.R. van Veen, *The selectivity of oxygen reduction by pyrolysed iron porphyrin supported on carbon.* Electrochimica Acta, 1998. **43**(21-22): p. 3141-3152.
100. Araki, K., S. Dovidauskas, H. Winnischofer, A.D.P. Alexiou, and H.E. Toma, *A new highly efficient tetra-electronic catalyst based on a cobalt porphyrin bound to four mu(3)-oxo-ruthenium acetate clusters.* Journal of Electroanalytical Chemistry, 2001. **498**(1-2): p. 152-160.
101. Reedy, C.J. and B.R. Gibney, *Heme protein assemblies.* Chemical Reviews, 2004. **104**(2): p. 617-649.
102. Ricard, D., M. L'Her, P. Richard, and B. Boitrel, *Iron porphyrins as models of cytochrome c oxidase.* Chemistry-a European Journal, 2001. **7**(15): p. 3291-3297.
103. Chen, Z.W., D. Higgins, A.P. Yu, L. Zhang, and J.J. Zhang, *A review on non-precious metal electrocatalysts for PEM fuel cells.* Energy & Environmental Science, 2011. **4**(9): p. 3167-3192.
104. Decreau, R.A., J.P. Collman, and A. Hosseini, *Electrochemical applications. How click chemistry brought biomimetic models to the next level: electrocatalysis under controlled rate of electron transfer.* Chem. Soc. Rev., 2010. **39**(Copyright (C) 2014 American Chemical Society (ACS). All Rights Reserved.): p. 1291-1301.

105. Jahnke, H., M. Schoenborn, and G. Zimmermann, *Organic dyes as catalysts for fuel cells.* Top. Curr. Chem., 1976. **61**(Copyright (C) 2014 American Chemical Society (ACS). All Rights Reserved.): p. 133-81.
106. Jasinski, R.J., *New fuel cell cathode catalyst.* Nature (London, U. K.), 1964. **201**(Copyright (C) 2014 American Chemical Society (ACS). All Rights Reserved.): p. 1212-13.
107. Matter, P.H. and U.S. Ozkan, *Non-metal catalysts for dioxygen reduction in an acidic electrolyte.* Catalysis Letters, 2006. **109**(3-4): p. 115-123.
108. Ikeda, T., M. Boero, S.F. Huang, K. Terakura, M. Oshima, and J. Ozaki, *Carbon alloy catalysts: Active sites for oxygen reduction reaction.* Journal of Physical Chemistry C, 2008. **112**(38): p. 14706-14709.
109. Gong, K., F. Du, Z. Xia, M. Durstock, and L. Dai, *Nitrogen-Doped Carbon Nanotube Arrays with High Electrocatalytic Activity for Oxygen Reduction.* Science (Washington, DC, U. S.), 2009. **323**(Copyright (C) 2013 American Chemical Society (ACS). All Rights Reserved.): p. 760-764.
110. Qu, L., Y. Liu, J.-B. Baek, and L. Dai, *Nitrogen-Doped Graphene as Efficient Metal-Free Electrocatalyst for Oxygen Reduction in Fuel Cells.* ACS Nano, 2010. **4**(Copyright (C) 2014 American Chemical Society (ACS). All Rights Reserved.): p. 1321-1326.
111. Hohenberg, P. and W. Kohn, *Inhomogeneous Electron Gas.* Physical Review, 1964. **136**(3B): p. B864-B871.
112. Kohn, W. and L.J. Sham, *Self-Consistent Equations Including Exchange and Correlation Effects.* Physical Review, 1965. **140**(4A): p. A1133-A1138.
113. Payne, M.C., M.P. Teter, D.C. Allan, T.A. Arias, and J.D. Joannopoulos, *Iterative Minimization Techniques for Abinitio Total-Energy Calculations - Molecular-Dynamics and Conjugate Gradients.* Reviews of Modern Physics, 1992. **64**(4): p. 1045-1097.
114. Kresse, G. and J. Furthmuller, *Efficiency of ab-initio total energy calculations for metals and semiconductors using a plane-wave basis set.* Computational Materials Science, 1996. **6**(1): p. 15-50.
115. Furthmuller, J., J. Hafner, and G. Kresse, *Dimer reconstruction and electronic surface states on clean and hydrogenated diamond (100) surfaces.* Physical Review B, 1996. **53**(11): p. 7334-7351.
116. Kresse, G. and J. Hafner, *Abinitio Molecular-Dynamics for Liquid-Metals.* Physical Review B, 1993. **47**(1): p. 558-561.
117. Perdew, J.P., J.A. Chevary, S.H. Vosko, K.A. Jackson, M.R. Pederson, D.J. Singh, and C. Fiolhais, *Atoms, molecules, solids, and surfaces: Applications of the generalized gradient approximation for exchange and correlation.* Physical Review B, 1992. **46**(11): p. 6671-6687.
118. Kresse, G. and D. Joubert, *From ultrasoft pseudopotentials to the projector augmented-wave method.* Physical Review B, 1999. **59**(3): p. 1758-1775.
119. Norskov, J.K., J. Rossmeisl, A. Logadottir, L. Lindqvist, J.R. Kitchin, T. Bligaard, and H. Jonsson, *Origin of the overpotential for oxygen reduction at a fuel-cell cathode.* Journal of Physical Chemistry B, 2004. **108**(46): p. 17886-17892.
120. Gewirth, A.A. and M.S. Thorum, *Electroreduction of Dioxygen for Fuel-Cell Applications: Materials and Challenges.* Inorganic Chemistry, 2010. **49**(8): p. 3557-3566.
121. Jayasayee, K., J.A.R.V. Veen, T.G. Manivasagam, S. Celebi, E.J.M. Hensen, and F.A. de Bruijn, *Oxygen reduction reaction (ORR) activity and durability of carbon supported PtM (Co, Ni, Cu) alloys: Influence of particle size and non-noble metals.* Applied Catalysis B: Environmental, 2012. **111–112**(0): p. 515-526.
122. Geng, D.S., H. Liu, Y.G. Chen, R.Y. Li, X.L. Sun, S.Y. Ye, and S. Knights, *Non-noble metal oxygen reduction electrocatalysts based on carbon nanotubes with controlled nitrogen contents.* Journal of Power Sources, 2011. **196**(4): p. 1795-1801.

123. Ma, G.X., R.R. Jia, J.H. Zhao, Z.J. Wang, C. Song, S.P. Jia, and Z.P. Zhu, *Nitrogen-Doped Hollow Carbon Nanoparticles with Excellent Oxygen Reduction Performances and Their Electrocatalytic Kinetics.* Journal of Physical Chemistry C, 2011. **115**(50): p. 25148-25154.
124. Biddinger, E.J., D. von Deak, and U.S. Ozkan, *Nitrogen-Containing Carbon Nanostructures as Oxygen-Reduction Catalysts.* Topics in Catalysis, 2009. **52**(11): p. 1566-1574.
125. Koslowski, U.I., I. Abs-Wurmbach, S. Fiechter, and P. Bogdanoff, *Nature of the Catalytic Centers of Porphyrin-Based Electrocatalysts for the ORR: A Correlation of Kinetic Current Density with the Site Density of Fe-N4 Centers.* J. Phys. Chem. C, 2008. **112**(Copyright (C) 2014 American Chemical Society (ACS). All Rights Reserved.): p. 15356-15366.
126. Maruyama, J., J. Okamura, K. Miyazaki, Y. Uchimoto, and I. Abe, *Hemoglobin Pyropolymer Used as a Precursor of a Noble-Metal-Free Fuel Cell Cathode Catalyst.* J. Phys. Chem. C, 2008. **112**(Copyright (C) 2014 American Chemical Society (ACS). All Rights Reserved.): p. 2784-2790.
127. Ziegelbauer, J.M., T.S. Olson, S. Pylypenko, F. Alamgir, C. Jaye, P. Atanassov, and S. Mukerjee, *Direct Spectroscopic Observation of the Structural Origin of Peroxide Generation from Co-Based Pyrolyzed Porphyrins for ORR Applications.* J. Phys. Chem. C, 2008. **112**(Copyright (C) 2014 American Chemical Society (ACS). All Rights Reserved.): p. 8839-8849.
128. Gupta, S., D. Tryk, I. Bae, W. Aldred, and E. Yeager, *Heat-treated polyacrylonitrile-based catalysts for oxygen electroreduction.* J. Appl. Electrochem., 1989. **19**(Copyright (C) 2012 American Chemical Society (ACS). All Rights Reserved.): p. 19-27.
129. Yang, J.B., D.J. Liu, N.N. Kariuki, and L.X. Chen, *Aligned carbon nanotubes with built-in FeN4 active sites for electrocatalytic reduction of oxygen.* Chemical Communications, 2008(3): p. 329-331.
130. Liu, D.J., J. Yang, and D.J. Gosztola, *Investigation of aligned carbon nanotubes as a novel catalytic electrodes for PEM fuel cells.* ECS Trans., 2007. **5**(1): p. 7.
131. Lefevre, M., E. Proietti, F. Jaouen, and J.P. Dodelet, *Iron-Based Catalysts with Improved Oxygen Reduction Activity in Polymer Electrolyte Fuel Cells.* Science, 2009. **324**(5923): p. 71-74.
132. Barazzouk, S., M. Lefevre, and J.P. Dodelet, *Oxygen Reduction in PEM Fuel Cells: Fe-Based Electrocatalysts Made with High Surface Area Activated Carbon Supports.* Journal of the Electrochemical Society, 2009. **156**(12): p. B1466-B1474.
133. Charreteur, F., F. Jaouen, and J.P. Dodelet, *Iron porphyrin-based cathode catalysts for PEM fuel cells: Influence of pyrolysis gas on activity and stability.* Electrochimica Acta, 2009. **54**(26): p. 6622-6630.
134. Lefevre, M., J.P. Dodelet, and P. Bertrand, *Molecular oxygen reduction in PEM fuel cell conditions: ToF-SIMS analysis of Co-based electrocatalysts.* Journal of Physical Chemistry B, 2005. **109**(35): p. 16718-16724.
135. Wu, G., K.L. More, C.M. Johnston, and P. Zelenay, *High-Performance Electrocatalysts for Oxygen Reduction Derived from Polyaniline, Iron, and Cobalt.* Science, 2011. **332**(6028): p. 443-447.
136. Wu, G., C.M. Johnston, N.H. Mack, K. Artyushkova, M. Ferrandon, M. Nelson, J.S. Lezama-Pacheco, S.D. Conradson, K.L. More, D.J. Myers, and P. Zelenay, *Synthesis-structure-performance correlation for polyaniline-Me-C non-precious metal cathode catalysts for oxygen reduction in fuel cells.* Journal of Materials Chemistry, 2011. **21**(30): p. 11392-11405.
137. Wu, G., K. Artyushkova, M. Ferrandon, J. Kropf, D. Myers, and P. Zelenay, *Performance durability of polyaniline-derived non-precious cathode catalysts.* ECS Trans., 2009. **25**(Copyright (C) 2014 American Chemical Society (ACS). All Rights Reserved.): p. 1299-1311.
138. Lefèvre, M., J.P. Dodelet, and P. Bertrand, *O2 Reduction in PEM Fuel Cells: Activity and Active Site Structural Information for Catalysts Obtained by the Pyrolysis at High Temperature of Fe Precursors.* The Journal of Physical Chemistry B, 2000. **104**(47): p. 11238-11247.

139. Lefèvre, M., J.P. Dodelet, and P. Bertrand, *Molecular Oxygen Reduction in PEM Fuel Cells: Evidence for the Simultaneous Presence of Two Active Sites in Fe-Based Catalysts.* The Journal of Physical Chemistry B, 2002. **106**(34): p. 8705-8713.
140. Kramm, U.I., J. Herranz, N. Larouche, T.M. Arruda, M. Lefevre, F. Jaouen, P. Bogdanoff, S. Fiechter, I. Abs-Wurmbach, S. Mukerjee, and J.-P. Dodelet, *Structure of the catalytic sites in Fe/N/C-catalysts for O2-reduction in PEM fuel cells.* Physical Chemistry Chemical Physics, 2012. **14**(33): p. 11673-11688.
141. Chang, C.J., L.L. Chng, and D.G. Nocera, *Proton-coupled O-O activation on a redox platform bearing a hydrogen-bonding scaffold.* Journal of the American Chemical Society, 2003. **125**(7): p. 1866-1876.
142. Sawaguchi, T., T. Matsue, K. Itaya, and I. Uchida, *Electrochemical catalytic reduction of molecular oxygen by iron porphyrin ion-complex modified electrode.* Electrochimica Acta, 1991. **36**(3–4): p. 703-708.
143. Sawaguchi, T., T. Matsue, K. Itaya, and I. Uchida, *Electrochemical Catalytic Reduction of Molecular-Oxygen by Iron Porphyrin Ion-Complex Modified Electrode.* Electrochimica Acta, 1991. **36**(3-4): p. 703-708.
144. Song, E., C. Shi, and F.C. Anson, *Comparison of the Behavior of Several Cobalt Porphyrins as Electrocatalysts for the Reduction of O2 at Graphite Electrodes.* Langmuir, 1998. **14**(15): p. 4315-4321.
145. D'Souza, F., Y.-Y. Hsieh, and G.R. Deviprasad, *Electrocatalytic reduction of molecular oxygen using non-planar cobalt tetrakis(4-sulfonatophenyl)-β-octabromoporphyrin.* J. Electroanal. Chem., 1997. **426**(Copyright (C) 2014 American Chemical Society (ACS). All Rights Reserved.): p. 17-21.
146. Fukuzumi, S., K. Okamoto, Y. Tokuda, C.P. Gros, and R. Guilard, *Dehydrogenation versus Oxygenation in Two-Electron and Four-Electron Reduction of Dioxygen by 9-Alkyl-10-methyl-9,10-dihydroacridines Catalyzed by Monomeric Cobalt Porphyrins and Cofacial Dicobalt Porphyrins in the Presence of Perchloric Acid.* J. Am. Chem. Soc., 2004. **126**(Copyright (C) 2014 American Chemical Society (ACS). All Rights Reserved.): p. 17059-17066.
147. Song, E.H., C.N. Shi, and F.C. Anson, *Comparison of the behavior of several cobalt porphyrins as electrocatalysts for the reduction of O-2 at graphite electrodes.* Langmuir, 1998. **14**(15): p. 4315-4321.
148. Winnischofer, H., V.Y. Otake, S. Dovidauskas, M. Nakamura, H.E. Toma, and K. Araki, *Supramolecular tetracluster-cobalt porphyrin: a four-electron transfer catalyst for dioxygen reduction.* Electrochimica Acta, 2004. **49**(22-23): p. 3711-3718.
149. Collman, J.P., P. Denisevich, Y. Konai, M. Marrocco, C. Koval, and F.C. Anson, *Electrode Catalysis of the 4-Electron Reduction of Oxygen to Water by Dicobalt Face-to-Face Porphyrins.* Journal of the American Chemical Society, 1980. **102**(19): p. 6027-6036.
150. Chang, C.J., Y.Q. Deng, C.N. Shi, C.K. Chang, F.C. Anson, and D.G. Nocera, *Electrocatalytic four-electron reduction of oxygen to water by a highly flexible cofacial cobalt bisporphyrin.* Chemical Communications, 2000(15): p. 1355-1356.
151. Chang, C.J., Z.H. Loh, C.N. Shi, F.C. Anson, and D.G. Nocera, *Targeted proton delivery in the catalyzed reduction of oxygen to water by bimetallic Pacman porphyrins.* Journal of the American Chemical Society, 2004. **126**(32): p. 10013-10020.
152. Collman, J.P., R.A. Decréau, Y. Yan, J. Yoon, and E.I. Solomon, *Intramolecular Single-Turnover Reaction in a Cytochrome c Oxidase Model Bearing a Tyr244 Mimic.* Journal of the American Chemical Society, 2007. **129**(18): p. 5794-5795.

153. Wang, G.F., N. Ramesh, A. Hsu, D. Chu, and R.R. Chen, *Density functional theory study of the adsorption of oxygen molecule on iron phthalocyanine and cobalt phthalocyanine.* Molecular Simulation, 2008. **34**(10-15): p. 1051-1056.
154. Zagal, J.H., *Metallophthalocyanines as catalysts in electrochemical reactions.* Coordination Chemistry Reviews, 1992. **119**(0): p. 89-136.
155. Kuehn, F.E., A.M. Santos, P.W. Roesky, E. Herdtweck, W. Scherer, P. Gisdakis, I.V. Yudanov, C. Di Valentin, and N. Rosch, *Trigonal-bipyramidal Lewis base adducts of methyltrioxorhenium(VII) and their bisperoxo congeners: characterization, application in catalytic epoxidation, and density functional mechanistic study.* Chem. - Eur. J., 1999. **5**(Copyright (C) 2014 American Chemical Society (ACS). All Rights Reserved.): p. 3603-3615.
156. Di Valentin, C., P. Gisdakis, I.V. Yudanov, and N. Roesch, *Olefin Epoxidation by Peroxo Complexes of Cr, Mo and W. A Comparative Density Functional Study.* J. Org. Chem., 2000. **65**(Copyright (C) 2014 American Chemical Society (ACS). All Rights Reserved.): p. 2996-3004.
157. Deubel, D.V., *Are peroxyformic acid and dioxirane electrophilic or nucleophilic oxidants?* Journal of Organic Chemistry, 2001. **66**(11): p. 3790-3796.
158. Di Valentin, C., P. Gisdakis, I.V. Yudanov, and N. Rosch, *Olefin epoxidation by peroxo complexes of Cr, Mo, and W. A comparative density functional study.* Journal of Organic Chemistry, 2000. **65**(10): p. 2996-3004.
159. Ricard, D., M. L'Her, P. Richard, and B. Boitrel, *Iron porphyrins as models of cytochrome c oxidase.* Chemistry, 2001. **7**(15): p. 3291-7.
160. Gojkovic, S.L., S. Gupta, and R.F. Savinell, *Heat-treated iron(III) tetramethoxyphenyl porphyrin supported on high-area carbon as an electrocatalyst for oxygen reduction - I. Characterization of the electrocatalyst.* Journal of the Electrochemical Society, 1998. **145**(10): p. 3493-3499.
161. Gojkovic, S.L., S. Gupta, and R.F. Savinell, *Heat-treated iron(III) tetramethoxyphenylporphyrin chloride supported on high-area carbon as an electrocatalyst for oxygen reduction: Part III. Detection of hydrogen-peroxide during oxygen reduction.* Electrochim. Acta, 1999. **45**(6): p. 889-897.
162. Gupta, S., D. Tryk, I. Bae, W. Aldred, and E. Yeager, *Heat-Treated Polyacrylonitrile-Based Catalysts for Oxygen Electroreduction.* Journal of Applied Electrochemistry, 1989. **19**(1): p. 19-27.
163. Maldonado, S. and K.J. Stevenson, *Influence of Nitrogen Doping on Oxygen Reduction Electrocatalysis at Carbon Nanofiber Electrodes.* J. Phys. Chem. B, 2005. **109**(Copyright (C) 2014 American Chemical Society (ACS). All Rights Reserved.): p. 4707-4716.
164. Geng, D., Y. Chen, Y. Chen, Y. Li, R. Li, X. Sun, S. Ye, and S. Knights, *High oxygen-reduction activity and durability of nitrogen-doped graphene.* Energy & Environmental Science, 2011. **4**(3): p. 760-764.
165. Matter, P.H., E. Wang, M. Arias, E.J. Biddinger, and U.S. Ozkan, *Oxygen Reduction Reaction Catalysts Prepared from Acetonitrile Pyrolysis over Alumina-Supported Metal Particles.* The Journal of Physical Chemistry B, 2006. **110**(37): p. 18374-18384.
166. Shao, Y., J. Sui, G. Yin, and Y. Gao, *Nitrogen-doped carbon nanostructures and their composites as catalytic materials for proton exchange membrane fuel cell.* Applied Catalysis B: Environmental, 2008. **79**(1): p. 89-99.
167. Chen, Z., D. Higgins, and Z. Chen, *Nitrogen doped carbon nanotubes and their impact on the oxygen reduction reaction in fuel cells.* Carbon, 2010. **48**(Copyright (C) 2014 American Chemical Society (ACS). All Rights Reserved.): p. 3057-3065.
168. Liang, J., Y. Jiao, M. Jaroniec, and S.Z. Qiao, *Sulfur and Nitrogen Dual-Doped Mesoporous Graphene Electrocatalyst for Oxygen Reduction with Synergistically Enhanced Performance.* Angew. Chem., Int. Ed., 2012. **51**(Copyright (C) 2014 American Chemical Society (ACS). All Rights Reserved.): p. 11496-11500.

169. Jaouen, F. and J.P. Dodelet, *Average turn-over frequency of O-2 electro-reduction for Fe/N/C and Co/N/C catalysts in PEFCs.* Electrochimica Acta, 2007. **52**(19): p. 5975-5984.
170. Nallathambi, V., J.W. Lee, S.P. Kumaraguru, G. Wu, and B.N. Popov, *Development of high performance carbon composite catalyst for oxygen reduction reaction in PEM Proton Exchange Membrane fuel cells.* Journal of Power Sources, 2008. **183**(1): p. 34-42.
171. Rao, C.V., C.R. Cabrera, and Y. Ishikawa, *In Search of the Active Site in Nitrogen-Doped Carbon Nanotube Electrodes for the Oxygen Reduction Reaction.* Journal of Physical Chemistry Letters, 2010. **1**(18): p. 2622-2627.
172. Maldonado, S., S. Morin, and K.J. Stevenson, *Structure, composition, and chemical reactivity of carbon nanotubes by selective nitrogen doping.* Carbon, 2006. **44**(Copyright (C) 2014 American Chemical Society (ACS). All Rights Reserved.): p. 1429-1437.
173. Kundu, S., T.C. Nagaiah, W. Xia, Y. Wang, S. Van Dommele, J.H. Bitter, M. Santa, G. Grundmeier, M. Bron, W. Schuhmann, and M. Muhler, *Electrocatalytic Activity and Stability of Nitrogen-Containing Carbon Nanotubes in the Oxygen Reduction Reaction.* J. Phys. Chem. C, 2009. **113**(Copyright (C) 2014 American Chemical Society (ACS). All Rights Reserved.): p. 14302-14310.
174. Deng, D., X. Pan, L. Yu, Y. Cui, Y. Jiang, J. Qi, W.-X. Li, Q. Fu, X. Ma, Q. Xue, G. Sun, and X. Bao, *Toward N-Doped Graphene via Solvothermal Synthesis.* Chem. Mater., 2011. **23**(Copyright (C) 2014 American Chemical Society (ACS). All Rights Reserved.): p. 1188-1193.
175. Zheng, B., J. Wang, F.B. Wang, and X.H. Xia, *Synthesis of nitrogen doped graphene with high electrocatalytic activity toward oxygen reduction reaction.* Electrochemistry Communications, 2013. **28**: p. 24-26.
176. Wang, H., T. Maiyalagan, and X. Wang, *Review on Recent Progress in Nitrogen-Doped Graphene: Synthesis, Characterization, and Its Potential Applications.* ACS Catalysis, 2012. **2**(5): p. 781-794.
177. Niwa, H., K. Horiba, Y. Harada, M. Oshima, T. Ikeda, K. Terakura, J. Ozaki, and S. Miyata, *X-ray absorption analysis of nitrogen contribution to oxygen reduction reaction in carbon alloy cathode catalysts for polymer electrolyte fuel cells.* Journal of Power Sources, 2009. **187**(1): p. 93-97.
178. Matter, P.H., L. Zhang, and U.S. Ozkan, *The role of nanostructure in nitrogen-containing carbon catalysts for the oxygen reduction reaction.* J. Catal., 2006. **239**(Copyright (C) 2014 American Chemical Society (ACS). All Rights Reserved.): p. 83-96.
179. Matter, P.H., E. Wang, M. Arias, E.J. Biddinger, and U.S. Ozkan, *Oxygen reduction reaction activity and surface properties of nanostructured nitrogen-containing carbon.* J. Mol. Catal. A: Chem., 2007. **264**(Copyright (C) 2014 American Chemical Society (ACS). All Rights Reserved.): p. 73-81.
180. Iwazaki, T., H. Yang, R. Obinata, W. Sugimoto, and Y. Takasu, *Oxygen-reduction activity of silk-derived carbons.* J. Power Sources, 2010. **195**(Copyright (C) 2014 American Chemical Society (ACS). All Rights Reserved.): p. 5840-5847.
181. Lv, R., Q. Li, A.R. Botello-Mendez, T. Hayashi, B. Wang, A. Berkdemir, Q. Hao, A.L. Elias, R. Cruz-Silva, H.R. Gutierrez, Y.A. Kim, H. Muramatsu, J. Zhu, M. Endo, H. Terrones, J.C. Charlier, M. Pan, and M. Terrones, *Nitrogen-doped graphene: beyond single substitution and enhanced molecular sensing.* Sci Rep, 2012. **2**: p. 586.
182. Matzner, S. and H.P. Boehm, *Influence of nitrogen doping on the adsorption and reduction of nitric oxide by activated carbons.* Carbon, 1998. **36**(Copyright (C) 2014 American Chemical Society (ACS). All Rights Reserved.): p. 1697-1700.
183. Huang, M.-C. and H. Teng, *Nitrogen-containing carbons from phenol-formaldehyde resins and their catalytic activity in NO reduction with NH3.* Carbon, 2003. **41**(Copyright (C) 2014 American Chemical Society (ACS). All Rights Reserved.): p. 951-957.

184. Biniak, S., M. Walczyk, and G.S. Szymanski, *Modified porous carbon materials as catalytic support for cathodic reduction of dioxygen.* Fuel Process. Technol., 2002. **79**(Copyright (C) 2014 American Chemical Society (ACS). All Rights Reserved.): p. 251-257.
185. Zhang, L. and Z. Xia, *Mechanisms of Oxygen Reduction Reaction on Nitrogen-Doped Graphene for Fuel Cells.* J. Phys. Chem. C, 2011. **115**(Copyright (C) 2014 American Chemical Society (ACS). All Rights Reserved.): p. 11170-11176.
186. Quaino, P., N.B. Luque, R. Nazmutdinov, E. Santos, and W. Schmickler, *Why is gold such a good catalyst for oxygen reduction in alkaline media?* Angew. Chem., Int. Ed., 2012. **51**(Copyright (C) 2014 American Chemical Society (ACS). All Rights Reserved.): p. 12997-13000.
187. Spendelow, J.S. and A. Wieckowski, *Electrocatalysis of oxygen reduction and small alcohol oxidation in alkaline media.* Phys. Chem. Chem. Phys., 2007. **9**(Copyright (C) 2014 American Chemical Society (ACS). All Rights Reserved.): p. 2654-2675.
188. Xu, X., S. Jiang, Z. Hu, and S. Liu, *Nitrogen-Doped Carbon Nanotubes: High Electrocatalytic Activity toward the Oxidation of Hydrogen Peroxide and Its Application for Biosensing.* ACS Nano, 2010. **4**(Copyright (C) 2014 American Chemical Society (ACS). All Rights Reserved.): p. 4292-4298.
189. Wang, Y.-J., J. Qiao, R. Baker, and J. Zhang, *Alkaline polymer electrolyte membranes for fuel cell applications.* Chem. Soc. Rev., 2013. **42**(Copyright (C) 2014 American Chemical Society (ACS). All Rights Reserved.): p. 5768-5787.
190. Xu, J., W. Huang, and R.L. McCreery, *Isotope and surface preparation effects on alkaline dioxygen reduction at carbon electrodes.* J. Electroanal. Chem., 1996. **410**(Copyright (C) 2014 American Chemical Society (ACS). All Rights Reserved.): p. 235-242.
191. Yeager, E., *Electrocatalysts for molecular oxygen reduction.* Electrochim. Acta, 1984. **29**(Copyright (C) 2014 American Chemical Society (ACS). All Rights Reserved.): p. 1527-37.
192. Wei, W., H. Liang, K. Parvez, X. Zhuang, X. Feng, and K. Muellen, *Nitrogen-Doped Carbon Nanosheets with Size-Defined Mesopores as Highly Efficient Metal-Free Catalyst for the Oxygen Reduction Reaction.* Angew. Chem., Int. Ed., 2014. **53**(Copyright (C) 2014 American Chemical Society (ACS). All Rights Reserved.): p. 1570-1574.
193. Bidault, F., D.J.L. Brett, P.H. Middleton, and N.P. Brandon, *Review of gas diffusion cathodes for alkaline fuel cells.* J. Power Sources, 2009. **187**(1): p. 39-48.
194. Li, X., B.N. Popov, T. Kawahara, and H. Yanagi, *Recent advances in non-precious metal catalysts for oxygen reduction reaction in fuel cells.* ECS Trans., 2010. **33**(1, Polymer Electrolyte Fuel Cells 10): p. 1769-1776.
195. Iwasita, T. and E. Pastor, *A Dems and Ftir Spectroscopic Investigation of Adsorbed Ethanol on Polycrystalline Platinum.* Electrochimica Acta, 1994. **39**(4): p. 531-537.
196. Camara, G.A. and T. Iwasita, *Parallel pathways of ethanol oxidation: The effect of ethanol concentration.* Journal of Electroanalytical Chemistry, 2005. **578**(2): p. 315-321.
197. Kokoh, K.B., F. Hahn, E.M. Belgsir, C. Lamy, A.R. de Andrade, P. Olivi, A.J. Motheo, and G. Tremiliosi-Filho, *Electrocatalytic oxidation of acetaldehyde on Pt alloy electrodes.* Electrochimica Acta, 2004. **49**(13): p. 2077-2083.
198. Stoltze, P., *Microkinetic simulation of catalytic reactions.* Prog. Surf. Sci., 2000. **65**(Copyright (C) 2014 American Chemical Society (ACS). All Rights Reserved.): p. 65-150.
199. Mei, D., P.A. Sheth, M. Neurock, and C.M. Smith, *First-principles-based kinetic Monte Carlo simulation of the selective hydrogenation of acetylene over Pd(111).* J. Catal., 2006. **242**(Copyright (C) 2014 American Chemical Society (ACS). All Rights Reserved.): p. 1-15.
200. Mei, D., M. Neurock, and C.M. Smith, *Hydrogenation of acetylene-ethylene mixtures over Pd and Pd-Ag alloys: First-principles-based kinetic Monte Carlo simulations.* J. Catal., 2009. **268**(Copyright (C) 2014 American Chemical Society (ACS). All Rights Reserved.): p. 181-195.

201. Cortright, R.D. and J.A. Dumesic, *Kinetics of heterogeneous catalytic reactions: Analysis of reaction schemes.* Adv. Catal., 2001. **46**(Copyright (C) 2014 American Chemical Society (ACS). All Rights Reserved.): p. 161-264.
202. Ovesen, C.V., B.S. Clausen, B.S. Hammershoei, G. Steffensen, T. Askgaard, I. Chorkendorff, J.K. Noerskov, P.B. Rasmussen, P. Stoltze, and P. Taylor, *A microkinetic analysis of the water-gas shift reaction under industrial conditions.* J. Catal., 1996. **158**(Copyright (C) 2014 American Chemical Society (ACS). All Rights Reserved.): p. 170-80.
203. Rubert-Nason, P., M. Mavrikakis, C.T. Maravelias, L.C. Grabow, and L.T. Biegler, *Advanced solution methods for microkinetic models of catalytic reactions: A methanol synthesis case study.* AIChE J., 2014(Copyright (C) 2014 American Chemical Society (ACS). All Rights Reserved.): p. Ahead of Print.
204. Wang, C.-C., J.-Y. Wu, T.L.M. Pham, and J.-C. Jiang, *Microkinetic Simulation of Ammonia Oxidation on the RuO2(110) Surface.* ACS Catal., 2014. **4**(Copyright (C) 2014 American Chemical Society (ACS). All Rights Reserved.): p. 639-648.
205. Bengaard, H.S., J.K. Norskov, J. Sehested, B.S. Clausen, L.P. Nielsen, A.M. Molenbroek, and J.R. Rostrup-Nielsen, *Steam Reforming and Graphite Formation on Ni Catalysts.* J. Catal., 2002. **209**(Copyright (C) 2014 American Chemical Society (ACS). All Rights Reserved.): p. 365-384.
206. Hansen, E. and M. Neurock, *First-principles based kinetic simulations of acetic acid temperature programmed reaction on Pd(111).* J. Phys. Chem. B, 2001. **105**(Copyright (C) 2014 American Chemical Society (ACS). All Rights Reserved.): p. 9218-9229.
207. Hansen, E.W. and M. Neurock, *First-Principles-Based Monte Carlo Simulation of Ethylene Hydrogenation Kinetics on Pd.* J. Catal., 2000. **196**(Copyright (C) 2014 American Chemical Society (ACS). All Rights Reserved.): p. 241-252.
208. Mei, D., E.W. Hansen, and M. Neurock, *Ethylene Hydrogenation over Bimetallic Pd/Au(III) Surfaces: Application of Quantum Chemical Results and Dynamic Monte Carlo Simulation.* J. Phys. Chem. B, 2003. **107**(Copyright (C) 2014 American Chemical Society (ACS). All Rights Reserved.): p. 798-810.
209. Kieken, L.D., M. Neurock, and D. Mei, *Screening by Kinetic Monte Carlo Simulation of Pt-Au(100) Surfaces for the Steady-State Decomposition of Nitric Oxide in Excess Dioxygen.* J. Phys. Chem. B, 2005. **109**(Copyright (C) 2014 American Chemical Society (ACS). All Rights Reserved.): p. 2234-2244.
210. Davies, J.C., B.E. Hayden, D.J. Pegg, and M.E. Rendall, *The electro-oxidation of carbon monoxide on ruthenium modified Pt(111).* Surf. Sci., 2002. **496**(Copyright (C) 2014 American Chemical Society (ACS). All Rights Reserved.): p. 110-120.
211. Stamenkovic, V.R., M. Arenz, C.A. Lucas, M.E. Gallagher, P.N. Ross, and N.M. Markovic, *Surface chemistry on bimetallic alloy surfaces: adsorption of anions and oxidation of CO on Pt3Sn(111).* J. Am. Chem. Soc., 2003. **125**(Copyright (C) 2014 American Chemical Society (ACS). All Rights Reserved.): p. 2736-2745.

Appendix A

Complete acetaldehyde dehydrogenation pathways on both Pt (111) and Pt-Mo surfaces:

Dehydrogenation steps (Pt(111))	Activation barrier E_a (eV)	Reaction Energy ΔE_{rxn} (eV)
$CH_3CHO^* \rightarrow CH_2CHO^* + H^*$	1.09	0.04
$CH_3CHO^* \rightarrow CH_3CO^* + H^*$	0.29	-0.50
$CH_2CHO^* \rightarrow CHCHO^* + H^*$	0.74	0.02
$CH_2CHO^* \rightarrow CH_2CO^* + H^*$	0.36	-0.60
$CH_3CO^* \rightarrow CH_2CO^* + H^*$	0.89	-0.06
$CH_2CO^* \rightarrow CHCO^* + H^*$	0.94	0.11
$CHCHO^* \rightarrow CHCO^* + H^*$	0.51	-0.51

Table A.1. All dehydrogenation paths of acetaldehyde on Pt(111) surface.

Dehydrogenation steps (Pt-Mo)	Activation barrier E_a (eV)	Reaction Energy ΔE_{rxn} (eV)
$CH_3CHO^* \rightarrow CH_2CHO^* + H^*$	1.14	-0.15
$CH_3CHO^* \rightarrow CH_3CO^* + H^*$	0.54	-0.32

$CH_2CHO^* \rightarrow CHCHO^* + H^*$	1.00	0.17
$CH_2CHO^* \rightarrow CH_2CO^* + H^*$	0.81	0.01
$CH_3CO^* \rightarrow CH_2CO^* + H^*$	1.23	0.18
$CH_2CO^* \rightarrow CHCO^* + H^*$	1.07	0.33
$CHCHO^* \rightarrow CHCO^* + H^*$	1.11	0.17

Table A.2. All dehydrogenation paths of acetaldehyde on Pt-Mo surface.

Complete C-C bond activation pathways for all possible C2 species on Pt(111) and Pt-Mo surfaces:

C-C activation steps (Pt(111))	Activation barrier E_a (eV)	Reaction Energy ΔE_{rxn} (eV)
$CH_3CHO^* \rightarrow CH_3^* + CHO^*$	1.55	-0.22
$CH_2CHO^* \rightarrow CH_2^* + CHO^*$	1.16	-0.02
$CH_3CO^* \rightarrow CH_3^* + CO^*$	1.30	-0.50
$CH_2CO^* \rightarrow CH_2^* + CO^*$	1.20	-0.05
$CHCHO^* \rightarrow CH^* + CHO^*$	1.02	-0.47
$CHCO^* \rightarrow CH^* + CO^*$	0.92	-0.58

Table A.3. All C-C bond activation paths for C2 species on Pt(111) surface.

C-C activation steps (Pt-Mo)	Activation barrier E_a (eV)	Reaction Energy ΔE_{rxn} (eV)
CH_3CHO^* --> CH_3^* + CHO^*	1.78	0.06
CH_2CHO^* --> CH_2^* + CHO^*	1.60	0.08
CH_3CO^* --> CH_3^* + CO^*	1.54	0.26
CH_2CO^* --> CH_2^* + CO^*	1.24	-0.06
$CHCHO^*$ --> CH^* + CHO^*	0.89	-0.32
$CHCO^*$ --> CH^* + CO^*	0.47	-0.62

Table A.4. All C-C bond activation paths for C2 species on Pt-Mo surface.

Appendix B

Microkinetic model regarding the dehydrogenation processes starting from acetaldehyde together with the C-C bond activation processes for all intermediate C2 species on both Pt(111) and Pt-Mo surfaces is shown in Fig. B.1:

Pt (111)	Pt-Mo
$CH_3CHO(g) + * \underset{k_2}{\overset{k_1}{\rightleftharpoons}} CH_3CHO*$	$CH_3CHO(g) + Mo* \underset{k_2}{\overset{k_1}{\rightleftharpoons}} CH_3CHO*$
$CH_3CHO* + * \underset{k_4}{\overset{k_3}{\rightleftharpoons}} CH_3CO* + H*$	$CH_3CHO* + Pt* \underset{k_4}{\overset{k_3}{\rightleftharpoons}} CH_3CO* + H*$
$CH_3CO* + * \underset{k_6}{\overset{k_5}{\rightleftharpoons}} CH_3* + CO*$	$CH_3CO* + Pt* \underset{k_6}{\overset{k_5}{\rightleftharpoons}} CH_3* + CO*$
$CH_3CO* + * \underset{k_8}{\overset{k_7}{\rightleftharpoons}} CH_2CO* + H*$	$CH_3CO* + Pt* \underset{k_8}{\overset{k_7}{\rightleftharpoons}} CH_2CO* + H*$
$CH_2CO* + * \underset{k_{10}}{\overset{k_9}{\rightleftharpoons}} CH_2* + CO*$	$CH_2CO* + Pt* \underset{k_{10}}{\overset{k_9}{\rightleftharpoons}} CH_2* + CO*$
$CH_2CO* + * \underset{k_{12}}{\overset{k_{11}}{\rightleftharpoons}} CHCO* + H*$	$CH_2CO* + Pt* \underset{k_{12}}{\overset{k_{11}}{\rightleftharpoons}} CHCO* + H*$
$CHCO* + * \underset{k_{14}}{\overset{k_{13}}{\rightleftharpoons}} CH* + CO*$	$CHCO* + Pt* \underset{k_{14}}{\overset{k_{13}}{\rightleftharpoons}} CH* + CO*$
$2H* \underset{k_{16}}{\overset{k_{15}}{\rightleftharpoons}} H_2+2*$	$2H* \underset{k_{16}}{\overset{k_{15}}{\rightleftharpoons}} H_2+2Pt*$

Figure B.1. Microkinetic model for acetaldehyde dehydrogenation and C-C bond activation processes.

The activation barriers from previous sections are inserted into the microkinetic model shown in Fig. B1 to obtain values for the rate constants under T=350K, which is the usual working

temperature for most commercialized PEMFCs. The surface coverage θi for each surface species i was solved. The site balance equation on the Pt(111) surface is therefore simply:

$$\theta_{CH3CHO} + \theta_{CH3CO} + \theta_{CH2CO} + \theta_{CHCO} + \theta_{CH3} + \theta_{CH2} + \theta_{CH} + \theta_{CO} + \theta_{H} + \theta_{*} = 1 \quad (B.1)$$

The site balance equations on the Pt-Mo surface are maintained for Pt sites and Mo sites respectively, with the surface Pt/Mo composition being 2:1 in the alloy model used in this work:

$$\theta_{CH3CHO} + \theta_{CH3CO} + \theta_{CH2CO} + \theta_{CHCO} + \theta_{Mo*} = 1/3 \quad (B.2)$$

$$\theta_{CH3} + \theta_{CH2} + \theta_{CH} + \theta_{CO} + \theta_{H} + \theta_{Pt*} = 2/3 \quad (B.3)$$

Appendix C

Complete C1 species dehydrogenation and oxidation pathways that lead to the formation of CO_2 on Pt-Mo surfaces, with Mo presenting only in the surface layer and in both the surface and subsurface layers.

C1 dehydrogenation and oxidation (Mo only in surface layer)	Activation barrier E_a (eV)	Reaction Energy ΔE_{rxn} (eV)
$CH_3^* + OH^* \rightarrow CH_3OH^*$	2.19	0.45
$CH_3^* + OH^* \rightarrow CH_2^* + H_2O^*$	1.42	-0.04
$CH_2^* + OH^* \rightarrow CH_2OH^*$	1.23	0.41
$CH_2^* + OH^* \rightarrow CH^* + H_2O^*$	0.95	-0.15
$CH_2OH^* + OH^* \rightarrow CHOH^* + H_2O^*$	0.94	0.15
$CH_2OH^* \rightarrow CH_2O^* + H^*$	0.55	-0.33
$CH_2O^* + OH^* \rightarrow CHO^* + H_2O^*$	1.23	-0.12
$CH^* + OH^* \rightarrow C^* + H_2O^*$	1.59	0.92
$CH^* + OH^* \rightarrow CHOH^*$	1.20	0.71
$CHOH^* + O^* \rightarrow HCOOH^*$	0.99	0.13
$CHOH^* + OH^* \rightarrow COH^* + H_2O^*$	1.07	-0.19
$COH^* + OH^* \rightarrow CO^* + H_2O^*$	-0.11	-0.37
$CHOH^* \rightarrow CHO^* + H^*$	0.33	-0.60
$CHO^* + OH^* \rightarrow HCOOH^*$	1.32	0.46
$HCOOH^* \rightarrow COOH^* + H^*$	1.00	-0.38

$HCOOH^* \rightarrow HCOO^* + H^*$	0.35	0.30
$HCOO^* \rightarrow CO_2^* + H^*$	0.24	-0.64
$CHO^* + OH^* \rightarrow CO^* + H_2O^*$	0.95	-0.04
$CO^* + OH^* \rightarrow COOH^*$	0.71	0.58
$COOH^* + OH^* \rightarrow CO_2^* + H_2O^*$	-0.23	0.13

Table C.1. C1 species dehydrogenation and oxidation on Pt-Mo surface with Mo only in surface layer.

C1 dehydrogenation and oxidation (Mo in surface and subsurface layers)	Activation barrier E_a (eV)	Reaction Energy ΔE_{rxn} (eV)
$CH_3^* + OH^* \rightarrow CH_3OH^*$	1.95	0.29
$CH_3^* + OH^* \rightarrow CH_2^* + H_2O^*$	1.22	0.04
$CH_2^* + OH^* \rightarrow CH_2OH^*$	1.24	0.38
$CH_2^* + OH^* \rightarrow CH^* + H_2O^*$	0.79	-0.24
$CH_2OH^* + OH^* \rightarrow CHOH^* + H_2O^*$	0.99	-0.01
$CH_2OH^* \rightarrow CH_2O^* + H^*$	0.45	-0.41
$CH_2O^* + OH^* \rightarrow CHO^* + H_2O^*$	0.65	-0.17
$CH^* + OH^* \rightarrow C^* + H_2O^*$	1.82	0.88
$CH^* + OH^* \rightarrow CHOH^*$	1.27	0.75
$CHOH^* + O^* \rightarrow HCOOH^*$	1.07	0.56
$CHOH^* + OH^* \rightarrow COH^* + H_2O^*$	1.25	-0.11
$COH^* + OH^* \rightarrow CO^* + H_2O^*$	-0.12	-0.19

CHOH* → CHO* + H*	0.63	-0.57
CHO* + OH* → HCOOH*	1.44	0.46
HCOOH* → COOH* + H*	0.89	-0.36
HCOOH* → HCOO* + H*	0.32	-0.29
HCOO* → CO_2* +H*	0.85	-0.05
CHO* + OH* → CO* + H_2O*	1.06	0.13
CO* + OH* → COOH*	0.66	0.52
COOH* + OH* → CO_2* + H_2O*	-0.21	0.16

Table C.2. C1 species dehydrogenation and oxidation on Pt-Mo surface with Mo in both surface and subsurface layers.